

AD-A086 667

POLYTECHNIC INST OF NEW YORK BROOKLYN

F/G 13/13

WAVE PROPAGATION IN HONEYCOMB AND FOAM-CORE PANELS FOR APPLICAT--ETC(1)

APR 80 H L BERTONI, S K PARK

F1962A-77-C-0130

UNCLASSIFIED

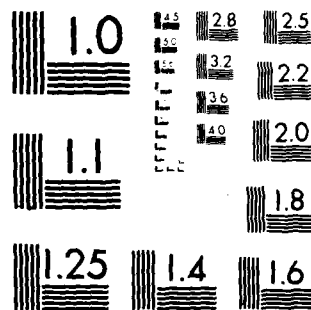
RADC-TR-80-112

NL

102

AD-A086 667





MICROCOPY RESOLUTION TEST CHART  
NATIONAL BUREAU OF STANDARDS-1963-A

54  
**LEVEL II**



**RADC-TR-80-112**  
Final Technical Report  
April 1980



# **WAVE PROPAGATION IN HONEYCOMB AND FOAM-CORE PANELS FOR APPLICATION TO PANEL NDE**

**Polytechnic Institute of New York**

Henry L. Berton  
S. K. Park

ADA 086667

APPROVED FOR PUBLIC RELEASE; DISTRIBUTION UNLIMITED

**DTIC  
ELECTE  
JUL 10 1980**

**RESEARCH AIR DEVELOPMENT CENTER  
OF THE AIR FORCE  
COLUMBIA UNIVERSITY, NEW YORK, N.Y. 10027**

This report has been reviewed by the RADC Public Affairs Office (PA) and is releasable to the National Technical Information Service (NTIS). At NTIS it will be releasable to the general public, including foreign nations.

RADC-TR-80-112 has been reviewed and is approved for publication.

APPROVED:

*Alan J. Budreau*

ALAN J. BUDREAU  
Project Engineer

APPROVED:

*Allan C. Schell*

ALLAN C. SCHELL

Chief, Electromagnetic Sciences Division

Accession for	
NTIS Grant	<input checked="" type="checkbox"/>
DOC TAB	<input type="checkbox"/>
Unannounced	<input type="checkbox"/>
Justification	
By	
Distribution	
Availability	
Dist	Availability
<i>A</i>	spec. 81

FOR THE COMMANDER:

*John P. Huse*

JOHN P. HUSE  
Acting Chief, Plans Office

If your address has changed or if you wish to be removed from the RADC mailing list, or if the address is no longer maintained by your organization, please notify RADC (RADC, Attention: AFM 80-112). This will assist us in maintaining a current mailing list.

Do not return this copy to the sender.

UNCLASSIFIED

SECURITY CLASSIFICATION OF THIS PAGE (When Data Entered)

REPORT DOCUMENTATION PAGE		READ INSTRUCTIONS BEFORE COMPLETING FORM	
1. REPORT NUMBER RADC-TR-80-112	2. GOVT ACCESSION NO. AD-A086667	3. RECIPIENT'S CATALOG NUMBER (9)	
4. TITLE (and Subtitle) WAVE PROPAGATION IN HONEYCOMB AND FOAM-CORE PANELS FOR APPLICATION TO PANEL NDE.		5. TYPE OF REPORT OR COVERED Final Technical Report 1 Jul 77 - 11 Oct 79	
6. PERFORMING ORG. REPORT NUMBER N/A		7. CONTRACT OR GRANT NUMBER(s) F19628-77-C-0130/mw	
8. AUTHOR(s) Henry L. Bertoni S. K. Park		9. PERFORMING ORGANIZATION NAME AND ADDRESS Polytechnic Inst. of New York 333 Jay Street Brooklyn NY 11201	
10. PROGRAM ELEMENT, PROJECT, TASK AREA & WORK UNIT NUMBERS 61102F 23051523		11. REPORT DATE Apr 80	
12. CONTROLLING OFFICE NAME AND ADDRESS Deputy for Electronic Technology (RADC/EEA) Hanscom AFB MA 01731		13. NUMBER OF PAGES 145	
14. MONITORING AGENCY NAME & ADDRESS (if different from Controlling Office) Same		15. SECURITY CLASS. (of this report) UNCLASSIFIED	
16. DISTRIBUTION STATEMENT (of this Report) Approved for public release; distribution unlimited.		17. DISTRIBUTION STATEMENT (of the abstract entered in Block 20, if different from Report) Same	
18. SUPPLEMENTARY NOTES RADC Project Engineer: Alan J. Budreau (RADC/EEA)			
19. KEY WORDS (Continue on reverse side if necessary and identify by block number) Non-destructive evaluation (NDE) Honeycomb panel Bloch waves			
20. ABSTRACT (Continue on reverse side if necessary and identify by block number) For rapid inspection, it is most useful to consider acoustic waves traveling along the larger dimensions of the panels. A study was made of the waves propagating in the honeycomb itself, particularly in the frequency range where the wavelength is on the order of the cell diameter. The characteristics of Bloch waves propagating in a honeycomb of infinite extent were calculated. At low frequencies, the honeycomb was found to act as an elastic continuum. At high frequencies, the periodicity and			

DD FORM 1473 EDITION OF 1 NOV 65 IS OBSOLETE

UNCLASSIFIED (Cont'd)

SECURITY CLASSIFICATION OF THIS PAGE (When Data Entered)

408704

UNCLASSIFIED

SECURITY CLASSIFICATION OF THIS PAGE(When Data Entered)

Item 20 (cont'd)

anisotropy of the honeycomb affect the propagation of the Bloch waves, and result in the presence of stop bands for propagation in certain directions. Computations of the frequency dependence, direction dependence, and polarization of the Bloch waves were made. In addition, the propagation characteristics of the waves guided by an aluminum face plate bonded to a honeycomb of semi-finite extent were studied in the low frequency range where the honeycomb acts as an elastic absorber. It was found that the presence of the honeycomb strongly perturbs the waves guided by the face plate, so that one can expect to inspect for de-bonded regions by measuring propagation characteristics. Similar results were found for a foam core bonded to an aluminum face plate. In this case, a glue layer bonding face plate to the foam was also considered and found to have a significant effect on the guided waves.

It is to be noted that the model considered under this contract is of a geometrical honeycomb in which all 6 sides are doubled in the fabrication, thereby reducing the symmetry of the structure. Therefore, further work is needed to extend the theory to the actual panels. Also, additional theoretical work to extend the upper frequency range would be desirable.

UNCLASSIFIED

SECURITY CLASSIFICATION OF THIS PAGE(When Data Entered)

## TABLE OF CONTENTS

	Page
I. INTRODUCTION .....	1
A. Honeycomb Panels .....	3
B. Foam-Core Panels .....	8
II. MODE COUPLING AT A Y JOINT .....	9
A. Transmission Line Representation .....	9
1. SH Mode .....	12
2. L Mode .....	12
3. F(0) Mode .....	13
4. F(1) Mode .....	14
B. Representation of Coupling at Y Joints .....	14
1. Particle Velocity Conditions .....	16
2. Force and Torque Conditions .....	20
3. Scattering Matrix Representation .....	22
C. Propagation Perpendicular to the Cell Axes ( $k_z = 0$ ) .....	24
III. BLOCH WAVES POLARIZED ALONG THE CELL AXES FOR PROPAGATION PERPENDICULAR TO THE CELL AXES .....	28
A. Formal Solution for Dispersion Characteristics ..	28
B. Numerical Evaluation of Propagation Characteristics .....	32
IV. BLOCH WAVES POLARIZED PERPENDICULAR TO THE CELL AXES FOR PROPAGATION PERPENDICULAR TO THE CELL AXES .....	40
A. Formal Solution for the Propagation Characteristics .....	40
1. Scattering Matrix for a Unit Cell .....	41
2. Application of Floquet Condition .....	47

# TABLE OF CONTENTS (Con't.)

	Page
B. Numerical Evaluation of the Propagation Characteristics .....	49
1. Fast-Wave Solution .....	49
2. Slow-Wave Solution .....	56
V. BLOCH WAVE PROPAGATION OBLIQUE TO THE CELL AXES .....	69
A. Low Frequency Propagation; Continuum Model .....	70
B. Dispersive Effects for the Slow Bloch Wave .....	76
C. Dispersive Effects for the Fast Bloch Wave .....	79
VI. WAVES GUIDED BY A FACE PLATE BONDED TO A HONEYCOMB .....	88
A. SH Mode of the Aluminum Plate .....	90
B. Lamb Modes of the Aluminum Plate .....	92
1. Formal Solution for the Guided Waves .....	94
2. Numerical Evaluation of the Dispersion Characteristics .....	97
VII. FOAM CORE PANELS .....	102
A. Aluminum - Foam Configuration .....	103
B. Aluminum - Glue - Foam Configuration .....	107
1. SH Modes .....	107
2. Lamb Modes .....	111
APPENDIX: Thin Plate Approximation of the Plate Modes ...	115
A. Lamb Modes of an Infinite Plate .....	117
1. Lowest Symmetric Mode: $L(0)$ .....	117
2. Antisymmetric Modes: $F(0)$ and $F(1)$ .....	121
B. SH Modes of an Infinite Plate .....	125
REFERENCES .....	128



# LIST OF ILLUSTRATIONS

Figure		Page
1.	Honeycomb core attached to one face plate .....	2
2.	Cross-section of regular hexagonal honeycomb core. Unit cell is indicated by dashed ellipse .....	6
3.	Y joint of three plates indicating the coordinate system for each plate .....	10
4.	Cross-section of the triangular cylinder at a Y joint, which is assumed to move as a rigid body .....	17
5.	Equivalent network describing the coupling of SH modes at a Y joint .....	25
6.	Equivalent circuit representing the SH modes in a unit cell of the honeycomb .....	29
7.	Reciprocal lattice points and slowness curves for normalized frequency $\theta = k_g w/2$ ; a) much less than 0.6155; b) just below 0.6155; and c) between 0.6155 and $\pi/4 = 0.7854$ .....	33
8.	Slowness curves in the first quadrant of the first Brillouin zone of the SH Bloch wave for several values of $\theta = k_g w/2$ .....	35
9.	Dispersive curve for propagation along x of the SH Bloch wave. In the range $0.6155 < k_g w/2 < 0.9553$ , $k_x$ is complex with real part given by $\text{Re } k_x w/2 = \pi/3$ .....	37
10.	Dispersion curve for propagation along y of the SH Bloch wave .....	38
11.	Magnitudes of particle velocity and stress along the left-half of a unit cell for an SH Bloch wave propagating along x at normalized frequency $k_g w/2 = 0.615$ . The curves for the right-half of the unit cell are obtained by reflecting those showing about the point $w/2$ .....	39
12.	Two halves of a unit cell showing the numbering employed in the scattering matrix representation .....	42
13.	Slowness curves in the first quadrant of the first Brillouin zone for the fast Bloch wave for various values of normalized frequency $k_g w/2$ within the first pass-band ( $w/t = 20$ , $\nu = 0.32$ ) .....	50
14.	Dispersion curve for propagation along x of the fast Bloch wave ( $w/t = 20$ , $\nu = 0.32$ ) .....	52

# LIST OF ILLUSTRATIONS (Cont'd.)

Figure		Page
15.	Dispersion curve for propagation along y of the fast Bloch wave ( $w/t = 20$ , $\nu = 0.32$ ) .....	53
16.	Dispersion curves for the various plate modes in the cell walls and for the longitudinal wave in the bulk honeycomb material ( $w/t = 20$ , $\nu = 0.32$ ) .....	55
17.	Displacement of the plates of a unit cell at an instant of time during the propagation of a fast Bloch wave in the x direction ( $w/t = 20$ , $\nu = 0.32$ ) .....	57
18.	Displacement of the plates of a unit cell at an instant of time during the propagation of a fast Bloch wave in the y direction ( $w/t = 20$ , $\nu = 0.32$ ) .....	58
19.	Slowness curves in the first quadrant of the first Brillouin zone for the slow Bloch wave for various values of normalized frequency $k_s w/2$ within the first pass-band ( $w/t = 20$ , $\nu = 0.32$ ) .....	59
20.	Dispersion curve for propagation along x of the slow Bloch wave ( $w/t = 20$ , $\nu = 0.32$ ) .....	60
21.	Dispersion curve for propagation along y of the slow Bloch wave ( $w/t = 20$ , $\nu = 0.32$ ) .....	61
22.	Displacement of the plates of a unit cell at an instant of time during the propagation of a slow Bloch wave in the x direction ( $w/t = 20$ , $\nu = 0.32$ ) .....	63
23.	Displacement of the plates of a unit cell at an instant of time during the propagation of a slow Bloch wave in the y direction ( $w/t = 20$ , $\nu = 0.32$ ) .....	64
24.	Slowness curves in the first quadrant of the first Brillouin zone for the slow Bloch wave for normalized frequencies in the range $0.112 < k_s w/2 < 0.185$ ( $w/t = 20$ , $\nu = 0.32$ ) .....	66
25.	Slowness curves in the first quadrant of the first Brillouin zone for the slow Bloch wave for normalized frequencies in the range $0.185 < k_s w/2 < 0.341$ ( $w/t = 20$ , $\nu = 0.32$ ) .....	68
26.	Slowness curves in the $(k_x, k_z)$ and $(k_y, k_z)$ planes for the Q-P and Q-SV Bloch waves at low frequency ( $k_s w/2 = 0.01$ ) for a honeycomb with $w/t = 20$ , $\nu = 0.32$ .....	71
27.	Slowness curves in the $(k_x, k_z)$ and $(k_y, k_z)$ planes for all three Bloch waves at low frequency ( $k_s w/2 = 0.01$ ) for a honeycomb with $w/t = 20$ , $\nu = 0.32$ . Note the difference in vertical and horizontal scales need to accommodate the Q-SH Bloch wave .....	73

# LIST OF ILLUSTRATIONS (Cont'd.)

Figure		Page
28.	Slowness curves in the $(k_x, k_z)$ and $(k_y, k_z)$ planes for frequency $k_s w/2 = 0.03$ approaching the first stop-band for propagation along x of the Q-SH Bloch wave ( $w/t = 20$ , $\nu = 0.032$ ) .....	77
29.	Slowness curves in the $(k_x, k_z)$ and $(k_y, k_z)$ planes for frequency $k_s w/2 = 0.06$ located in the first stop-band for propagation along x of the Q-SH Bloch wave ( $w/t = 20$ , $\nu = 0.32$ ) .....	78
30.	Slowness curves in the $(k_x, k_z)$ plane for frequency $k_s w/2 = 0.13$ in the second pass-band of the Q-SH Bloch wave showing the presence of a fourth surface ( $w/t = 20$ , $\nu = 0.32$ ) .....	80
31.	Slowness curves in the $(k_y, k_z)$ plane for frequency $k_s w/2 = 0.13$ in the second pass-band of the Q-SH Bloch wave showing the presence of a fourth surface ( $w/t = 20$ , $\nu = 0.32$ ). This figure is for the same frequency as Fig. 30 .....	81
32.	Slowness curves in the $(k_x, k_z)$ plane for frequency $k_s w/2 = 0.26$ in the third pass-band of the Q-SH Bloch wave ( $w/t = 20$ , $\nu = 0.32$ ) .....	82
33.	Slowness curves in the $(k_y, k_z)$ plane for frequency $k_s w/2 = 0.26$ in the third pass-band of the Q-SH Bloch wave ( $w/t = 20$ , $\nu = 0.32$ ). This figure is for the same frequency as Fig. 32 .....	83
34.	Slowness curves in the $(k_x, k_z)$ and $(k_y, k_z)$ plane of the Q-P and Q-SV Bloch waves for frequency $k_s w/2 = 0.21$ just below the point where the two waves have the same phase velocity in the $(x, y)$ plane .....	85
35.	Slowness curves in the $(k_x, k_z)$ and $(k_y, k_z)$ plane of the Q-P and Q-SV Bloch waves for frequency $k_s w/2 = 0.23$ just above the point where the two waves have the same phase velocity in the $(x, y)$ plane. Note the change in polarization indicated as the direction of propagation changes from being along z to being perpendicular to z..	86
36.	Coordinate system used in computing the characteristics of waves guided by an aluminum face plate bonded to a semi-infinite honeycomb .....	89
37.	Attenuation constant $\alpha$ and propagation constant $\beta$ of the SH leaky wave guided by an aluminum face plate bonded to a semi-infinite honeycomb .....	93

# LIST OF ILLUSTRATIONS (Cont'd.)

Figure		Page
38.	Attenuation constant $\alpha$ and propagation constant $\beta$ of the leaky Lamb wave guided by an aluminum face plate bonded to a semi-infinite honeycomb .....	99
39.	Propagation constant $\beta$ of the flexural mode guided by an aluminum face plate bonded to a semi-infinite honeycomb. For this mode $\alpha = 0$ .....	101
40.	Propagation constants $\beta$ of the L(0) and F(0) leaky wave modes of a 1/16 in. aluminum plate on which a polyurethane foam has been formed. These curves are numerically the same as those found for a free plate ...	105
41.	Attenuation constants $\alpha$ of the L(0), SH(0) and F(0) leaky wave modes of a 1/16 in. aluminum plate on which a polyurethane foam has been formed .....	106
42.	Propagation constants $\beta$ of the SH(0) and SH(1) modes of a 1/16 in. aluminum plate covered with 1/64 in. of glue, with and without bonding to a semi-infinite polyurethane foam .....	108
43.	Attenuation constants $\alpha$ of the SH(0) and SH(1) leaky wave modes of a 1/16 in. aluminum plate covered with 1/64 in. of glue that bonds the plate to a semi-infinite polyurethane foam .....	110
44.	Propagation constants $\beta$ of Lamb modes of a 1/16 in. aluminum plate covered with 1/64 in. of glue, with and without bonding to a semi-infinite polyurethane foam .....	112
45.	Attenuation constants $\alpha$ of Lamb modes of a 1/16 in. aluminum plate covered with 1/64 in. of glue, with and without bonding to a semi-infinite polyurethane foam ...	114
A-1.	Geometry of an infinite plate and the transmission line representation for a given plate mode, taking the transmission direction to be along x .....	116

## EVALUATION

1. This is the Final Report on the contract. It covers the period 1 July 77 to 11 Oct 79. The objective of this research was to study the waves which can propagate on a honeycomb panel of the type used to construct the shelters which house much of the ground-based electronic equipment developed by the Electronic Systems Division. By knowing the waves that can propagate on such panels, it will be possible to develop a system of non-destructive evaluation (NDE) which can, in a cost-effective way, find defective panels and avoid their incorporation into shelters.

2. Although this work terminated before developing a complete theory appropriate to the exact honeycomb structures used in shelter panels, it does provide adequate information for understanding the waves appropriate for the NDE of shelter panels and would form the basis of an experimental study.

*Alan J. Budreau*

ALAN J. BUDREAU  
Project Engineer

## I. INTRODUCTION

Honeycomb panels and foam-core panels consist of a light-weight core bonded between face plates. This fabrication results in a strong light-weight and insulating construction element. Such panels are used in containers for housing electronic equipment. Honeycomb panels are also used in airplane construction, while foam-core panels are used for insulating tanks.

In the case of the honeycomb panel, the core consists of an array of thin-walled, hollow cylinders of hexagonal cross-section, as shown in Figure 1, and resembles a honeycomb. The core material consists of waxed cardboard in the case of equipment containers, while in airplane construction it is usually metal. Face plates are attached to both ends of the core using epoxy or other adhesive bonding materials (one of the face plates is shown in Figure 1).

Foam-core panels consist of a foamed plastic, such as styrofoam, between face plates. The foam can be generated by interacting the chemical agents directly on the face plates, in which case a welded bond exists between the foam and plate. Alternatively a prepared foam core may be glued to the face plates.

During fabrication and use, defects can occur within the panel, and are therefore not detectable by visual inspection. One type of defect is a region of a face plate that is not bonded to the core. Another defect in honeycomb panels is the presence of water in some of the cells, which can degrade a cardboard core and weaken the epoxy or adhesive bond between core and faceplate. Other defects are buckled or fractured cell walls.

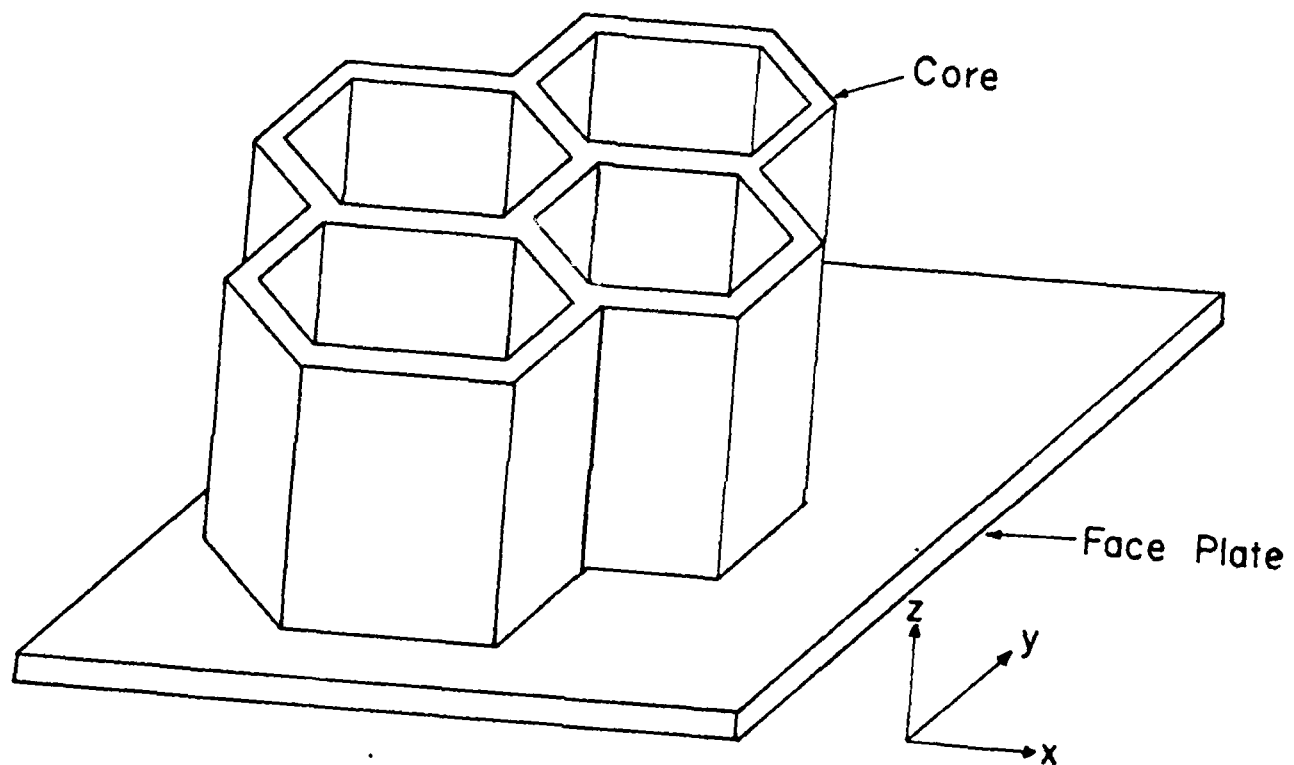


Figure 1. Honeycomb core attached to one face plate.

Currently, acoustic non-destructive evaluation (NDE) techniques are used to locate the defects cited above in honeycomb panels. An acoustic beam in a fluid is directed at normal incidence on the panel and received at the opposite face. The beam is then scanned in a raster fashion over the area of the panel. Unbonded regions interrupt the transmission while water in cells increases the transmission. Since the size of the acoustic beam is on the order of the cell diameter, the raster scan inspection procedure is very lengthy for a large panel. A great reduction in inspection time could be achieved by propagating the acoustic waves parallel to the face plates, rather than perpendicular to them. In this way, one would inspect an entire strip along the panel at one time. Reinspecting installed panels with only one face exposed would require using waves that propagate along the panel.

#### A. Honeycomb Panels

Low frequency studies of propagation along honeycomb panels<sup>(1)</sup> have been carried out with the aim of NDE inspection in mind. However, it was recognized that successful NDE inspection would require the use of high frequencies for which the acoustic wavelengths would be on the order of the cell diameter. Establishment of a sensitive test procedure requires a knowledge of the propagation characteristics of the modes guided by honeycomb panels. From such knowledge, one can determine the frequency and mode polarization most useful for inspection. These choices must be made in relation to the geometric design and elastic properties of materials used in the panel.

In this report we first compute the properties of waves propagating through a honeycomb of infinite extent. Because the honeycomb is a



periodic structure in two dimensions (and uniform in the third dimension), the waves propagating through it are Bloch waves, which are analogous to plane waves in an elastic continuum. Each elastic field quantity in a Bloch wave is the product of a plane wave's exponential factor, and a second function that gives the variation of the field quantity within a unit cell. In the case of a honeycomb, this second function is defined only within the honeycomb walls if the space within the cells is assumed empty. The waves guided by an assembled panel will be a combination of the Bloch waves, just as the waves guided by a plate are a combination of the plane waves of an infinite medium.

The calculation of Bloch wave propagation characteristics are carried out over the range from low to high frequencies. At low frequencies (below 1.0 kHz for a Shelter Core honeycomb) the core is found to act as an elastic continuum of hexagonal symmetry, and hence supporting three wave types. At high enough frequencies (above 10 kHz for the Shelter Core honeycomb), the wavelength of all wave types is on the order of the cell diameter, and hence the periodicity of the honeycomb strongly effects the propagation.

Having computed the Bloch waves in an infinite honeycomb, we next compute the characteristics of the waves guided by a structure consisting of one face plate bonded to a semi-infinite honeycomb. In this case, the waves guided by the face plate are strongly perturbed by the coupling to the core. The SH and symmetric Lamb waves in the face plate are found to radiate or leak energy in to the honeycomb, and hence are of the leaky wave type. The flexural wave in the face plate is speeded up by the honeycomb, but remains a bound surface wave. These calculations are carried out treating the core as an elastic continuum. For a Shelter

Core honeycomb this means frequencies below 1.0 kHz for the SH wave in the face plate, and below 10 kHz for the symmetric Lamb and flexural modes of the face plate.

The cross-section of a regular hexagonal honeycomb is shown in Figure 2. The core consists of strips or plates of thickness  $t$ , width  $w$  and infinite length along  $z$  (out of plane of the paper). The strips are assumed to be arranged in a regular hexagonal pattern. This assumption idealizes actual honeycombs, whose fabrication leads to hexagons having unequal vertex angles, and two of whose side walls are of double thickness as compared to the other four.

A unit cell of the periodic core is indicated by the dashed curve in Figure 2. The entire periodic core can be generated by translations of the unit cell along the basis vectors  $\underline{d}_1$  and  $\underline{d}_2$ , as shown in Figure 2, of the periodic structure. The cell is seen to be composed of plate segments coupled at two Y joints. A primary part of the study of core waves therefore involves the coupling of the plate waves at the Y joint.

The acoustic fields in the plate segments that form the cell walls can be expressed as a superposition of plate modes. Since the thickness  $t$  of the cell walls is one tenth of their width  $w$ , or less, thin plate approximations may be made for the plate modes, even for frequencies where the cell diameter is on the order of the acoustic wavelength. Consistent with this approximation we keep only the lowest four plate modes, which are: 1) the shear wave with no variation across the plate - the SH mode; 2) the lowest symmetric Lamb mode - L mode; 3) the lowest anti-symmetric Lamb mode or flexural wave - F(0) mode; and 4) the first cutoff flexural wave - F(1) mode.

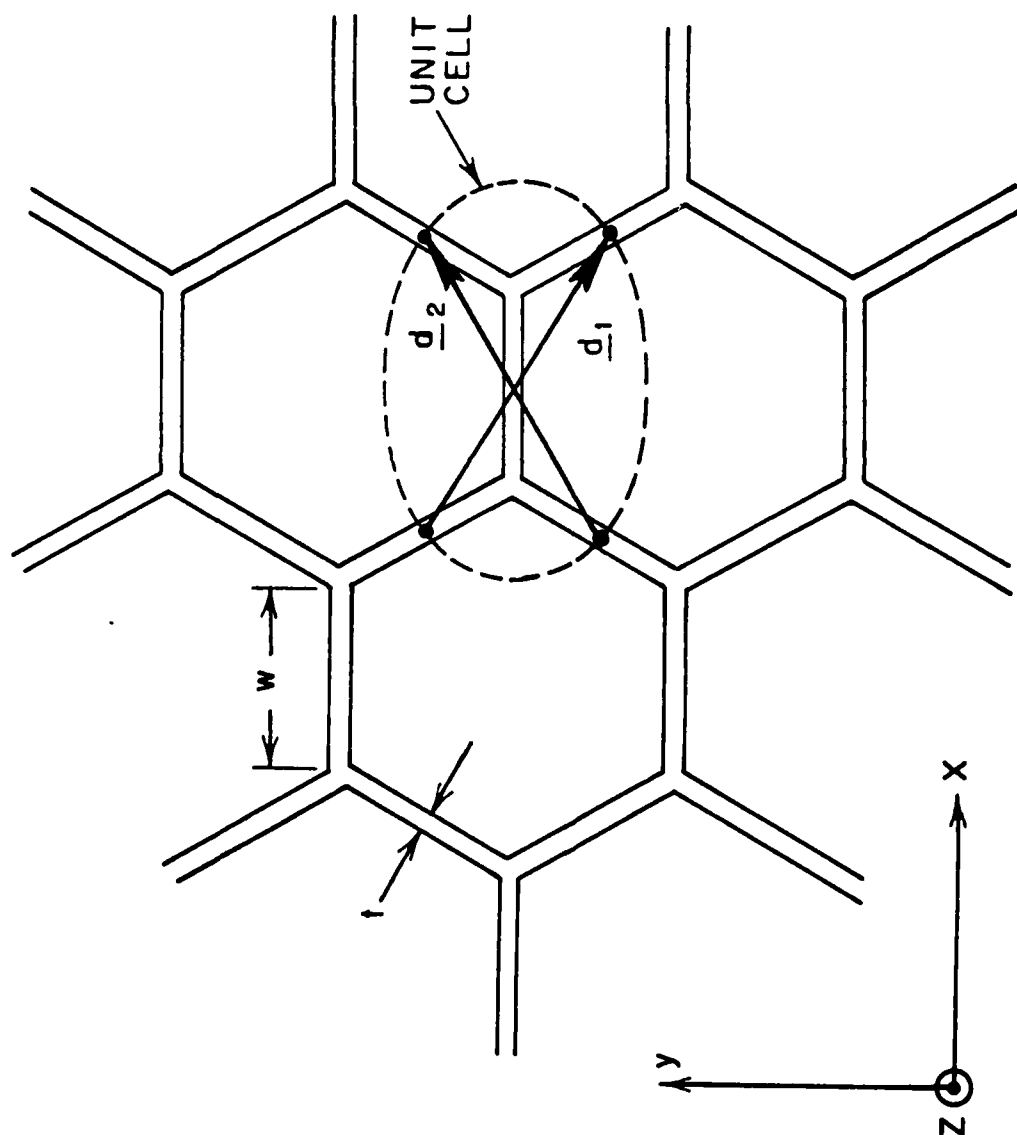


Figure 2. Cross-section of regular hexagonal honeycomb core.  
Unit cell is indicated by dashed ellipse.

The  $F(1)$  mode is included since it has the same transverse variation through the thickness of the plate as the  $F(0)$  mode, and since its attenuation constant vanishes as frequency goes to zero. Hence, this mode will couple neighboring Y joints at low frequency and its inclusion is necessary to accurately find the amplitude of the  $F(0)$  mode excited even at an isolated Y joint. All higher order plate modes attenuate rapidly away from the Y joint, even in the limit of zero frequency, and therefore do not couple neighboring Y joints. In addition these modes have more variation through the thickness of the plate, and are therefore not expected to be strongly excited.

The physical approximations used to obtain the mode coupling are discussed in Section II. These approximations are embodied in a set of twelve equations containing the amplitudes of the twelve modes (four modes in each of the three plates). From these equations a scattering matrix is obtained that gives the amplitudes of each of the twelve modes excited at the Y joint for any incident mode.

For propagation perpendicular to the cell axes the SH mode does not couple to the L,  $F(0)$  and  $F(1)$  modes at the Y joint, as discussed in Section II. Thus we may treat separately the case of waves having particle motion parallel to the cell axis, which corresponds to the SH plate mode polarization, and whose properties are found in Section III. The L,  $F(0)$  and  $F(1)$  modes together give rise to two Bloch waves in the honeycomb polarized with particle motion perpendicular to the cell axis, which are considered in Section IV.

The case of propagation oblique to the cell axes is treated in Section V. Here, the shape of the intersection of the slowness surfaces with the principle planes is found. From these curves and the propagation

perpendicular to the cell axes it is possible to infer the shape of the complete slowness surface. At high frequencies it is found that more than three surfaces can exist, and these surfaces indicate that propagation can take place only over a limited range of angles about the direction of the cell axes.

The characteristics of Bloch wave propagation at low frequencies are used to define the constants of an elastic continuum of hexagonal symmetry. This continuum is assumed to be directly bonded to an aluminum face plate and the propagation constant of waves guided by the combination are determined in Section VI.

#### B. Foam-Core Panels

In studying foam-core panels, we have treated the case of waves guided by a single aluminum face plate attached to a semi-infinite foam core, as discussed in Section VII. The foam is treated as an isotropic continuum, with elastic constants representative of typical static values found in the literature. Both the case of directly bonded and glued foams are considered. The waves are found to radiate or leak energy into the foam. The rate of leakage and the propagation constant are found to be strongly influenced by the presence of a glue layer.

## II. MODE COUPLING AT A Y JOINT

The Y joint of three plates is shown in Figure 3. For each plate, with index  $i = 1, 2, 3$  a coordinate system  $(x_i, y_i, z)$  is established as shown. In treating Bloch wave propagation oblique to the cell axes, all four of the plate modes in the cell walls will couple at the Y joint. In order to satisfy the coupling equations for all values of  $z$  along the joint, all of the modes must have the same phase dependence  $\exp(-jk_z z)$ , where  $k_z$  is the wavenumber along  $z$ . This condition is the analogue of Snell's law in optics. Since the Bloch wave is formed by the plate modes that are multiply scattered at the Y joint, all fields in the Bloch wave must have the same phase variation along  $z$ , and hence  $k_z$  is the  $z$  component of the wavevector of the Bloch wave. The variation of the modal fields along  $(x_i, y_i, z)$  in each plate can be represented by equivalent transmission lines<sup>(2-6)</sup>. Mode coupling at a Y joint is then represented by an interconnection of the modal transmission lines, or by a scattering matrix.

### A. Transmission Line Representation

In the transmission line representation, the fields of each mode for harmonic time dependence  $\exp(j\omega t)$  are expressed in the form

$$\begin{bmatrix} v_y(x_i, y_i, z) \\ v_z(x_i, y_i, z) \\ T_{xx}(x_i, y_i, z) \end{bmatrix} = V(x_i) \begin{bmatrix} g_1(y_i) \\ g_2(y_i) \\ g_3(y_i) \end{bmatrix} e^{-jk_z z} \quad (1-a)$$

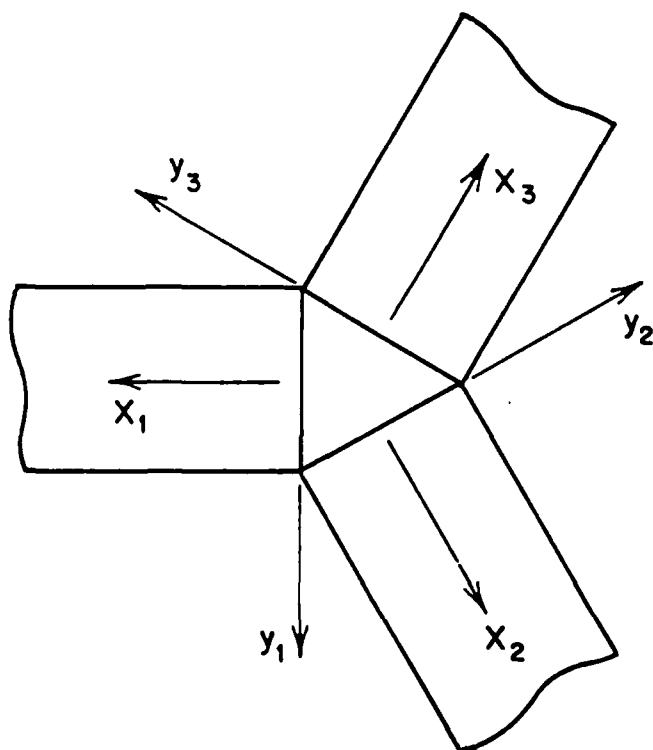


Figure 3. Y joint of three plates indicating the coordinate system for each plate.

$$\begin{bmatrix} T_{xy}(x_i, y_i, z) \\ T_{xz}(x_i, y_i, z) \\ v_x(x_i, y_i, z) \end{bmatrix} = I(x_i) \begin{bmatrix} q_1(y_i) \\ q_2(y_i) \\ q_3(y_i) \end{bmatrix} e^{-jk_z z} \quad (1-b)$$

In (1), the  $1 \times 3$  matrices  $\underline{g}(y_i)$  and  $\underline{q}(y_i)$  are the mode vectors and  $V(x_i)$ ,  $I(x_i)$  are the modal voltages and currents. In terms of traveling waves,  $\mu\kappa$

$$\left. \begin{aligned} V(x_i) &= (be^{-j\kappa x_i} + ae^{j\kappa x_i}) \sqrt{Z} \\ I(x_i) &= (be^{-j\kappa x_i} - ae^{j\kappa x_i}) \frac{1}{\sqrt{Z}} \end{aligned} \right\} \quad (2)$$

where  $\kappa$  is the wavenumber of the mode,  $Z$  is the modal impedance, and  $b$ ,  $a$  are the amplitudes of the waves traveling in the  $+$  and  $-x_i$  directions, respectively. If the mode vectors are normalized such that

$$\int_{-t/2}^{t/2} \underline{g}(y_i) \cdot \underline{q}^*(y_i) dy = -1, \quad (3)$$

then  $\text{Re}[V(x_i)I^*(x_i)]$  represents the power carried in the  $+x_i$  direction by the mode, per unit length along  $z$ . For propagating modes  $\kappa$  and  $Z$  are real and

$$\text{Re}[V(x_i)I^*(x_i)] = |b|^2 - |a|^2, \quad (4)$$

while for evanescent modes with  $\kappa$  imaginary,  $Z$  is imaginary and

$$\text{Re}[V(x_i)I^*(x_i)] = \text{Re}\left[\frac{Z}{|Z|} (ab^* - a^*b)\right]. \quad (5)$$

The various modal quantities for plate waves have previously been derived (5, 6).



For thin plates, the plane-strain approximations may be made for the modal fields<sup>(7, 8)</sup>. In this approximation, the cross-section of the plate is assumed to remain a plane surface of constant width. Employing this approximation, we derive in the Appendix the various quantities for each mode. The modal quantities are tabulated below. In these expressions,  $\mu$  is the shear modulus of the wall material,  $\rho$  is its density and  $\nu$  is Poisson's ratio. The wave number  $k_s$  of shear waves in the wall material is

$$k_s = \omega \sqrt{\frac{\rho}{\mu}}. \quad (6)$$

1. SH Mode

$$\kappa_s = \sqrt{k_s^2 - k_z^2}; \quad Z_s = \frac{\mu \kappa_s}{\omega} \quad (7)$$

$$\underline{g}(y) = \frac{1}{\sqrt{t}} \begin{bmatrix} 0 \\ \frac{1}{\sqrt{\mu \rho}} \\ \frac{2k_z}{k_s} \end{bmatrix}; \quad \underline{q}(y) = \frac{1}{\sqrt{t}} \begin{bmatrix} 0 \\ \sqrt{\mu \rho} \frac{k_z^2 - \kappa_s^2}{k_s^2} \\ -\frac{k_z}{k_s} \end{bmatrix} \quad (8)$$

2. L Mode

$$\left. \begin{aligned} k_L &= k_s \sqrt{(1-\nu)/2} \\ \kappa_L &= \sqrt{k_L^2 - k_z^2}; \quad Z_L = \frac{\omega \rho}{\kappa_L} \end{aligned} \right\} \quad (9)$$

$$\underline{g}(y) = \frac{1-\nu}{\sqrt{t}} \begin{bmatrix} 0 \\ \frac{1}{\sqrt{\mu\rho}} \frac{k_z k_s}{2k_L^2} \\ \frac{-1}{1-\nu} + \frac{k_z^2}{k_L^2} \end{bmatrix} ; \quad \underline{q}(y) = \begin{bmatrix} 0 \\ -\sqrt{\mu\rho} \frac{k_z}{k_s} \frac{2}{\sqrt{t}} \\ \frac{1}{\sqrt{t}} \end{bmatrix} \quad (10)$$

### 3. F(0) Mode

$$\left. \begin{aligned} k_{F0} &= \sqrt{\frac{k_s}{t} \sqrt{6(1-\nu)}} \\ \kappa_0 &= \sqrt{k_{F0}^2 - k_z^2} ; \quad Z_0 = \frac{\omega\rho}{\kappa_0} \end{aligned} \right\} \quad (11)$$

$$\underline{g}(y) = \frac{1}{N_0} \begin{bmatrix} \frac{1}{\sqrt{\mu\rho}} & \frac{1}{1-2r} \\ \frac{jk_z y}{\sqrt{\mu\rho}} & \frac{1}{1-2r} \\ jk_s y \left\{ \frac{1}{1-\nu} + \frac{1}{1-2r} \left( \frac{2k_z^2}{k_s^2} - 1 \right) \right\} \end{bmatrix} ; \quad \underline{q}(y) = \frac{1}{N_0} \begin{bmatrix} \sqrt{\mu\rho} \frac{k_s^2((t/2)^2 - y^2)}{2(1-\nu)} \\ -j2\sqrt{\mu\rho} k_z y \frac{1}{1-2r} \\ \frac{jk_s y}{1-2r} \end{bmatrix} \quad (12)$$

Here

$$N_0^2 = \frac{k_s^2 t^3}{6(1-\nu)(2r-1)} \left[ 1 + \frac{1-\nu}{2(2r-1)} \right] \quad (13)$$

and

$$r = \sqrt{6(1-\nu)} / k_s t. \quad (14)$$

#### 4. F(1) Mode

$$\left. \begin{aligned} k_{F1} &= -jk_{F0} \\ \kappa_1 &= \sqrt{k_{F1}^2 - k_z^2} ; \quad Z_1 = -\frac{\omega \rho}{\kappa_1} \end{aligned} \right\} \quad (15)$$

$$g(y) = \frac{1}{N_1} \begin{bmatrix} \sqrt{\mu \rho} \frac{1}{1+2r} \\ \frac{jk_z y}{\sqrt{\mu \rho}} \frac{1}{1+2r} \\ jk_s y \left\{ \frac{1}{1-\nu} + \frac{1}{1+2r} \left( \frac{2k_z^2}{k_s^2} - 1 \right) \right\} \end{bmatrix} ; \quad q(y) = \frac{1}{N_1} \begin{bmatrix} -\sqrt{\mu \rho} \frac{k_s^2 ((t/2)^2 - y^2)}{2(1-\nu)} \\ j2 \sqrt{\mu \rho} \frac{k_z y}{1+2r} \\ -jk_s y \frac{1}{1+2r} \end{bmatrix} \quad (16)$$

Here

$$N_1^2 = \frac{k_s^2 t^3}{6(1-\nu)(2r+1)} \left[ 1 - \frac{1-\nu}{2(2r+1)} \right] \quad (17)$$

and  $r$  is given by (13).

#### B. Representation of Coupling at Y Joints

The Y joint of three plates, as shown in Figure 3, may be viewed as the connection to a triangular cylinder of three plates having end faces perpendicular to  $x_1$ . With this view, mode coupling at the Y joint is determined by the boundary conditions at the surfaces of the triangular cylinder. We assume that the cylinder is rigid and massless. The assumption of rigid motion composed of translation and rotation about the  $z$  axis is consistent with the plane strain approximation used for the modal fields. Neglecting the mass of the cylinder implies that the net force and torque about the  $z$  axis must vanish,

and ignores the kinetic energy that it stored in the cylinder's motion. Rotation of the cross-section about the x and y axes is not taken into account, nor are the torques about these axes considered. Experience with structures that are periodic in one dimension suggests that the effect of neglecting the kinetic and potential energy in the cylinder is limited to a small error in the frequencies predicted for the stop-bands<sup>(9)</sup>, which is not expected to be significant for NDE applications. The approximations used here are essentially the same as those used to describe mode coupling at L and butt joints of two plates<sup>(10)</sup>.

If the rotation and torque about the x and y axes were taken into account more equations would be obtained than the number of scattered waves. As a result, the scattering problem would be over determined, and it would be necessary to include more scattered modes in the plates. Physically, the particle velocities associated with the rotation of the cross-section about x and y will be small compared to the translational velocities. To estimate the differences in the velocities cited, consider the F(0) mode to be incident in plate 1 of Figure 3 at an angle  $\theta$  with respect to the  $x_1$  axis. This mode will tend to rotate the triangle about the  $x_1$  axis, in addition to rotating it about z and translating it along  $y_1$ . At the corner  $x_1 = 0$ ,  $y_1 = t/2$ , the particle velocity due to the rotation about  $x_1$  is  $v_z(t/2)$  while the translational velocity is  $v_y$ . From the mode vector given by (21) it can be shown that the ratio  $v_z(t/2)/v_y$  is of the order  $\sqrt{k_s t/2} \sin \theta$ , which is less than about  $(0.1) \sin \theta$  for the highest frequencies discussed here. In other words, the particle velocity due to rotation about  $x_1$  is small compared to the translational velocity,

and hence little error will be introduced by not accounting for the rotation.

### 1. Particle Velocity Conditions

Let  $\underline{v}_i(y_i)\exp(-jk_z z)$  be the particle velocity at the end face  $x_i = 0$  of the  $i$ th plate in Figure 3. Now the motion of the triangular cylinder consists of a translation  $\underline{v}_0\exp(-jk_z z)$  of the center of gravity plus a rotation  $\Omega \underline{z}_0\exp(-jk_z z)$ . Referring to Figure 4, it is seen that the particle velocity of the  $i$ th face, with the phase factor  $\exp(-jk_z z)$  understood, is

$$\underline{v}_i(y_i) = \underline{v}_0 + \Omega \underline{z}_0 \times \underline{r} = \underline{v}_0 - \underline{x}_{oi} \Omega y_i + y_{oi} \Omega d, \quad (18)$$

where  $\underline{x}_{oi}$  and  $y_{oi}$  are unit vectors along  $x_i$  and  $y_i$ , and

$$d = \frac{t}{2\sqrt{3}} \quad (19)$$

is the perpendicular distance from the center of gravity to the triangular faces.

Alternatively, the particle velocity  $\underline{v}_i(y_i)$  can be expressed in terms of the modes of the plate. Let  $V_{Si}$ ,  $I_{Si}$  be the voltage and current at  $x_i = 0$  of the SH mode in the  $i$ th plate. Similarly, let  $V_{Li}$ ,  $I_{Li}$  and  $V_{0i}$ ,  $I_{0i}$  and  $V_{1i}$ ,  $I_{1i}$  be the voltages and currents at  $x_i = 0$  of the L, F(0) and F(1) modes in the  $i$ th plate. The particle velocity at  $x_i = 0$  can be expressed in terms of the plate modes using the modal quantities listed in the previous section. With the phase factor  $\exp(-jk_z z)$  implied, the components of particle velocity are

$$\underline{x}_{oi} \cdot \underline{v}_i(y_i) = I_{Li} \frac{1}{\sqrt{t}} - I_{Si} \frac{k_z}{\sqrt{t} k_s} + I_{0i} \frac{-jk_s y_i}{N_0(2r-1)} + I_{1i} \frac{-jk_s y_i}{N_1(2r-1)} \quad (20)$$

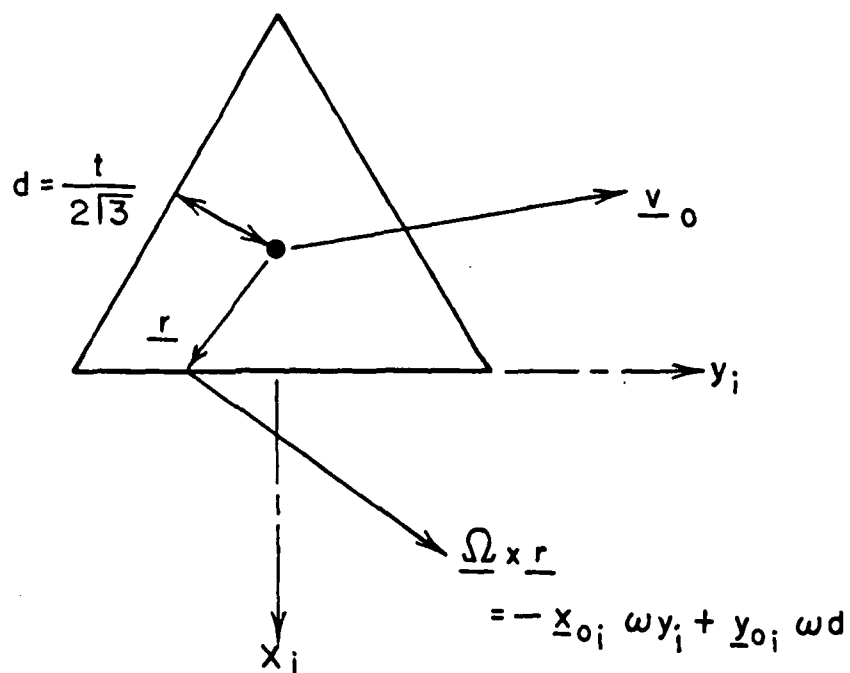


Figure 4. Cross-section of the triangular cylinder at a Y joint, which is assumed to move as a rigid body.

$$\underline{y}_{0i} \cdot \underline{v}_i(y_i) = V_{0i} \frac{-1}{N_0 \sqrt{\mu \rho} (2r-1)} + V_{1i} \frac{1}{N_1 \sqrt{\mu \rho} (2r+1)} \quad (21)$$

$$\underline{z}_o \cdot \underline{v}_i(y_i) = V_{Li} \frac{k_z k_s (1-\nu)}{2 \sqrt{t \mu \rho} k_L^2} + V_{Si} \frac{1}{\sqrt{t \mu \rho}} \quad (22)$$

In writing (22) the z components of particle velocity of the F(0) and F(1) modes were not included since they depend linearly on  $y_i$ , and hence represent a rotation about the  $x_i$  axis, which is not accounted for in our approximation.

The particle velocity (20)-(22) of each plate end must be consistent with translation of the triangular cylinder and its rotation about z, as stated in equation (18). Equating like powers of  $y_i$  for each component gives the equations

$$-\Omega = I_{0i} \frac{-jk_s}{N_0 (2r-1)} + I_{1i} \frac{-jk_s}{N_1 (2r+1)} \quad (23)$$

$$\underline{x}_{oi} \cdot \underline{v}_o = I_{Li} \frac{1}{\sqrt{t}} - I_{Si} \frac{k_z}{\sqrt{t} k_s} \quad (24)$$

$$\underline{y}_{oi} \cdot \underline{v}_o + \Omega d = V_{0i} \frac{-1}{N_0 \sqrt{\mu \rho} (2r-1)} + V_{1i} \frac{1}{N_1 \sqrt{\mu \rho} (2r+1)} \quad (25)$$

$$\underline{z}_o \cdot \underline{v}_o = V_{Li} \frac{k_z k_s (1-\nu)}{2 \sqrt{t \mu \rho} k_L^2} + V_{Si} \frac{1}{\sqrt{t \mu \rho}} \quad (26)$$

Four equations can be obtained by substituting (23) into (25) and using the relations

$$\underline{x}_{o2} \cdot \underline{v}_o = -\frac{1}{2} \underline{x}_{o1} \cdot \underline{v}_o + \frac{\sqrt{3}}{2} \underline{y}_{o1} \cdot \underline{v}_o \quad (27. a)$$

$$x_{03} \cdot v_o = -\frac{1}{2} x_{01} \cdot v_o - \frac{\sqrt{3}}{2} y_{01} \cdot v_o \quad (27. b)$$

$$y_{02} \cdot v_o = -\frac{\sqrt{3}}{2} x_{01} \cdot v_o - \frac{1}{2} y_{01} \cdot v_o \quad (27. c)$$

$$y_{03} \cdot v_o = \frac{\sqrt{3}}{2} x_{01} \cdot v_o - \frac{1}{2} y_{01} \cdot v_o \quad (27. d)$$

Also, (25) represents two equations relating the modal quantities, as does (26). The eight equations so obtained are

$$\begin{aligned} 0 = & \frac{2}{\sqrt{3t}} (I_{L2} + \frac{1}{2} I_{L1}) - \frac{2}{\sqrt{3t}} \frac{k_z}{k_s} (I_{S2} + \frac{1}{2} I_{S1}) \\ & + \frac{1}{\sqrt{\mu\rho}} \left[ \frac{V_{01}}{N_0(2r-1)} - \frac{V_{11}}{N_1(2r+1)} \right] + jk_s d \left[ \frac{I_{01}}{N_0(2r-1)} + \frac{I_{11}}{N_1(2r+1)} \right] \end{aligned} \quad (28. a)$$

$$\begin{aligned} 0 = & \frac{2}{\sqrt{3t}} (I_{L3} + \frac{1}{2} I_{L1}) - \frac{2}{\sqrt{3t}} \frac{k_z}{k_s} (I_{S3} + \frac{1}{2} I_{S1}) \\ & - \frac{1}{\sqrt{\mu\rho}} \left[ \frac{V_{01}}{N_0(2r-1)} - \frac{V_{11}}{N_1(2r+1)} \right] - jk_s d \left[ \frac{I_{01}}{N_0(2r-1)} + \frac{I_{11}}{N_1(2r+1)} \right] \end{aligned} \quad (28. b)$$

$$\begin{aligned} 0 = & -\frac{\sqrt{3}}{2\sqrt{t}} \left[ I_{L1} - \frac{k_z}{k_s} I_{S1} \right] + \frac{1}{\sqrt{\mu\rho}} \left[ \frac{V_{02} + \frac{1}{2} V_{01}}{N_0(2r-1)} - \frac{V_{12} + \frac{1}{2} V_{11}}{N_1(2r+1)} \right] \\ & + jk_s d \left[ \frac{I_{02} + \frac{1}{2} I_{01}}{N_0(2r-1)} + \frac{I_{12} + \frac{1}{2} I_{11}}{N_1(2r+1)} \right] \end{aligned} \quad (28. c)$$

$$\begin{aligned} 0 = & \frac{\sqrt{3}}{2\sqrt{t}} \left[ I_{L1} - \frac{k_z}{k_s} I_{S1} \right] + \frac{1}{\sqrt{\mu\rho}} \left[ \frac{V_{03} + \frac{1}{2} V_{01}}{N_0(2r-1)} - \frac{V_{13} + \frac{1}{2} V_{11}}{N_1(2r+1)} \right] \\ & + jk_s d \left[ \frac{I_{03} + \frac{1}{2} I_{01}}{N_0(2r-1)} + \frac{I_{13} + \frac{1}{2} I_{11}}{N_1(2r+1)} \right] \end{aligned} \quad (28. d)$$



$$\begin{aligned}
\frac{I_{01}}{N_0(2r-1)} + \frac{I_{11}}{N_1(2r+1)} &= \frac{I_{02}}{N_0(2r-1)} + \frac{I_{12}}{N_1(2r+1)} \\
&= \frac{I_{03}}{N_0(2r-1)} + \frac{I_{13}}{N_1(2r+1)}
\end{aligned} \tag{29}$$

$$\begin{aligned}
(1-\nu) \frac{k_z k_s}{2k_L^2} V_{L1} + V_{S1} &= (1-\nu) \frac{k_z k_s}{2k_L^2} V_{L2} + V_{S2} \\
&= (1-\nu) \frac{k_z k_s}{2k_L^2} V_{L3} + V_{S3}
\end{aligned} \tag{30}$$

## 2. Force and Torque Conditions

In addition to imposing continuity of velocity, which yielded the foregoing six equations, we must require that the force and torque about  $z$  on the cylinder vanish. A mathematical statement of vanishing force is

$$\sum_{i=1}^3 \int_{-t/2}^{t/2} \left[ \underline{x}_{oi} T_{xx}(0, y_i, z) + \underline{y}_{oi} T_{xy}(0, y_i, z) + \underline{z}_o T_{xz}(0, y_i, z) \right] dy_i = 0 \tag{31}$$

while the vanishing of torque about the  $z$  axis can be written

$$\sum_{i=1}^3 \int_{-t/2}^{t/2} (\underline{x}_{oi} d + \underline{y}_{oi} y_i) \times \left[ \underline{x}_{oi} T_{xx}(0, y_i, z) + \underline{y}_{oi} T_{xy}(0, y_i, z) \right] dy_i = 0 \tag{32}$$

Substituting the modal quantities from the previous section into (31) gives

$$\begin{aligned}
& \sum_{i=1}^3 \left\{ \underline{x}_{oi} \left[ \left( -1 + (1-\nu) \frac{k_z^2}{k_L^2} \right) \sqrt{t} V_{Li} + 2 \frac{k_z}{k_s} \sqrt{t} V_{Si} \right] \right. \\
& \quad + \underline{y}_{oi} \frac{\sqrt{\mu \rho} k_s^2 t^3}{12(1-\nu)} \left( \frac{I_{0i}}{N_0} - \frac{I_{1i}}{N_1} \right) \\
& \quad \left. + \underline{z}_o \sqrt{\mu \rho} t \left[ -2 \frac{k_z}{k_s} I_{Li} + \frac{2k_z^2 - k_s^2}{k_s^2} I_{Si} \right] \right\} = 0 \quad (33)
\end{aligned}$$

Decomposing  $\underline{x}_{oi}$ ,  $\underline{y}_{oi}$  for  $i = 2, 3$  along  $\underline{x}_{oi}$ ,  $\underline{y}_{oi}$  we can write (33) in component form as

$$\begin{aligned}
0 = & \left[ -1 + (1-\nu) \frac{k_z^2}{k_L^2} \right] \sqrt{t} (V_{L1} - \frac{1}{2} V_{L2} - \frac{1}{2} V_{L3}) + \frac{k_z}{k_s} \sqrt{t} (2V_{S1} - V_{S2} - V_{S3}) \\
& - \frac{\sqrt{\mu \rho} k_s^2 t^3}{8\sqrt{3}(1-\nu)} \left( \frac{I_{02} - I_{03}}{N_0} - \frac{I_{12} - I_{13}}{N_1} \right) \quad (34)
\end{aligned}$$

$$\begin{aligned}
0 = & \left[ -1 + (1-\nu) \frac{k_z^2}{k_L^2} \right] \frac{\sqrt{3t}}{2} (V_{L2} - V_{L3}) + \sqrt{3t} \frac{k_z}{k_s} (V_{S2} - V_{S3}) \\
& + \frac{\sqrt{\mu \rho} k_s^2 t^3}{24(1-\nu)} \left( \frac{2I_{01} - I_{02} - I_{03}}{N_0} - \frac{2I_{11} - I_{12} - I_{13}}{N_1} \right) \quad (35)
\end{aligned}$$

$$0 = -2 \frac{k_z}{k_s} (I_{L1} + I_{L2} + I_{L3}) + \frac{2k_z^2 - k_s^2}{k_s^2} (I_{S1} + I_{S2} + I_{S3}) \quad (36)$$

Substituting the modal quantities into (32) gives

$$\begin{aligned}
0 = & \sum_{i=1}^3 \left\{ \sqrt{\mu \rho} k_s \left( \frac{I_{0i}}{N_0} - \frac{I_{1i}}{N_1} \right) - j \left[ 1 + \frac{1-\nu}{2r-1} \left( 1 - 2 \frac{k_z^2}{k_s^2} \right) \right] \frac{V_{0i}}{N_0} \right. \\
& \left. - j \left[ 1 - \frac{1-\nu}{2r+1} \left( 1 - 2 \frac{k_z^2}{k_s^2} \right) \right] \frac{V_{1i}}{N_1} \right\} \quad (37)
\end{aligned}$$

### 3. Scattering Matrix Representation

Equations (28)-(30) and (34)-(37) are twelve equations describing the coupling between the twelve plate modes, four in each plate. Because of their complexity, we have chosen to use the equations to generate a scattering matrix for the junction. To this end we express the various voltages and currents in terms of the traveling-wave amplitudes  $a$  and  $b$  using (2) with  $x_i = 0$ .

Let the  $1 \times 4$  matrices  $\underline{a}_i$  and  $\underline{b}_i$  be defined as

$$\underline{a}_i = \begin{bmatrix} a_{Si} \\ a_{Li} \\ a_{0i} \\ a_{1i} \end{bmatrix}; \quad \underline{b}_i = \begin{bmatrix} b_{Si} \\ b_{Li} \\ b_{0i} \\ b_{1i} \end{bmatrix} \quad (38)$$

After substantial manipulation, one obtains from (28)-(30) and (34)-(37) equations relating the traveling-wave amplitudes in the form

$$\begin{bmatrix} A_{ij}^{(+)} \end{bmatrix} \begin{bmatrix} \underline{a}_1 \\ \underline{a}_2 \\ \underline{a}_3 \\ \underline{a}_4 \end{bmatrix} + \begin{bmatrix} A_{ij}^{(-)} \end{bmatrix} \begin{bmatrix} \underline{b}_1 \\ \underline{b}_2 \\ \underline{b}_3 \\ \underline{b}_4 \end{bmatrix} = 0 \quad (39)$$

The  $12 \times 12$  matrices  $\begin{bmatrix} A_{ij}^{(+)} \end{bmatrix}$  and  $\begin{bmatrix} A_{ij}^{(-)} \end{bmatrix}$  are defined in Table I. From (39), the  $12 \times 12$  scattering matrix  $S_{ij}$  relating the  $a$ 's and  $b$ 's as

$$\begin{bmatrix} b \end{bmatrix} = \begin{bmatrix} S_{ij} \end{bmatrix} \begin{bmatrix} a \end{bmatrix} \quad (40)$$

can be expressed in the form

TABLE I  
ELEMENTS OF THE 12x12 MATRICES  $[A_{ij}^{(+)}]$  DESCRIBING PLATE MODE COUPLING

$\mp m_1$	$\pm \frac{1}{2}$	$-\sqrt{3}m_{2,4}$	$-\sqrt{3}m_{3,5}$	$\mp 2m_1$	$\pm 1$	0	0	0	0	0	0
$\mp m_1$	$\pm \frac{1}{2}$	$\sqrt{3}m_{2,4}$	$\sqrt{3}m_{3,5}$	0	0	0	0	$\mp 2m_1$	$\pm 1$	0	0
$\mp \sqrt{3}m_1$	$\pm \frac{\sqrt{3}}{2}$	$m_{2,4}$	$m_{3,5}$	0	0	$2m_{2,4}$	$2m_{3,5}$	0	0	0	0
$\pm \sqrt{3}m_1$	$\mp \frac{\sqrt{3}}{2}$	$m_{2,4}$	$m_{3,5}$	0	0	0	0	0	0	$2m_{2,4}$	$2m_{3,5}$
0	0	$\mp 1$	$\mp m_6$	0	0	$\pm 1$	$\pm m_6$	0	0	0	0
0	0	0	0	0	0	$\mp 1$	$\mp m_6$	0	0	$\pm 1$	$\pm m_6$
$\sqrt{Z_S/Z_L}$	$k_z/k_s$	0	0	$-\sqrt{Z_S/Z_L}$	$-k_z/k_s$	0	0	0	0	0	0
0	0	0	0	$\sqrt{Z_S/Z_L}$	$k_z/k_s$	0	0	$-\sqrt{Z_S/Z_L}$	$-k_z/k_s$	0	0
$2m_7$	2	0	0	$-m_7$	-1	$\pm \sqrt{3}m_8$	$\mp \sqrt{3}m_9$	$-m_7$	-1	$\mp \sqrt{3}m_8$	$\pm \sqrt{3}m_9$
0	0	$\mp 2m_8$	$\pm 2m_9$	$\sqrt{3}m_7$	$\sqrt{3}$	$\pm m_8$	$\mp m_9$	$-\sqrt{3}m_7$	$-\sqrt{3}$	$\pm m_8$	$\mp m_9$
$\mp m_{10}$	$\mp k_z/k_s$	0	0	$\mp m_{10}$	$\mp k_z/k_s$	0	0	$\mp m_{10}$	$\mp k_z/k_s$	0	0
0	0	$\pm m_{12}$	$m_{11,13}$	0	0	$\pm m_{12}$	$m_{11,13}$	0	0	$\pm m_{12}$	$m_{11,13}$

$$m_1 = \frac{1}{2} \frac{k_z}{k_s} \sqrt{\frac{Z_L}{Z_S}}$$

$$m_{2,4} = \frac{\sqrt{t}}{2N_0(2r-1)} \left[ \frac{Z_0}{\sqrt{\mu\rho}} \mp k_s d \right] \sqrt{\frac{Z_L}{Z_0}}$$

$$m_{3,5} = \frac{-\sqrt{t}}{2N_1(2r+1)} \left[ \frac{Z_1}{\sqrt{\mu\rho}} \pm jk_s d \right] \sqrt{\frac{Z_L}{Z_1}}$$

$$m_6 = \frac{N_0}{N_1} \frac{2r-1}{2r+1} \sqrt{\frac{Z_0}{Z_1}}$$

$$m_7 = \frac{2k_z}{k_s \left[ -1 + (1-\nu)k_z^2/k_L^2 \right]} \sqrt{\frac{Z_S}{Z_L}}$$

$$m_8 = \frac{\sqrt{\mu\rho t} k_s^2 t^2}{12N_0(1-\nu)} \frac{1}{\left[ -1 + (1-\nu)k_z^2/k_L^2 \right]} \frac{1}{\sqrt{Z_L Z_0}}$$

$$m_9 = \frac{\sqrt{\mu\rho t} k_s^2 t^2}{12N_1(1-\nu)} \frac{1}{\left[ -1 + (1-\nu)k_z^2/k_L^2 \right]} \frac{1}{\sqrt{Z_L Z_1}}$$

$$m_{10} = \frac{1}{2} - \frac{k_z^2}{k_s^2}$$

$$m_{11,13} = \frac{N_0}{N_1} \sqrt{\frac{Z_1}{Z_0}} \frac{1 - \frac{1-\nu}{2r+1} (1 - 2k_z^2/k_s^2) \pm jk_s d \sqrt{\mu\rho} / Z_1}{1 + \frac{1-\nu}{2r-1} (1 - 2k_z^2/k_s^2)}$$

$$m_{12} = \frac{jk_s d \sqrt{\mu\rho} / Z_0}{1 + \frac{1-\nu}{2r-1} (1 - 2k_z^2/k_s^2)}$$

$$\begin{bmatrix} S_{ij} \end{bmatrix} = - \begin{bmatrix} A_{ij}^{(-)} \end{bmatrix}^{-1} \begin{bmatrix} A_{ij}^{(+)} \end{bmatrix} \quad (41)$$

Because the matrices  $\begin{bmatrix} A_{ij}^{(+)} \end{bmatrix}$  are complex, it is not useful to obtain analytic expressions for the elements  $S_{ij}$  of the scattering matrix. Instead, we have written computer programs for the elements  $A_{ij}^{(+)}$  and then used a computer to carry out numerically the matrix manipulations indicated in (41).

### C. Propagation Perpendicular to the Cell Axes ( $k_z = 0$ )

For the special case when there is no phase variation along  $z$ , the mode coupling equations (28)-(30) and (34)-(37) simplify. In this case the SH modes do not couple to the L, F(0) and F(1) modes. From (30) and (36), it is seen that coupling between the SH modes in the three plates is governed by the equations

$$\left. \begin{aligned} V_{S1} &= V_{S2} = V_{S3} \\ I_{S1} + I_{S2} + I_{S3} &= 0 \end{aligned} \right\} \quad (42)$$

Conditions (42) for the modal voltages and currents can be interpreted readily in terms of the interconnection of the equivalent modal transmission lines. Since the voltage is the same on all lines and the currents sum to zero, this transmission line connection is as shown in Figure 5, and is used subsequently to find the Bloch waves propagating in the honeycomb and polarized with particle motion along  $z$ .

While the coupling of the L, F(0) and F(1) modes is also simpler for  $k_z = 0$ , it is still not obvious or useful to introduce equivalent circuits interconnecting the equivalent transmission lines. In this case

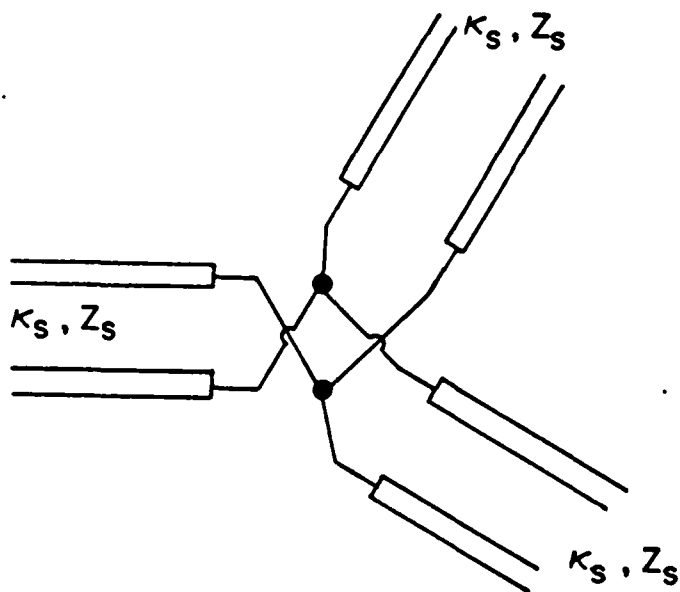


Figure 5. Equivalent network describing the coupling of SH modes at a Y joint.

it is still convenient to use the scattering matrix formation, where  $\underline{a}_i$  and  $\underline{b}_i$  are now  $1 \times 3$  matrices obtained by dropping  $a_{Si}$  and  $b_{Si}$  in (39). Also  $[A_{ij}^{(+)}]$  and  $[A_{ij}^{(-)}]$  are  $9 \times 9$  matrices, whose elements in Table II can be obtained by dropping the first, fifth and ninth columns, and seventh, eighth and eleventh rows of Table I. Also, the order of the rows has been changed, which does not effect the value of the scattering matrix.

Table II

Element of the 9x9 Matrices  $[A_{ij}^{(+)}]$  for the case  $k_z = 0$ 

2	0	0	-1	$\pm \mu_0$	$\mp \mu_1$	-1	$\mp \mu_0$	$\pm \mu_1$
0	$\mp \frac{2}{3} \mu_0$	$\pm \mu_1$	1	$\pm \frac{1}{3} \mu_0$	$\mp \frac{1}{3} \mu_1$	-1	$\pm \frac{1}{3} \mu_0$	$\mp \frac{1}{3} \mu_1$
0	$\mu_{2,4}$	$\mu_{3,5}$	0	$\mu_{2,4}$	$\mu_{3,5}$	0	$\mu_{2,4}$	$\mu_{3,5}$
$\pm \lambda_1$	$\sqrt{3} \lambda_{2,4}$	$\sqrt{3} \lambda_{3,5}$	$\pm 2 \lambda_1$	0	0	0	0	0
$\pm \sqrt{3} \lambda_1$	$-\lambda_{2,4}$	$-\lambda_{3,5}$	0	$-2 \lambda_{2,4}$	$-2 \lambda_{3,5}$	0	0	0
$\pm \lambda_1$	$-\sqrt{3} \lambda_{2,4}$	$-\sqrt{3} \lambda_{3,5}$	0	0	0	$\pm 2 \lambda_1$	0	0
$\pm \sqrt{3} \lambda_1$	$-\lambda_{2,4}$	$-\lambda_{3,5}$	0	0	0	0	$-2 \lambda_{2,4}$	$-2 \lambda_{3,5}$
0	$\pm 1$	$\pm \sigma$	0	$\mp 1$	$\mp \sigma$	0	0	0
0	0	0	0	$\pm 1$	$\pm \sigma$	0	$\mp 1$	$\mp \sigma$

$$\sigma = \frac{N_0}{N_1} \frac{2r-1}{2r+1} \sqrt{\frac{Z_0}{Z_1}}$$

$$\mu_{0,1} = \frac{N_L}{N_{0,1}} \frac{k_s^2 t^2}{4\sqrt{3}}$$

$$\mu_{2,4} = \frac{2r-v}{2r-1} \pm j \frac{k_s t}{2\sqrt{3}} \sqrt{\frac{\mu\rho}{Z_0}}$$

$$\mu_{3,5} = \frac{N_0}{N_1} \sqrt{\frac{Z_1}{Z_0}} \left[ \frac{2r+v}{2r+1} \mp j \frac{k_s t}{2\sqrt{3}} \sqrt{\frac{\mu\rho}{Z_1}} \right]$$

$$\lambda_1 = \frac{N_0}{N_L} \frac{2r-1}{1-v} \sqrt{\frac{\mu\rho}{Z_L}}$$

$$\lambda_{2,4} = \sqrt{\frac{Z_0}{Z_L}} \left[ 1 \pm j \frac{k_s t}{2\sqrt{3}} \sqrt{\frac{\mu\rho}{Z_0}} \right]$$

$$\lambda_{3,5} = \frac{N_0}{N_1} \frac{(2r-1)}{(2r+1)} \sqrt{\frac{Z_1}{Z_L}} \left[ -1 \pm j \frac{k_s t}{2\sqrt{3}} \sqrt{\frac{\mu\rho}{Z_1}} \right]$$



### III. BLOCH WAVES POLARIZED ALONG THE CELL AXES FOR PROPAGATION PERPENDICULAR TO THE CELL AXES

Because the SH plate waves do not couple to other modes at the Y junctions, and because they are non-dispersive, the Bloch waves composed of them have the simplest properties. We therefore consider this polarization first, in order to demonstrate the effects of the six-fold symmetry on propagation characteristics.

#### A. Formal Solution for Dispersion Characteristics

Starting with the equivalent circuit for the Y junction, as depicted in Figure 5, the equivalent network for a unit cell can be obtained. This network is drawn in Figure 6 and is seen to consist of four ports at which the voltages and currents  $V_i, I_i$  ( $i = 1 - 4$ ) are defined. The voltages and currents can be related via an impedance matrix. Because of the symmetry of the network, this relationship takes the form

$$\begin{bmatrix} V_1 \\ V_2 \\ V_3 \\ V_4 \end{bmatrix} = \begin{bmatrix} Z_{11} & Z_{12} & Z_{13} & Z_{13} \\ Z_{12} & Z_{11} & Z_{13} & Z_{13} \\ Z_{13} & Z_{13} & Z_{11} & Z_{12} \\ Z_{13} & Z_{13} & Z_{12} & Z_{11} \end{bmatrix} \begin{bmatrix} I_1 \\ I_2 \\ I_3 \\ I_4 \end{bmatrix} \quad (43)$$

By straightforward, but lengthy network analysis, it can be shown that

$Z_{11}, Z_{12}$  and  $Z_{13}$  are given by

$$Z_{11} = jZ_s \frac{1 - 10 \tan^2 \theta + 7 \tan^4 \theta}{6 \tan \theta (2 \tan^2 \theta - 1)} \quad (44)$$

$$Z_{12} = jZ_s \frac{1 - 5 \tan^2 \theta}{6 \cos^2 \theta \tan \theta (2 \tan^2 \theta - 1)} \quad (45)$$

$$Z_{13} = jZ_s \frac{1}{6 \cos^4 \theta \tan \theta (2 \tan^2 \theta - 1)} \quad (46)$$

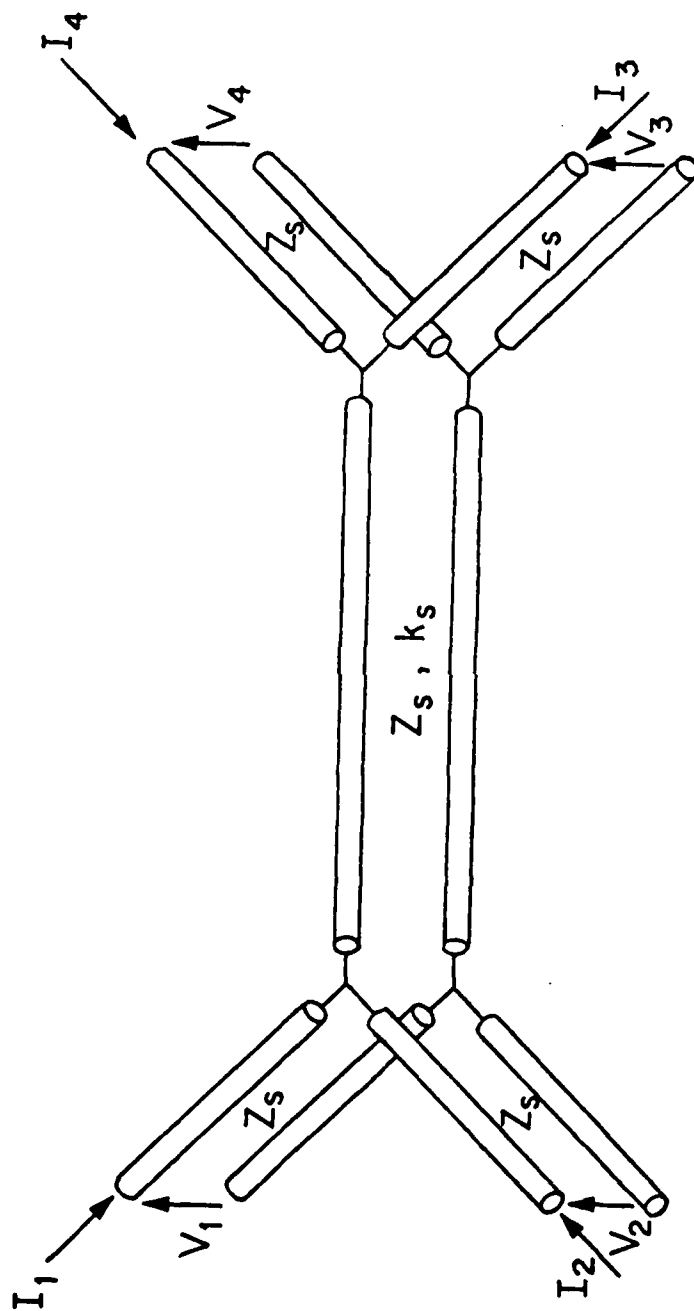


Figure 6. Equivalent circuit representing the SH modes in a unit cell of the honeycomb.

with

$$\theta = k_s w/2 . \quad (47)$$

We now consider the terminal voltages and currents  $V_i$  and  $I_i$  to be associated with a wave traveling through the core. Let

$$\underline{k} = \underline{x}_0 k_x + \underline{y}_0 k_y \quad (48)$$

be the wave vector of this wave. Also, let  $\underline{d}_1$  and  $\underline{d}_2$  be the basic translation vectors of the periodic structure, as shown in Figure 2, and given by

$$\underline{d}_{1,2} = \frac{3}{2} w \underline{x}_0 + \frac{\sqrt{3}}{2} w \underline{y}_0 \quad (49)$$

The Floquet assumption for periodic structures then implies the following relation between the terminal voltages and currents

$$\left. \begin{aligned} V_3 &= V_1 e^{-jk \cdot \underline{d}_1} \\ I_3 &= -I_1 e^{-jk \cdot \underline{d}_1} \\ V_4 &= V_2 e^{-jk \cdot \underline{d}_2} \\ I_4 &= -I_2 e^{-jk \cdot \underline{d}_2} \end{aligned} \right\} \quad (50)$$

The minus sign before  $I_1$  and  $I_2$  is due to the assumption that the currents are positive into the unit cell.

Substituting (50) into (43) one obtains four linear homogeneous equations in terms of the four unknowns  $V_1$ ,  $V_2$ ,  $I_1$  and  $I_2$ . Defining

$$\left. \begin{aligned} \psi_1 &= e^{-jk \cdot \underline{d}_1} \\ \psi_2 &= e^{-jk \cdot \underline{d}_2} \end{aligned} \right\} \quad (51)$$

the four equations may be written as

$$0 = \begin{bmatrix} Z_{11} - \psi_1 Z_{13} & Z_{12} - \psi_2 Z_{13} & -1 & 0 \\ Z_{12} - \psi_1 Z_{13} & Z_{11} - \psi_2 Z_{13} & 0 & -1 \\ Z_{13} - \psi_1 Z_{11} & Z_{13} - \psi_2 Z_{12} & -\psi_1 & 0 \\ Z_{13} - \psi_1 Z_{12} & Z_{13} - \psi_2 Z_{11} & 0 & -\psi_2 \end{bmatrix} \begin{bmatrix} I_1 \\ I_2 \\ V_1 \\ V_2 \end{bmatrix} \quad (52)$$

In order for (52) to have a non-trivial solution, the determinant of the 4x4 matrix must vanish. Setting the determinant equal to zero gives the dispersion equation of the form

$$(Z_{13}^2 - Z_{12}^2) \cos^2 \delta + 2Z_{13}(Z_{12} - Z_{11}) \cos \delta \cos \gamma + (Z_{11}^2 - Z_{13}^2) = 0 \quad (53)$$

where

$$\left. \begin{aligned} \delta &= \frac{\sqrt{3}}{2} w k_y \\ \gamma &= \frac{3}{2} w k_y \end{aligned} \right\} \quad (54)$$

This equation may then be solved numerically for its root  $k_x$  as a function of  $k_y$  and  $\omega$  or  $k_y$  as a function of  $k_x$  and  $\omega$ . The root corresponds to a wave in the core whose polarization is found from the eigen vector associated with the root.

Because of the periodicity of the honeycomb, (53) will have multiple solutions. Let  $\underline{u}_1$  and  $\underline{u}_2$  be reciprocal lattice vectors

$$\underline{u}_{1,2} = \frac{2\pi}{3w} \underline{x}_0 + \frac{2\pi}{\sqrt{3} w} \underline{y}_0 \quad (55)$$

so that

$$\underline{u}_i \cdot \underline{d}_j = 2\pi \delta_{ij} \quad (56)$$

where  $\delta_{ij}$  is the Kronecker delta. Thus, if a particular wavevector  $\underline{k}$  satisfies (53), then for any integers  $m$  and  $n$  the wavevector  $\underline{k} + m \underline{u}_1 + n \underline{u}_2$  will also satisfy (53). Also, due to the hexagonal symmetry of the honeycomb, a plot of  $k_x$  versus  $k_y$  for fixed  $\omega$  will have six-fold symmetry about the origin.

#### B. Numerical Evaluation of Propagation Characteristics

Numerical computations have been carried out for the dispersion curves  $k_x$  versus  $k_y$  for various fixed values of  $\omega$ . Because the SH wave velocity is independent of the wall thickness  $t$ , and because the impedances of all transmission lines in Figure 6 are the same, the results are independent of  $t$ . In addition, if the normalized frequency variable  $\theta$  in (47) is used, and the wave numbers  $k_x$  and  $k_y$  are multiplied by  $w/2$ , the computations will apply to all materials and honeycombs.

Due to the symmetry and periodicity of the honeycomb, the first quadrant in the  $k_x$ - $k_y$  plane of the first Brillouin zone is more than adequate to present the numerical results for the dispersion curves of  $k_x$  versus  $k_y$ . However, in order to explain the variation of the dispersion curves with frequency we have sketched the curves for several Brillouin zones in Figures 7(a), (b), (c). In Figure 7(a) we have indicated several reciprocal lattice points by dots and the vectors  $\underline{u}_1$  and  $\underline{u}_2$ . The dashed hexagon represents the first Brillouin zone. For low frequencies ( $\theta \ll 0.6155$ ), the dispersion curve is very nearly a circle of radius  $|\underline{k}| \frac{w}{2} = \sqrt{2} \theta_s$ . This value of  $|\underline{k}|$  corresponds to a wave velocity for the Bloch wave that is  $1/\sqrt{2}$  times the shear wave velocity of the honeycomb material. Because

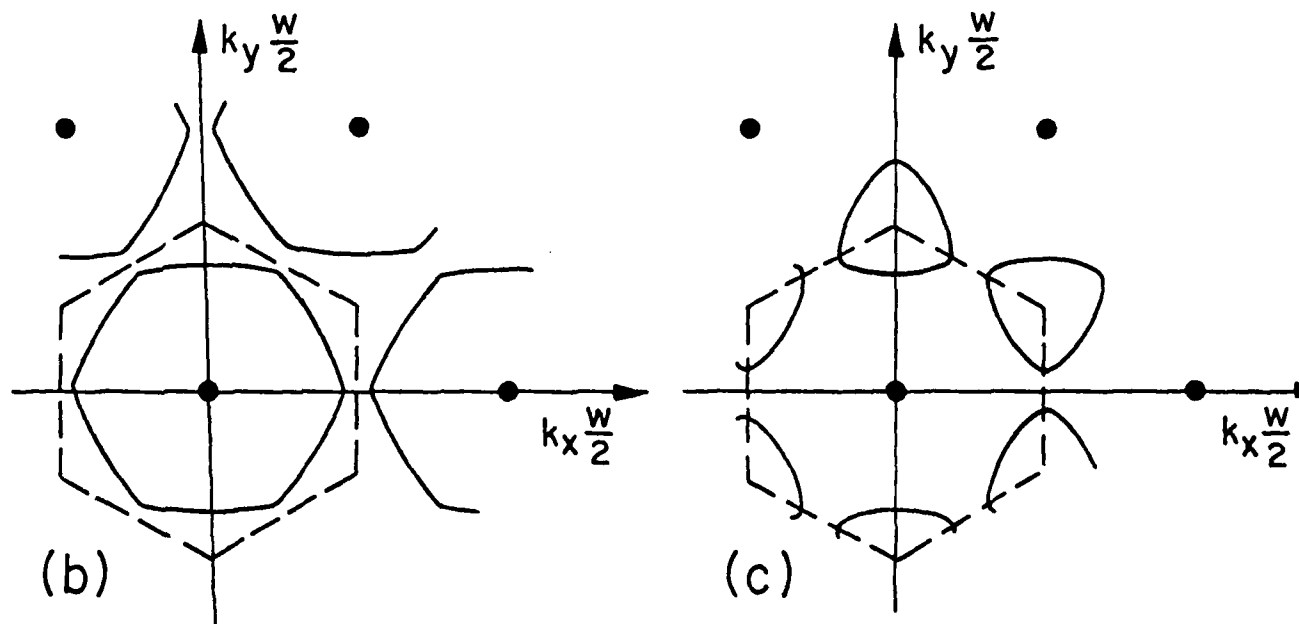
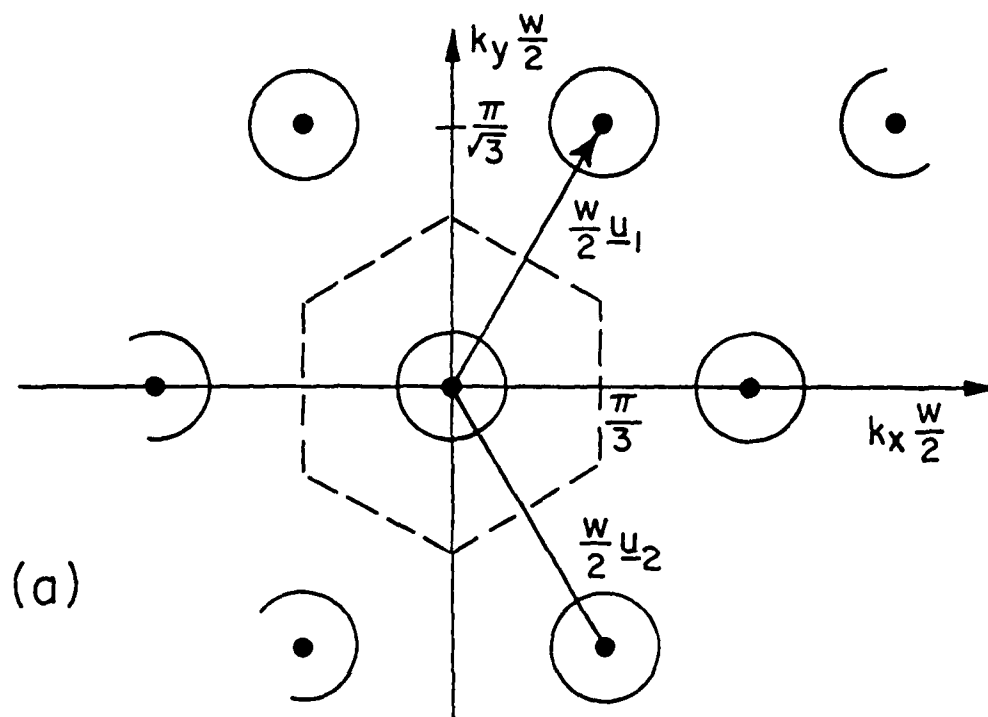


Figure 7. Reciprocal lattice points and slowness curves for normalized frequency  $\theta = k_s w/2$ : a) much less than 0.6155; b) just below 0.6155; and c) between 0.6155 and  $\pi/4 = 0.7854$ .

of the periodicity, the near-circles centered about each reciprocal lattice point are all locii of solutions of the dispersion relation, (53), as discussed after (56).

As the frequency variable  $\theta$  increases to just below 0.6155, the near-circular dispersion curves expand and distort into nearly hexagonal shapes, as indicated in Figure 7(b). At  $\theta = 0.6155$ , the tips of the hexagons touch. For  $0.6155 < \theta < \frac{\pi}{4} = 0.7854$ , the dispersion curves switch to being nearly triangular and centered about the apexes of the dashed hexagon, as shown in Figure 7(c). As  $\theta$  approaches  $\pi/4$ , the dispersion curves shrink to the points at the apexes of the hexagon. For  $\theta$  increasing above  $\pi/4$ , the change in the dispersion curves is reversed from that described above until for  $\theta$  approaching  $\pi/2$ , the curves become nearly circular as in Figure 7(a). For  $\theta$  increasing above  $\pi/2$ , the variation of the dispersion curves described above is repeated periodically with period  $\pi/2$ .

The actual dispersion curves in the first quadrant of the first Brillouin zone are plotted to scale in Figure 8, and are seen to be in agreement with the discussion of Figure 7. One of the features of these curves that may be important for NDE is the fact that in certain frequency ranges the waves are cut-off along  $\pm x$  and the four other directions making angles of  $60^\circ$  to the  $\pm x$  axes. These cut-off directions are ones parallel to a set of cell walls. However, the waves are never cut-off along  $y$ , and the six-fold related axes.

In order to show the cut-off behavior for propagation along  $x$ , we have plotted  $k_x$  as a function of  $\omega$  for the case  $k_y = 0$ . This plot is shown in

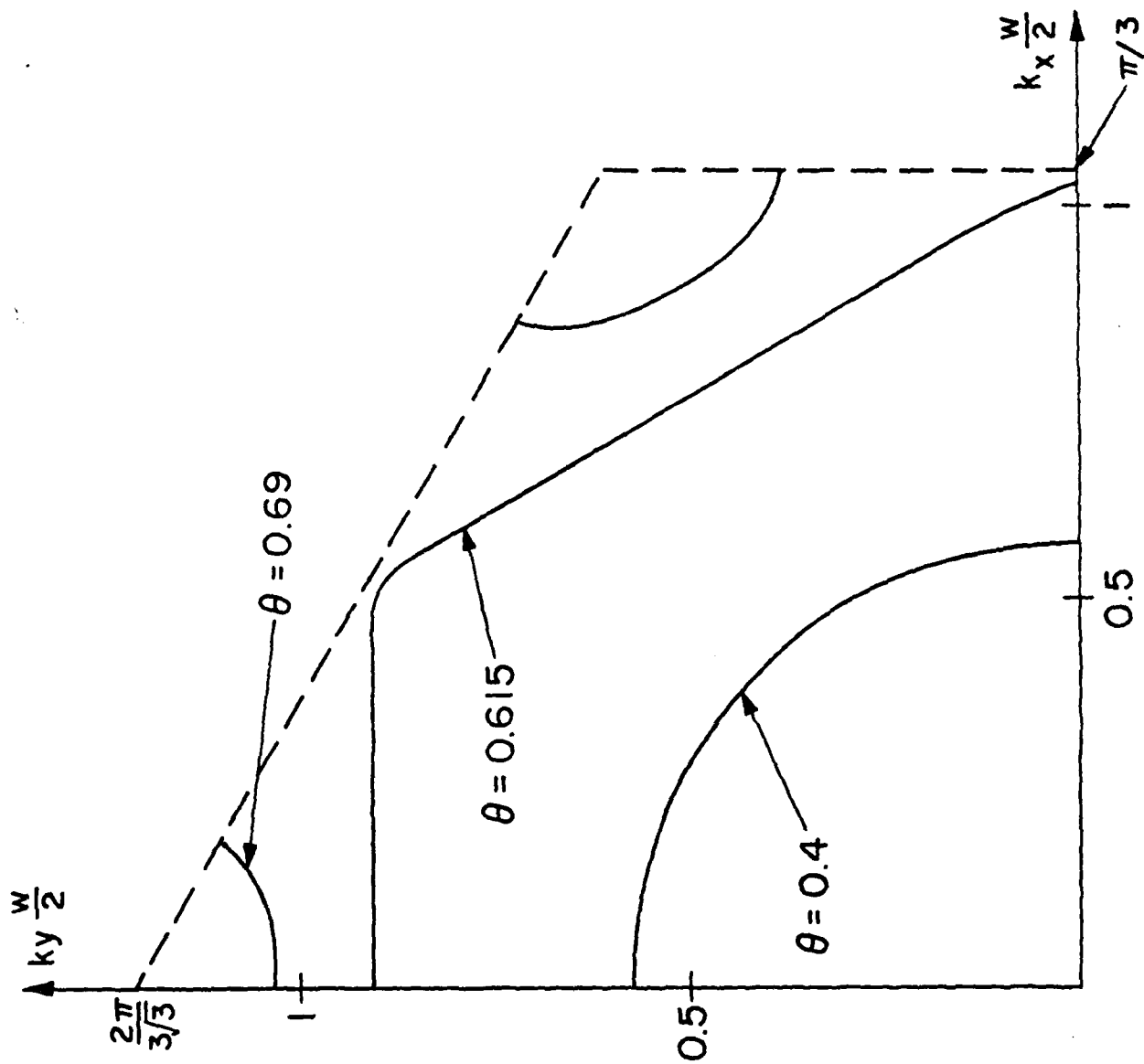


Figure 8. Slowness curves in the first quadrant of the Brillouin zone of the SH Bloch wave for several values of  $\theta = k_s w/2$ .



Figure 9, where  $k_x$  is real for  $0 < \theta < 0.6155$  and  $0.9553 > \theta > \pi/2$ . In the range  $0.6155 < \theta < 0.9553$ ,  $k_x$  is complex with real part given by  $\text{Re}(k_x \frac{w}{2}) = \pi/3$ . The curves are symmetric about  $\theta = \pi/4$ . For  $\theta$  outside the range plotted, the curves repeat with period  $\pi/2$ . By contrast, the plot in Figure 10 of  $k_y \frac{w}{2}$  versus the frequency variable  $k_s \frac{w}{2}$  for propagation along  $y$  does not show the presence of a stop band. The forward and backward wave regions connect directly at  $\theta = \pi/4$ . Again, the curves as a function of  $\theta$  repeat with period of  $\pi/2$ .

The variations in the magnitudes of particle velocity and stress within the unit cell is depicted in Figure 11 for propagation along  $x$  ( $k_y = 0$ ) and at a frequency just below cut-off. Because the fields are symmetric about the center of the unit cell, it is only necessary to plot the fields over one half of the cell. From Figure 11 it is seen that the center of the unit cell is almost stationary but has a large stress, as compared to points at the edges of the cell, for propagation along  $x$ . At the joint, however, the stress on the center branch is close to the maximum value in the cell. Note that the jump in stress at the joint is due to the fact that stress on the center branch is the sum of the stress on the two joining branches, and hence double that on Branch 1 for propagation along  $x$ . The high stress at the joint would facilitate NDE inspection for cracking at the joint, since a cracked joint would require stress to vanish and hence would be a large perturbation. For frequencies well below cut-off,  $|v_z|$  and  $|T_{zx}|$  are nearly uniform over the unit cell.

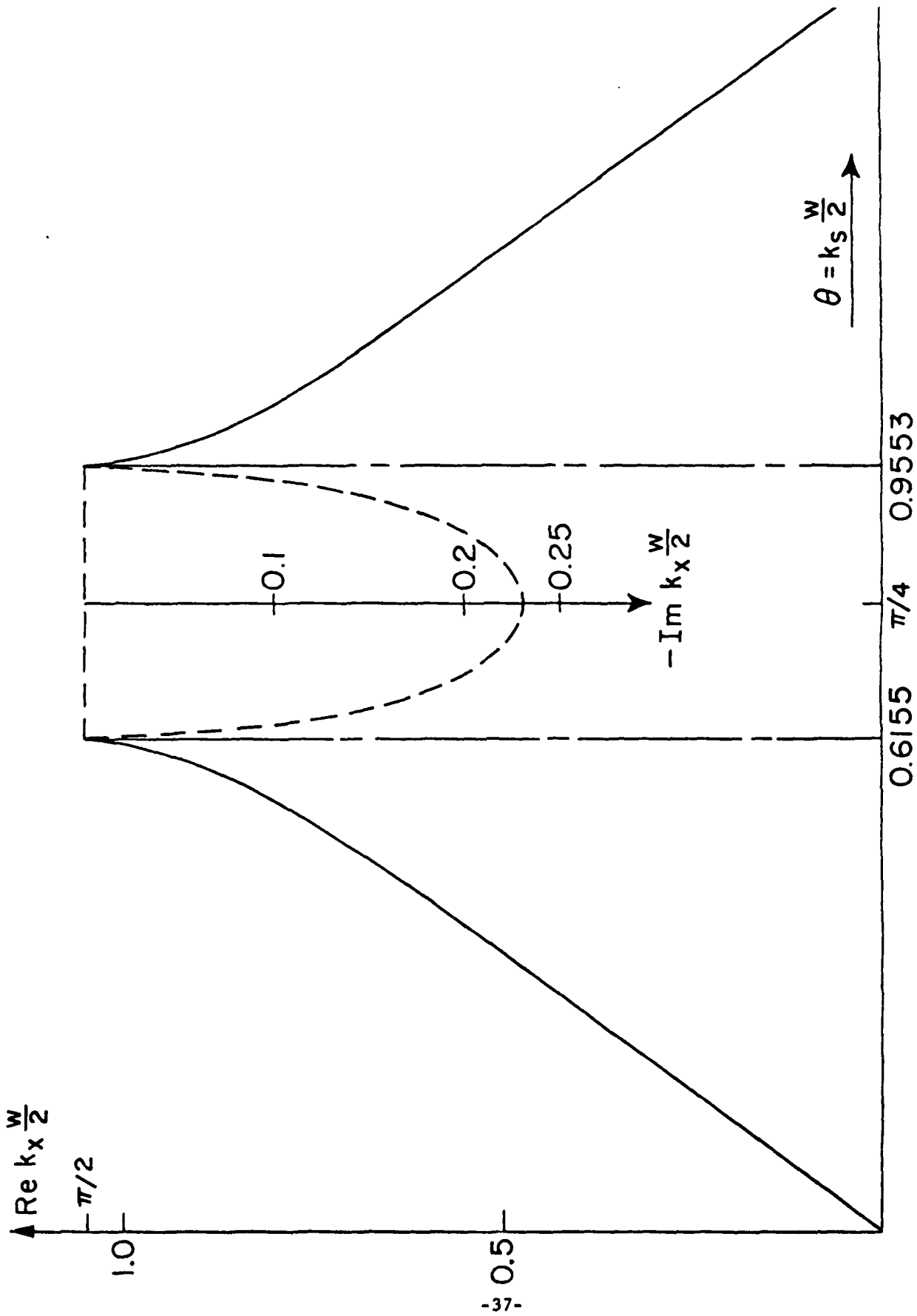


Figure 9. Dispersion curve for propagation along  $x$  of the SH Bloch wave. In the range  $0.6155 < k_x w/2 < 0.9553$ ,  $k_x$  is complex with real part given by  $\text{Re } k_x w/2 = \pi/3$ .

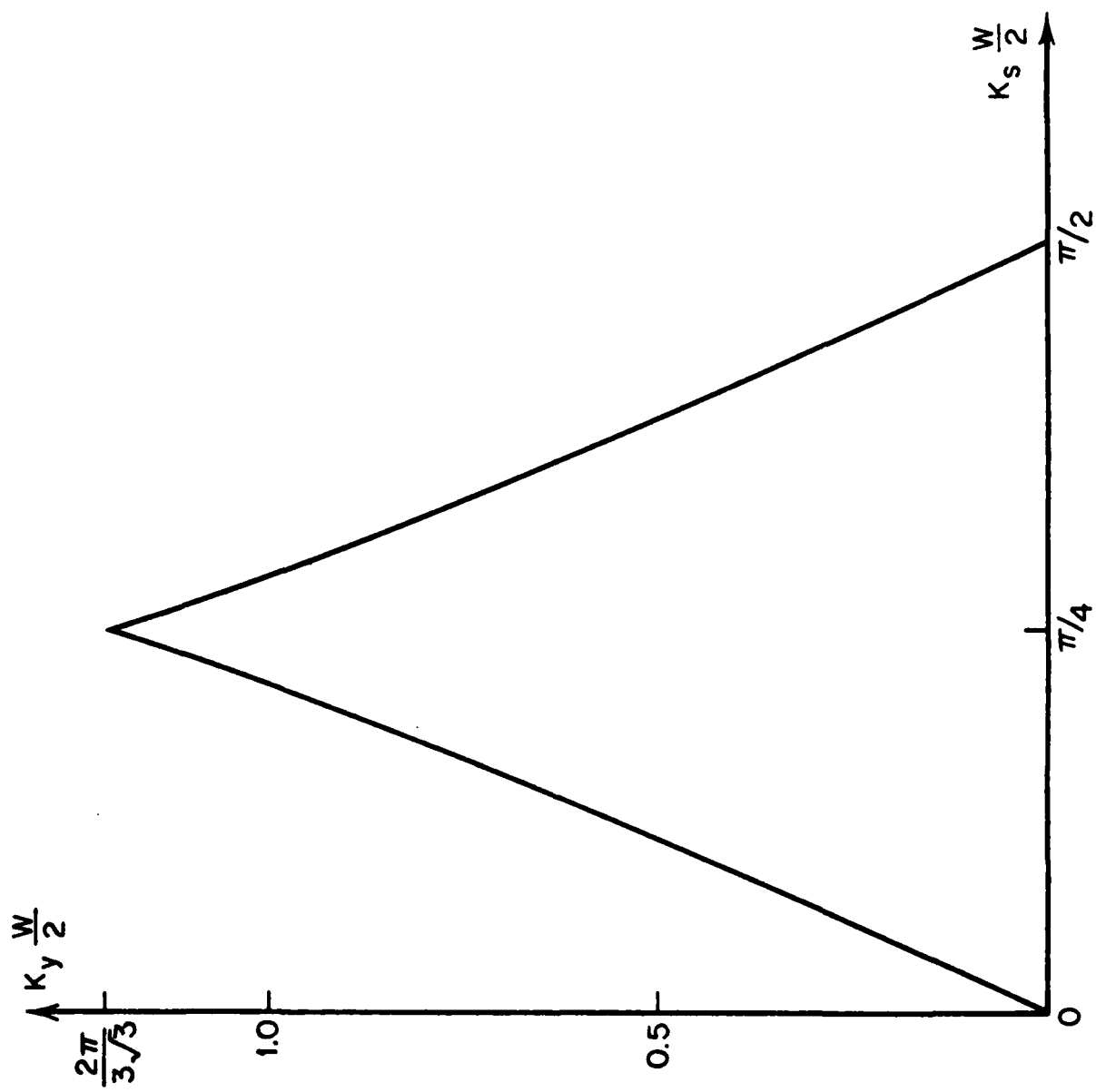


Figure 10. Dispersion curve for propagation along y of the SH Bloch wave.

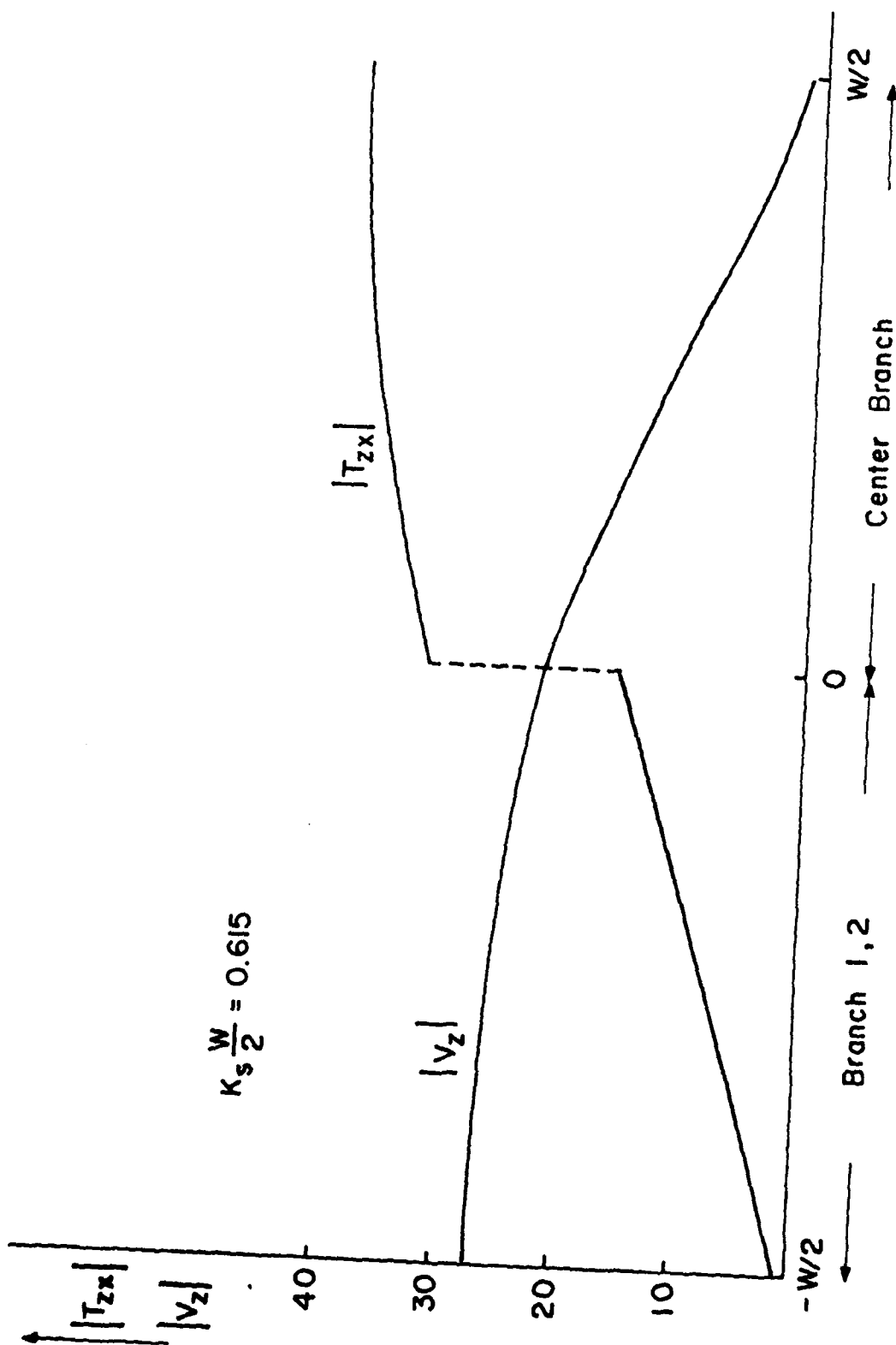


Figure 11. Magnitudes of particle velocity and stress along the left-half of a unit cell for an SH Bloch wave propagating along  $x$  at normalized frequency  $k_w/2 \approx 0.615$ . The curves for the right half of the unit cell are obtained by reflecting those showing about the point  $w/2$ .

#### IV. BLOCH WAVES POLARIZED PERPENDICULAR TO THE CELL AXES FOR PROPAGATION PERPENDICULAR TO THE CELL AXES

As discussed in Section II, waves propagating the plane perpendicular to the axis and polarized with particle velocity in the plane are composed of L(0), F(0) and F(1) modes in each cell wall. Because of the number of modes and the complexity of the equations describing their coupling at a Y joint, it is not readily apparent how to represent the coupling by an equivalent circuit, as was done for the case of particle motion along the cell axis. Instead, the scattering matrix representation (40) is used for the coupling. This representation is convenient since the necessary matrix manipulations can be indicated symbolically, whereas the actual evaluation is carried out numerically by a computer.

##### A. Formal Solution for the Propagation Characteristics

In order to facilitate the matrix manipulations, define the 1x3 column matrices

$$\underline{a}_i \equiv \begin{bmatrix} a_{Li} \\ a_{0i} \\ a_{1i} \end{bmatrix} ; \quad \underline{b}_i \equiv \begin{bmatrix} b_{Li} \\ b_{0i} \\ b_{1i} \end{bmatrix} , \quad (57)$$

where the a's and b's are the traveling wave amplitudes in the  $i = 1, 2, 3$  plate of Figure 3 evaluated at  $x_i = 0$ . Recall that the subscripts L, 0, 1 refer to the L, F(0) and F(1) modes and that the a's are the amplitudes of waves traveling in the  $-x_i$  direction towards the junction, while the b's are the amplitudes of waves traveling in the opposite direction. With this definition, the scattering matrix  $\underline{S}$  may be partitioned into 3x3 matrices  $\underline{S}_i$  as

$$\begin{bmatrix} \underline{b}_1 \\ \underline{b}_2 \\ \underline{b}_3 \end{bmatrix} = \begin{bmatrix} \underline{S}_1 & \underline{S}_2 & \underline{S}_3 \\ \underline{S}_3 & \underline{S}_1 & \underline{S}_2 \\ \underline{S}_2 & \underline{S}_3 & \underline{S}_1 \end{bmatrix} \begin{bmatrix} \underline{a}_1 \\ \underline{a}_2 \\ \underline{a}_3 \end{bmatrix} \quad (58)$$

The three-fold symmetry of the Y junction is evident in the form (58) of  $\underline{S}$ . In addition, all  $\underline{S}_i$  are symmetric and the two matrices  $\underline{S}_2$  and  $\underline{S}_3$  are the same except for the signs of the 12, 13, 21 and 23 elements. Because the F(1) mode is cut-off rather than propagating,  $\underline{S}$  is not a unitary matrix.

#### 1. Scattering Matrix for a Unit Cell

Figure 12 shows a unit cell divided into two identical portions, each consisting of three plates of length  $w/2$  connected at a Y joint. The numbering of the plates has been chosen for convenience in subsequent analysis. If  $\underline{a}_i'$  and  $\underline{b}_i'$  are the traveling wave amplitudes for the  $i^{\text{th}}$  plate at the end  $x_i = w/2$ , then

$$\underline{b}' = \underline{e} \underline{b}_i; \quad \underline{a}_i' = \underline{e}^{-1} \underline{a}_i \quad (59)$$

where  $\underline{e}$  is the 3x3 diagonal matrix

$$\underline{e} = \begin{bmatrix} e^{-jk_L w/2} & 0 & 0 \\ 0 & e^{-jk_{F0} w/2} & 0 \\ 0 & 0 & e^{-jk_{F1} w/2} \end{bmatrix} \quad (60)$$

Defining the 9x9 matrix  $\underline{S}'$  via the relation

$$\underline{S}' \equiv \begin{bmatrix} \underline{S}_1' & \underline{S}_2' & \underline{S}_3' \\ \underline{S}_3' & \underline{S}_1' & \underline{S}_2' \\ \underline{S}_2' & \underline{S}_3' & \underline{S}_1' \end{bmatrix} = \begin{bmatrix} \underline{e} & 0 & 0 \\ 0 & \underline{e} & 0 \\ 0 & 0 & \underline{e} \end{bmatrix} \begin{bmatrix} \underline{S} \\ \underline{S} \\ \underline{S} \end{bmatrix} \begin{bmatrix} \underline{e} & 0 & 0 \\ 0 & \underline{e} & 0 \\ 0 & 0 & \underline{e} \end{bmatrix} \quad (61)$$

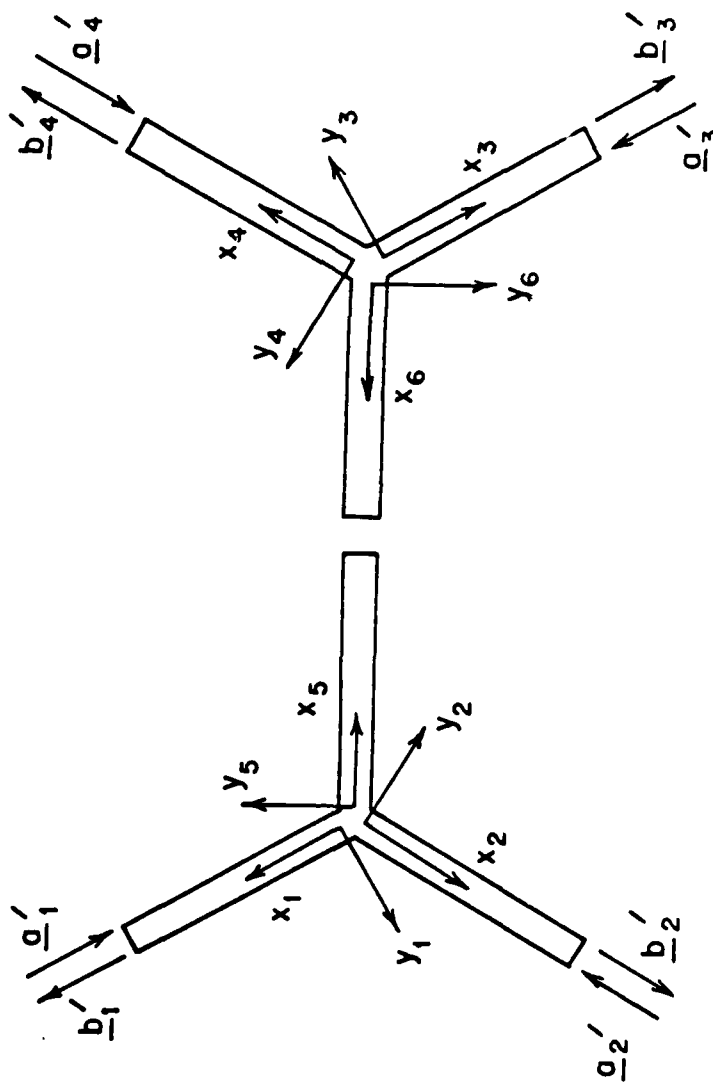


Figure 12. Two halves of a unit cell showing the numbering employed in the scattering matrix representation.

from (59) it follows for the left-hand half of the unit cell that

$$\begin{bmatrix} \underline{b}'_1 \\ \underline{b}'_2 \\ \underline{b}'_5 \end{bmatrix} = \underset{\sim}{S}' \begin{bmatrix} \underline{a}'_1 \\ \underline{a}'_2 \\ \underline{a}'_5 \end{bmatrix} \quad (62)$$

Similarly, for the right-hand half of the unit cell

$$\begin{bmatrix} \underline{b}'_3 \\ \underline{b}'_4 \\ \underline{b}'_6 \end{bmatrix} = \underset{\sim}{S}' \begin{bmatrix} \underline{a}'_3 \\ \underline{a}'_4 \\ \underline{a}'_6 \end{bmatrix} \quad (63)$$

The two halves of the unit cell are coupled at the mid-plane T, where the boundary conditions

$$T_{x_5 x_5} = T_{x_6 x_6}; \quad T_{x_5 y_5} = T_{x_6 y_6} \quad (64-a)$$

$$v_{x_5} = -v_{x_6}; \quad v_{y_5} = -v_{y_6} \quad (64-b)$$

must hold. From (1), (2) and (10), the first condition in (64-a) and the first condition in (64-b) are seen to imply for the L mode that

$$\left. \begin{aligned} (b'_{L5} + a'_{L5}) &= (b'_{L6} + a'_{L6}) \\ (b'_{L5} - a'_{L5}) &= - (b'_{L6} - a'_{L6}) \end{aligned} \right\} \quad (65)$$

since  $g_3$  and  $q_3$  are the same for both plates. Because the wave propagating in the  $+x_5$  direction on plate 5 becomes the wave propagating in the  $-x_6$  direction on plate 6, and vice versa, (65) is satisfied if



$$\left. \begin{aligned} b'_{L5} &= a'_{L6} \\ a'_{L5} &= b'_{L6} \end{aligned} \right\} \quad (66)$$

When considering the flexural mode  $F(0)$ , the second conditions in (64-a) and (64-b) are seen from (1), (2) and (12) to give

$$\left. \begin{aligned} (b'_{05} - a'_{05}) &= (b'_{06} - a'_{06}) \\ (b'_{05} + a'_{05}) &= - (b'_{06} + a'_{06}) \end{aligned} \right\} \quad (67)$$

since  $g_1$  and  $q_1$  are the same for both plates. However, the first conditions in (64-a) and (64-b) are seen from (1), (2) and (12) to give

$$\left. \begin{aligned} (b'_{05} + a'_{05})y_5 &= (b'_{06} + a'_{06})y_6 \\ (b'_{05} - a'_{05})y_5 &= -(b'_{06} - a'_{06})y_6 \end{aligned} \right\} \quad (68)$$

Noting that  $y_5 = -y_6$ , it is seen that (67) and (68) imply that

$$\left. \begin{aligned} b'_{05} &= -a'_{06} \\ a'_{05} &= -b'_{06} \end{aligned} \right\} , \quad (69)$$

where it is recalled that the  $+x_i$  traveling wave on one plate becomes the  $-x_i$  traveling wave on the other plate.

Similarly, for the  $F(1)$  mode

$$\left. \begin{aligned} b'_{15} &= -a'_{16} \\ a'_{15} &= -b'_{16} \end{aligned} \right\} . \quad (70)$$

Equations (66), (69) and (70) may be summarized as

$$\left. \begin{aligned} \underline{b}'_5 &= T \underline{a}'_6 \\ \underline{b}'_6 &= T \underline{a}'_5 \end{aligned} \right\} \quad (71)$$

where

$$T = \begin{bmatrix} 1 & 0 & 0 \\ 0 & -1 & 0 \\ 0 & 0 & -1 \end{bmatrix} \quad (72)$$

In order to join the scattering representations (62) and (63) using the conditions (66), (69) and (70) to obtain the scattering matrix for the unit cell, we write (62) and (63) in the form

$$\begin{bmatrix} \underline{b}'_1 \\ \underline{b}'_2 \\ \underline{b}'_3 \\ \underline{b}'_4 \end{bmatrix} = \begin{bmatrix} \underline{s}'_1 & \underline{s}'_2 & 0 & 0 \\ \underline{s}'_3 & \underline{s}'_1 & 0 & 0 \\ 0 & 0 & \underline{s}'_1 & \underline{s}'_2 \\ 0 & 0 & \underline{s}'_3 & \underline{s}'_1 \end{bmatrix} \begin{bmatrix} \underline{a}'_1 \\ \underline{a}'_2 \\ \underline{a}'_3 \\ \underline{a}'_4 \end{bmatrix} + \begin{bmatrix} \underline{s}'_3 & 0 \\ \underline{s}'_2 & 0 \\ 0 & \underline{s}'_3 \\ 0 & \underline{s}'_2 \end{bmatrix} \begin{bmatrix} \underline{a}'_5 \\ \underline{a}'_6 \end{bmatrix} \quad (73)$$

and

$$\begin{bmatrix} \underline{b}'_5 \\ \underline{b}'_6 \end{bmatrix} = \begin{bmatrix} \underline{s}'_2 & \underline{s}'_3 & 0 & 0 \\ 0 & 0 & \underline{s}'_2 & \underline{s}'_3 \end{bmatrix} \begin{bmatrix} \underline{a}'_1 \\ \underline{a}'_2 \\ \underline{a}'_3 \\ \underline{a}'_4 \end{bmatrix} + \begin{bmatrix} \underline{s}'_1 & 0 \\ 0 & \underline{s}'_1 \end{bmatrix} \begin{bmatrix} \underline{a}'_5 \\ \underline{a}'_6 \end{bmatrix} \quad (74)$$

Substituting (71) into (74), we can solve for  $\underline{a}'_5$  and  $\underline{a}'_6$  in terms of  $\underline{a}'_1$ ,  $\underline{a}'_2$ ,  $\underline{a}'_3$  and  $\underline{a}'_4$ . If this result is substituted into (73) we obtain the scattering representation for the unit cell as

$$\begin{bmatrix} \underline{b}'_1 \\ \underline{b}'_2 \\ \underline{b}'_3 \\ \underline{b}'_4 \end{bmatrix} = \begin{bmatrix} \underline{u} \end{bmatrix} \begin{bmatrix} \underline{a}'_1 \\ \underline{a}'_2 \\ \underline{a}'_3 \\ \underline{a}'_4 \end{bmatrix}, \quad (75)$$

where  $\underline{u}$  is the 12x12 matrix given by

$$\underline{u} = \begin{bmatrix} \underline{s}'_1 & \underline{s}'_2 & 0 & 0 \\ \underline{s}'_3 & \underline{s}'_1 & 0 & 0 \\ 0 & 0 & \underline{s}'_1 & \underline{s}'_2 \\ 0 & 0 & \underline{s}'_3 & \underline{s}'_1 \end{bmatrix} + \begin{bmatrix} \underline{s}'_3 & 0 \\ \underline{s}'_2 & 0 \\ 0 & \underline{s}'_3 \\ 0 & \underline{s}'_2 \end{bmatrix} \begin{bmatrix} -\underline{s}'_1 & \underline{T} \\ \underline{T} & -\underline{s}'_1 \end{bmatrix}^{-1} \begin{bmatrix} \underline{s}'_2 & \underline{s}'_3 & 0 & 0 \\ 0 & 0 & \underline{s}'_2 & \underline{s}'_3 \end{bmatrix} \quad (76)$$

Considerable symmetry exists within the  $\underline{u}$  matrix as a result of the symmetry of the unit cell. The 12x12 matrix  $\underline{u}$  may be partitioned into 3x3 submatrices and is found to have the form

$$\underline{u} = \begin{bmatrix} \underline{u}_1 & \underline{u}_2 & \underline{u}_3 & \underline{u}_4 \\ \underline{v}_2 & \underline{v}_1 & \underline{v}_4 & \underline{v}_3 \\ \underline{u}_3 & \underline{u}_4 & \underline{u}_1 & \underline{u}_2 \\ \underline{v}_4 & \underline{v}_3 & \underline{v}_2 & \underline{v}_1 \end{bmatrix} \quad (77)$$

In addition,

$$\underline{u}_1 = \underline{T} \underline{v}_1 \underline{T} \quad (78)$$

and  $\underline{u}_2$ ,  $\underline{u}_4$ ,  $\underline{v}_2$  and  $\underline{v}_4$  are symmetric while for  $i = 1, 3$  the transposes of the matrices  $\underline{u}_i$ ,  $\underline{v}_i$  satisfy

$$\left. \begin{aligned} \underline{\overline{u}}_1 &= \underline{T} \underline{u}_1 \underline{T} \\ \underline{\overline{v}}_1 &= \underline{T} \underline{v}_1 \underline{T} \end{aligned} \right\} \quad (79)$$

These symmetry properties can be used to check intermediate numerical results.

## 2. Application of Floquet Condition

Consider now a Bloch wave traveling through the core and let

$$\underline{k} = \underline{x}_0 k_x + \underline{y}_0 k_y \quad (80)$$

be its wave vector. The Floquet condition requires that the outward (inward) traveling waves at the end of plate 3 differ from the inward (outward) traveling waves at the end of plate 1 by the factor  $\exp(-jk \cdot \underline{d}_1)$ , where  $\underline{d}_1$  is a basis vector of the unit cell defined in (49). Because of the reversal of coordinate systems, an additional negative sign enters for the flexural modes, as discussed after (64). Thus, the Floquet condition takes the form

$$\left. \begin{aligned} \underline{b}'_3 &= e^{-jk \cdot \underline{d}_1} \underline{T} \underline{a}'_1 \\ \underline{a}'_3 &= e^{-jk \cdot \underline{d}_1} \underline{T} \underline{b}'_1 \end{aligned} \right\} \quad (81)$$

Similarly, the waves at the end of plate 4 can be related to those at the end of plate 2 via

$$\left. \begin{aligned} \underline{b}'_4 &= e^{-jk \cdot \underline{d}_2} \underline{T} \underline{a}'_2 \\ \underline{a}'_4 &= e^{-jk \cdot \underline{d}_2} \underline{T} \underline{b}'_2 \end{aligned} \right\} \quad (82)$$

Using  $\psi_1$  and  $\psi_2$ , as defined in (51), to represent the exponential factors, and substituting (81) and (82) into (75), one finds after suitable manipulation that

$$(\underline{u}' - \underline{\psi}) \begin{bmatrix} \underline{a}'_1 \\ \underline{a}'_2 \\ \underline{\psi}_1 \underline{b}'_1 \\ \underline{\psi}_2 \underline{b}'_2 \end{bmatrix} = 0 . \quad (83)$$

In (83)  $\underline{u}'$  and  $\underline{\psi}$  are 12x12 matrices that may be partitioned into 3x3 matrices in the form

$$\underline{u}' = \begin{bmatrix} \underline{\tilde{u}}_3 & \underline{\tilde{u}}_4 & \underline{v}_1 & \underline{v}_2 \\ \underline{\tilde{v}}_4 & \underline{\tilde{v}}_3 & \underline{u}_2 & \underline{u}_1 \\ \underline{u}_1 & \underline{u}_2 & \underline{u}_3^T & \underline{u}_4^T \\ \underline{v}_2 & \underline{v}_1 & \underline{v}_4^T & \underline{v}_3^T \end{bmatrix} \quad (84)$$

and

$$\underline{\psi} = \begin{bmatrix} \underline{\psi}_1 \underline{1} & 0 & 0 & 0 \\ 0 & \underline{\psi}_2 \underline{1} & 0 & 0 \\ 0 & 0 & \frac{1}{\underline{\psi}_1} \underline{1} & 0 \\ 0 & 0 & 0 & \frac{1}{\underline{\psi}_2} \underline{1} \end{bmatrix} \quad (85)$$

where  $\underline{1}$  is the 3x3 unit matrix.

In order for (83) to have non-trivial solutions, it is necessary that

$$\det(\underline{u}' - \underline{\psi}) = 0 , \quad (86)$$

which is the dispersion equation for the Bloch waves. Because the elements of  $\underline{u}'$  depend on frequency and  $\underline{\psi}$  contains the wavenumbers  $k_x$  and  $k_y$ , (86) is an equation of the form  $f(\omega, k_x, k_y) = 0$ , and can be solved for any one variable in terms of the other two. In practice, the equation is solved

numerically using a root search procedure. Numerical aspects of the solutions are discussed below.

#### B. Numerical Evaluation of the Propagation Characteristics

Computations were made for a honeycomb material having Poisson's ratio  $\nu = 0.32$ , which is the value for phenolic plastic cores, and a ratio  $w/t = 20$ . With these ratios fixed, the normalized wavenumbers  $k_x w/2$  and  $k_y w/2$  will depend on the shear wave velocity  $C_s$  of the honeycomb material only through the normalized frequency variable  $k_s w/2 = C_s w/2\omega$ . At very low frequencies, two propagating waves are found. One of these waves has velocity of propagation  $0.862 C_s$  that is independent of the direction of propagation. The second wave has velocity of propagation that varies from  $0.059 C_s$  to  $0.062 C_s$  as a function of the direction of propagation. The 5% variation in the calculated velocity is not thought to be meaningful, so that at low frequencies the propagation is isotropic in x-y plane. The two waves are referred to as the fast and slow Bloch wave solutions, respectively. For comparison, recall that at low frequencies the Bloch waves with particle motion along z propagate with velocity  $0.707 C_s$ . For convenience, we refer to the Bloch wave with particle motion along z as the Q-SV (quasi-shear vertical) wave. The properties of the fast and slow Bloch waves are discussed separately below.

##### 1. Fast-Wave Solution

The wavevector or slowness curves corresponding to the fast-wave solution are depicted in Figure 13. As discussed in connection with the Q-SV waves, the portion of  $k_x$ - $k_y$  space shown in Figure 13, which is the first quadrant of the first Brillouin zone, contains all of the information concerning the solutions of (86). The six-fold symmetry of the dispersion curves about the z-axis is

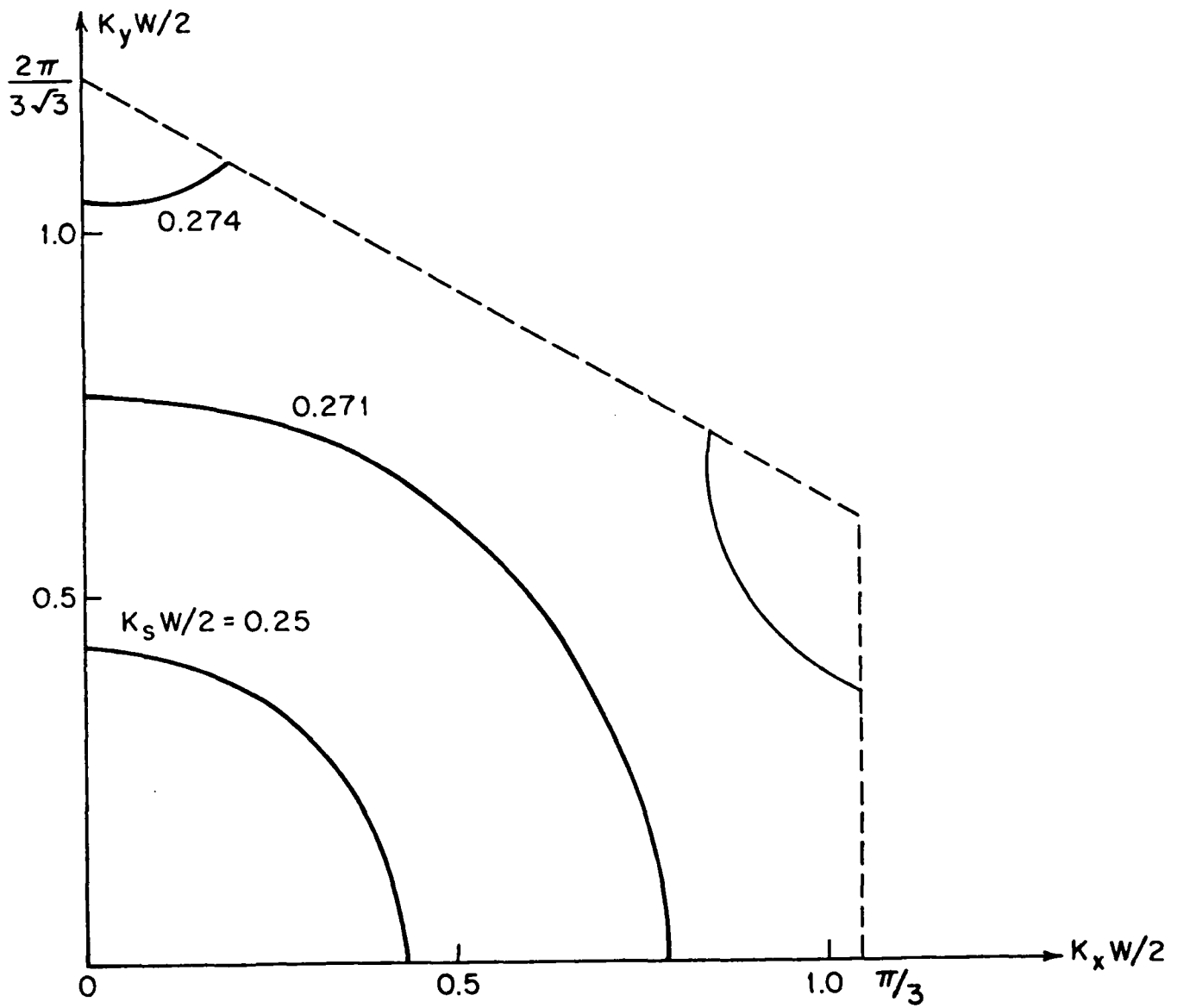


Figure 13. Slowness curves in the first quadrant of the first Brillouin zone for the fast Bloch wave for various values of normalized frequency  $k_s w/2$  within the first pass-band ( $w/t = 20$ ,  $\nu = 0.32$ ).

evident from the plots for the first quadrant, and is consistent with the hexagonal nature of the core. The normalized frequencies in Figure 13 lie in the first pass-band of the fast-wave.

The dispersion curves for propagation along  $x$  and along  $y$ , as well as their six-fold related directions, are shown in Figures 14 and 15. Above the first pass-band, the dispersion curves for propagation along both  $x$  and  $y$  consist of a complex set of stop bands and pass-bands that are not periodic with frequency, as in the case of SH waves. The non-periodicity results from the fact that the Bloch wave is composed of  $F(0)$  and  $F(1)$  plate modes, in addition to the  $L$  mode. Furthermore, the  $F(0)$  plate mode is dispersive, the coupling at the  $Y$  joints is frequency dependent, and the interaction between  $Y$  joints due to the  $F(1)$  mode decreases exponentially with the square root of frequency. The complexity associated with higher stop and pass-bands is discussed in connection with the slow-wave solution.

As the frequency increases from zero to the first stop band, the slowness curves of Figure 13 behave in a fashion similar to those of the SH wave. Thus, the curve changes from being circular about the origin to a figure that is slightly elongated along  $k_x$ , and six-fold related axes. At the normalized frequency  $k_g w/2 = 0.2735$ , the slowness curve touches the boundaries of the first Brillouin zone along  $k_x$  and related directions. In the range  $0.2735 < k_g w/2 < 0.275$ , the slowness curve becomes a series of closed shapes about the apexes of the Brillouin zone.



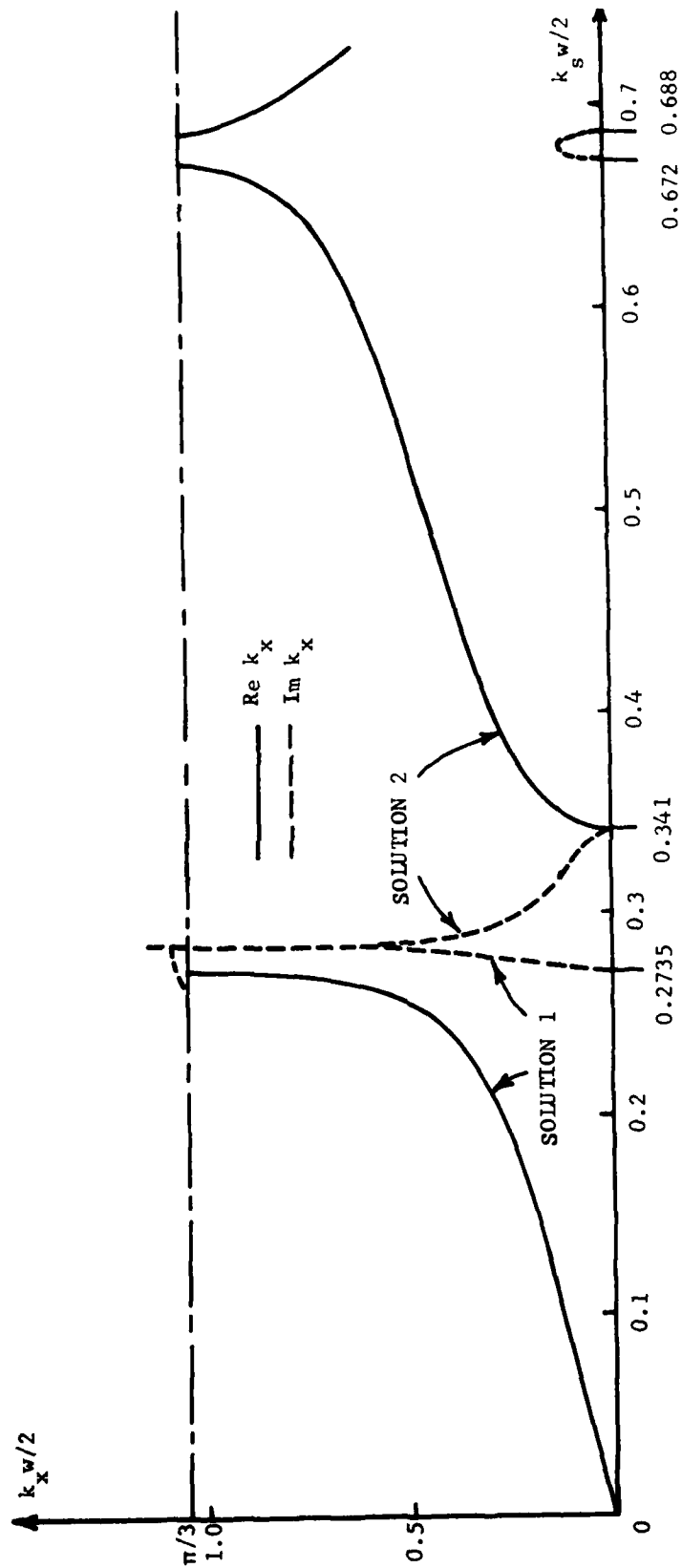


Figure 14. Dispersion curve for propagation along x of the fast Bloch wave ( $w/t = 20$ ,  $\nu = 0.32$ ).

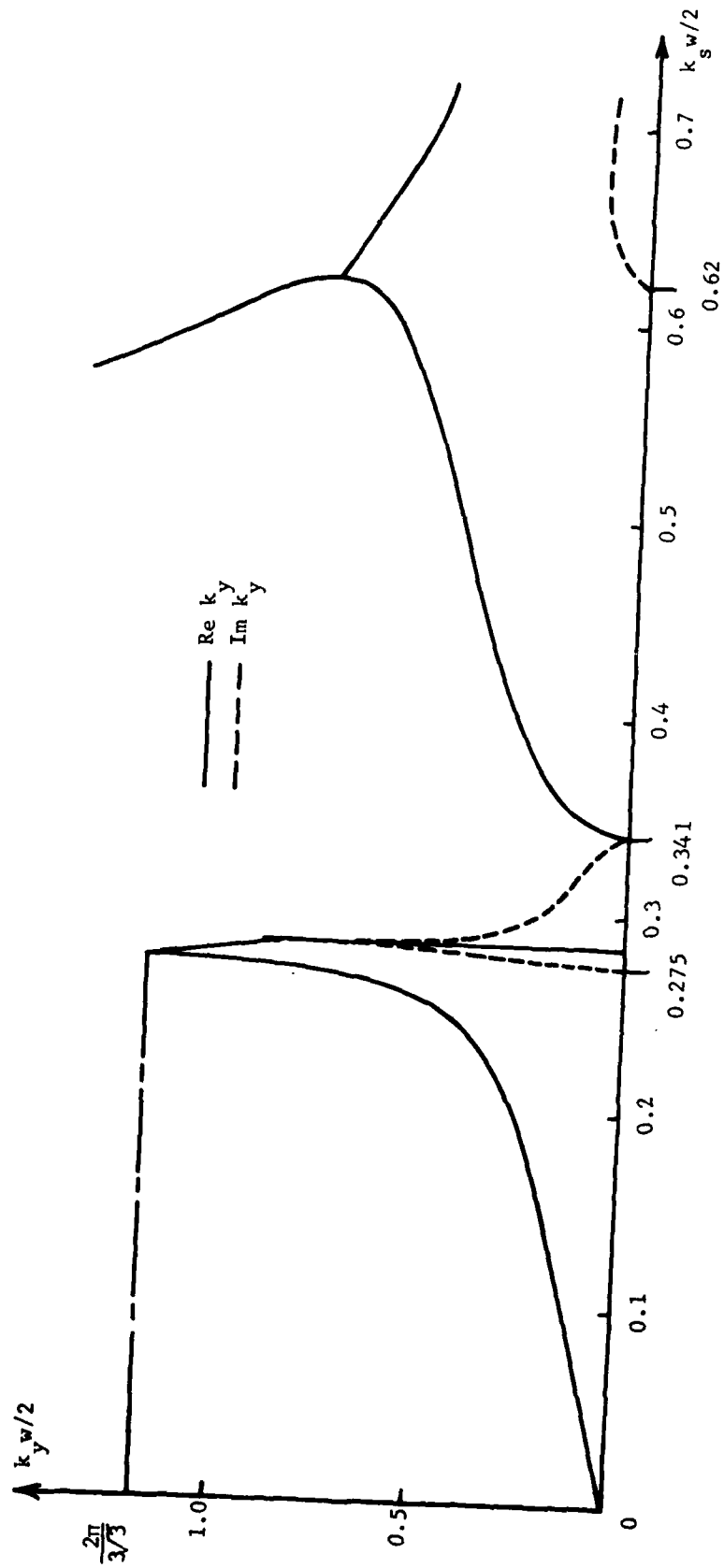


Figure 15. Dispersion curve for propagation along  $y$  of the fast Bloch wave ( $w/t = 20$ ,  $\nu = 0.32$ ).

While the fast Bloch wave has low frequency velocity greater than the Q-SV Bloch wave, it has a lower cutoff frequency for propagation along x and a cutoff band for propagation along y. In Figure 16 we plotted the normalized wavenumbers of the L, SH and F(0) plate modes, as well as the longitudinal wavenumber  $k_p$  of the honeycomb material versus normalized frequencies  $k_s w/2$  for  $w/t = 20$ . Were the fast Bloch wave to be composed solely of the L mode in the plates, at low frequencies, one would expect the fast Bloch wave velocity to be about 1.7 times that of the Q-SV Bloch wave; the value 1.7 being the ratios of the L mode to SH mode velocities. That the fast Bloch wave is only 1.2 times that of the Q-SV Bloch waves is therefore due to the presence of flexural waves. The coupling between F(0) and L modes increases with frequency, so that the phase shift due to the very slow F(0) mode becomes more significant in the Bloch wave at higher frequencies. This is believed to explain the rapid increase in dispersion above  $k_s w/2 = 0.20$ , and a value of cutoff frequency below that of the Q-SV Bloch wave.

In tracing the higher stop and pass-band behavior for propagation along x it was found that the first branch of dispersion equation became complex, as in Figure 14, and did not connect to the higher pass-band solution. The second pass-band results from a second branch of the dispersion equation, which is imaginary for frequencies below  $k_s w/2 = 0.341$ . For propagation along y, the same branch of the dispersion equation connected from the first to the second pass-band. The double solution for  $k_y$  in the vicinity of  $k_s w/2 = 0.6$  indicates that the slowness curves for these frequencies consist of several disconnected curves, and are probably quite complex. We have not however computed the shapes.

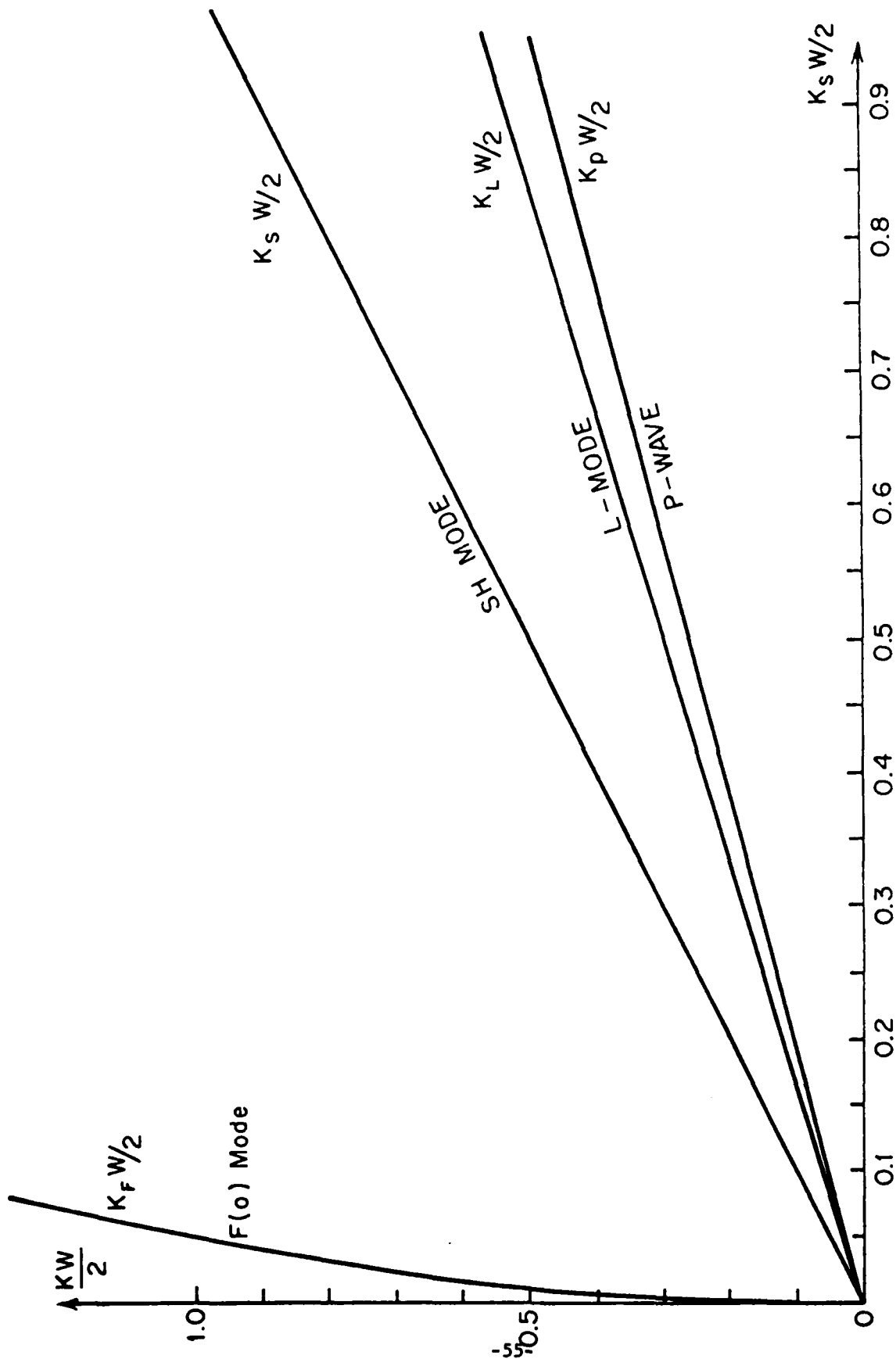


Figure 16. Dispersion curves for the various plate modes in the cell walls and for the longitudinal wave in the bulk honeycomb material ( $w/t = 20$ ,  $\nu = 0.32$ ).

The particle motion associated with the fast Bloch wave is depicted in Figures 17 and 18 for wave propagation along x and y, respectively, and a normalized frequency  $k_s w/2 = 0.2$ . These curves show, in exaggerated scale, the actual displacement of points along the center line of the plates at some instant of time. While the motion is different for the two directions of propagation, in each case it is symmetric about a line that is parallel to the direction of propagation and that divides the unit cell in half. In addition, the center of gravity of the unit cell appears to move back and forth in the direction of wave propagation. Because of this motion, the fast Bloch wave resembles a longitudinal wave in an elastic continuum, and will be referred to as the Q-P (quasi-longitudinal) wave.

## 2. Slow-Wave Solution

The slowness curves corresponding to the slow Bloch wave are depicted in Figure 19 for frequencies below the first stop band along y. The corresponding dispersion curves for propagation along x and along y are shown in Figures 20 and 21, respectively. It is seen that the behavior of the slowness curve is similar to that in Figures 8 and 13 for the Q-SV and Q-P Bloch waves. However, the anisotropy effects are much more pronounced and the normalized frequency  $k_s w/2$  for corresponding curves is an order of magnitude lower.

The difference in frequency can be understood by referring to the differences in the wavenumbers of the various plate modes, as shown in Figure 16. Over the ordinate range  $0 < k_{F0} w/2 < 1.0$ , the flexural wavenumber is more than 20 times larger than the shear wavenumber. If the slow Bloch wave were composed solely of the F(0) mode in the plates, one would expect its slowness curve at

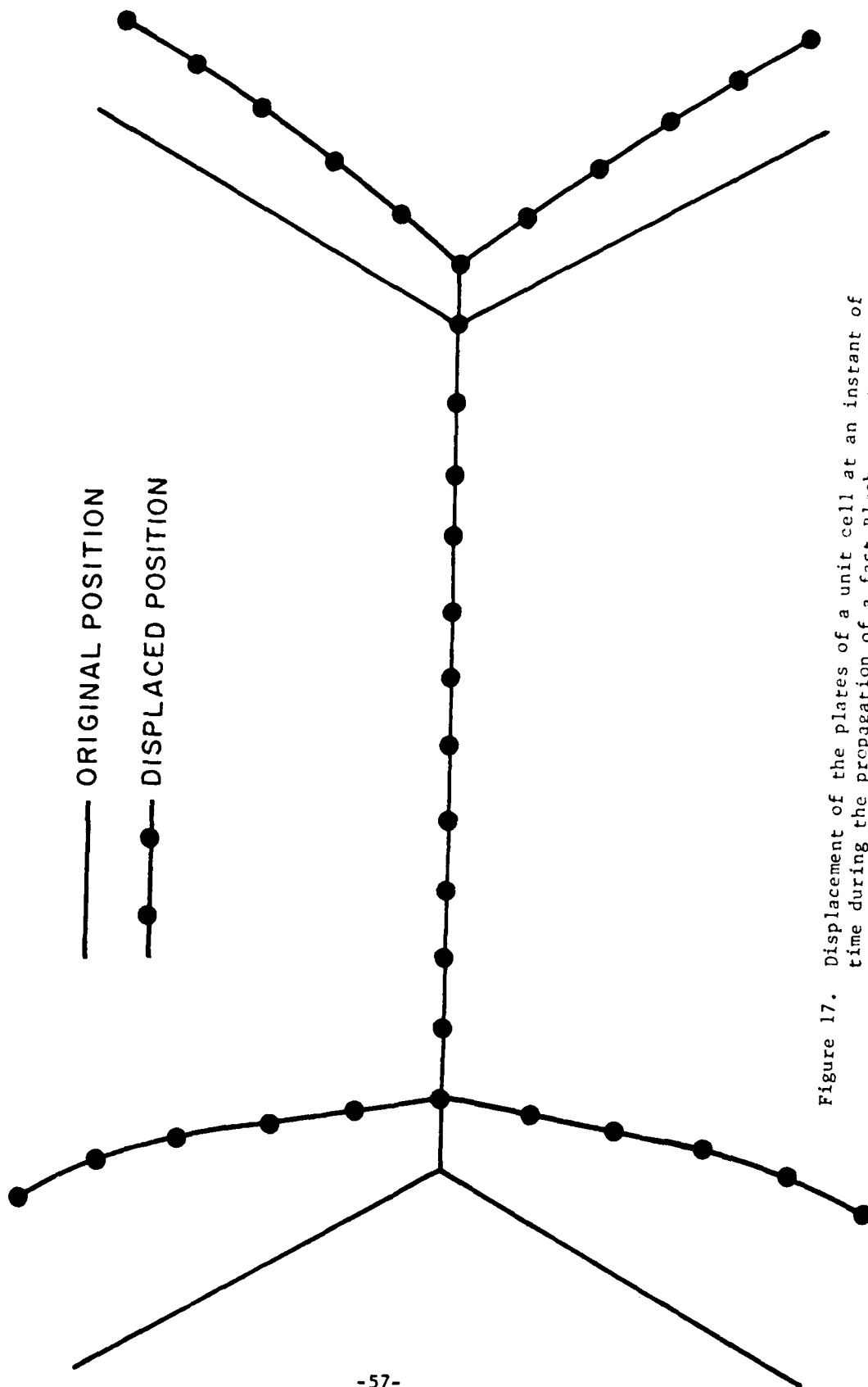


Figure 17. Displacement of the plates of a unit cell at an instant of time during the propagation of a fast Bloch wave in the  $x$  direction ( $w/t = 20$ ,  $\nu = 0.32$ ).

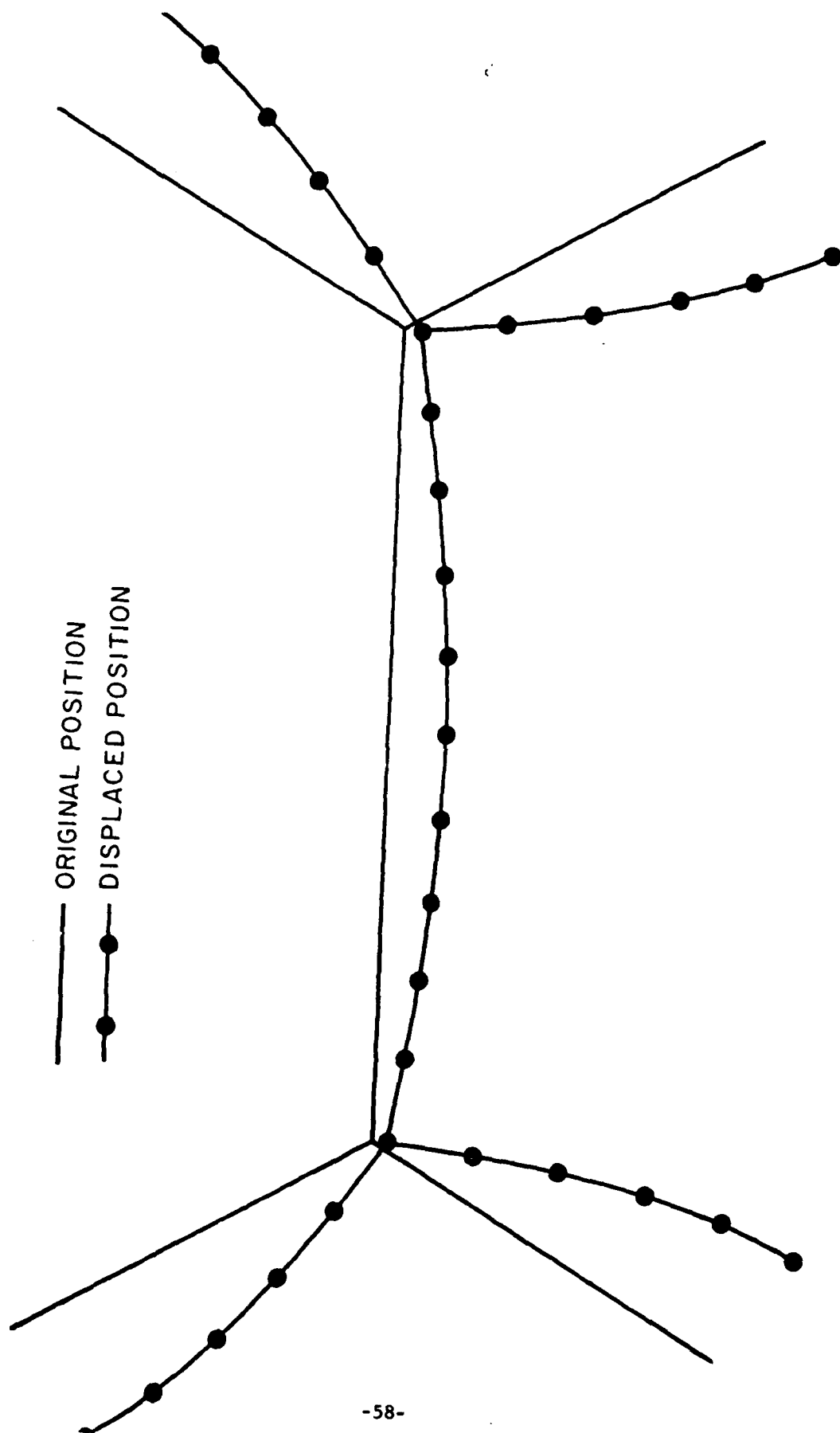


Figure 18. Displacement of the plates of a unit cell at an instant of time during the propagation of a fast Bloch wave in the  $y$  direction ( $w/t = 20$ ,  $\nu = 0.32$ ).

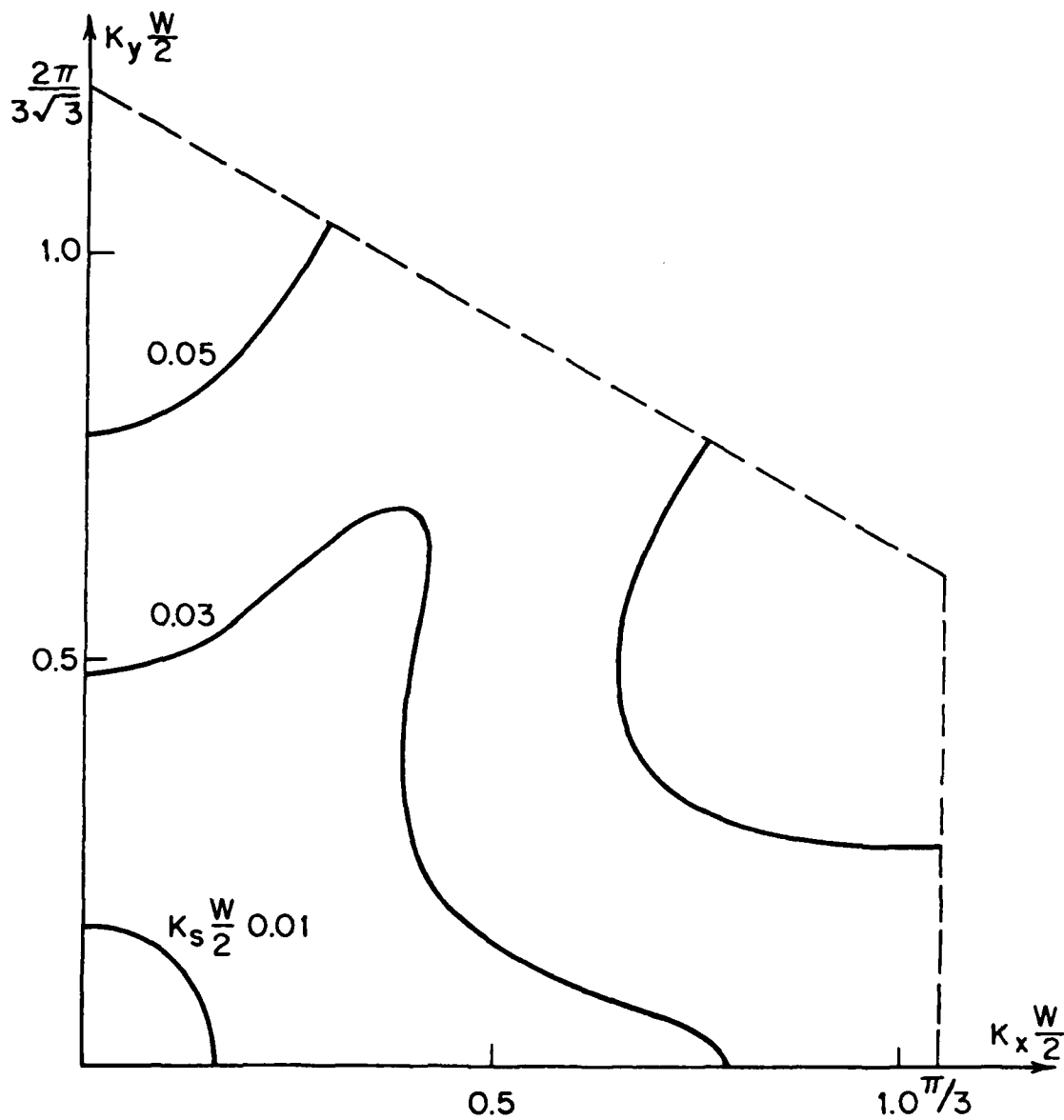


Figure 19. Slowness curves in the first quadrant of the first Brillouin zone for the slow Bloch wave for various values of normalized frequency  $k_s w/2$  within the first pass-band ( $w/t = 20$ ,  $v = 0.32$ ).



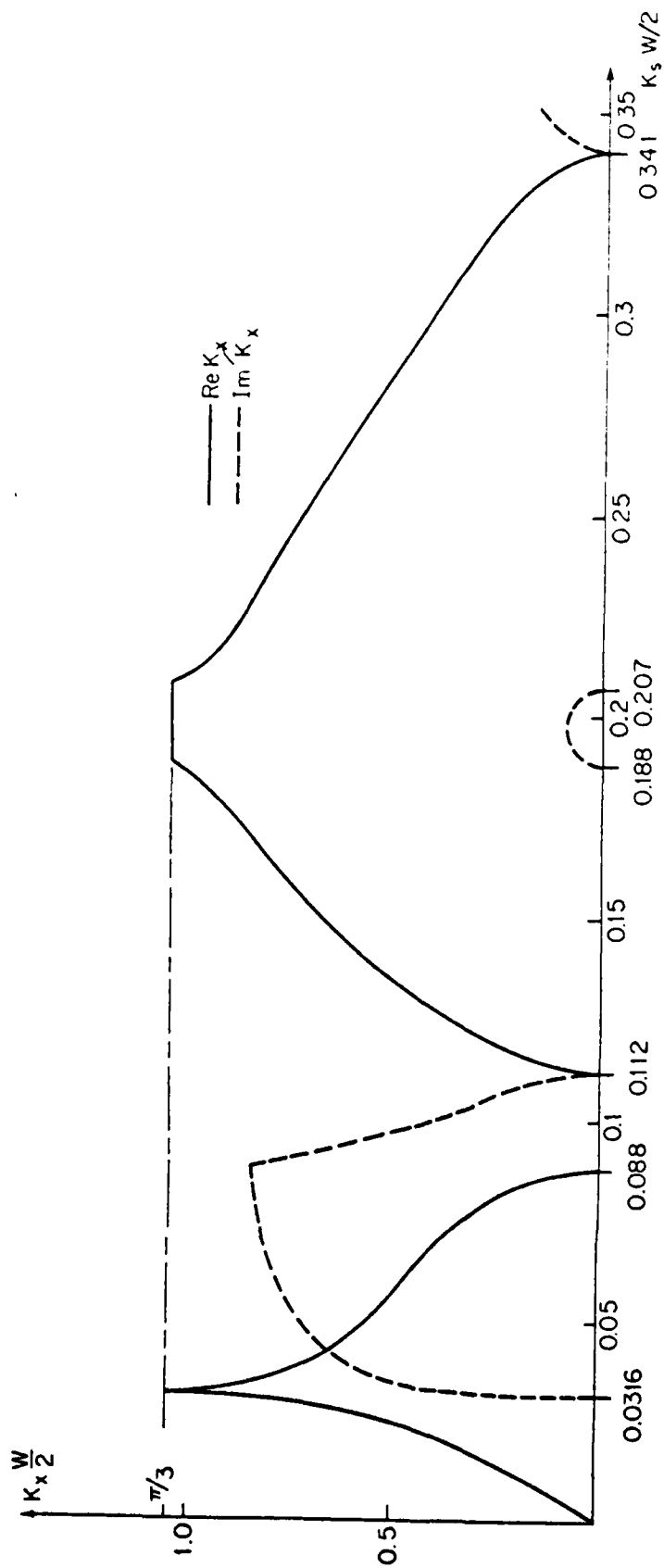


Figure 20. Dispersion curve for propagation along x of the slow Bloch wave ( $w/t = 20$ ,  $v = 0.32$ ).

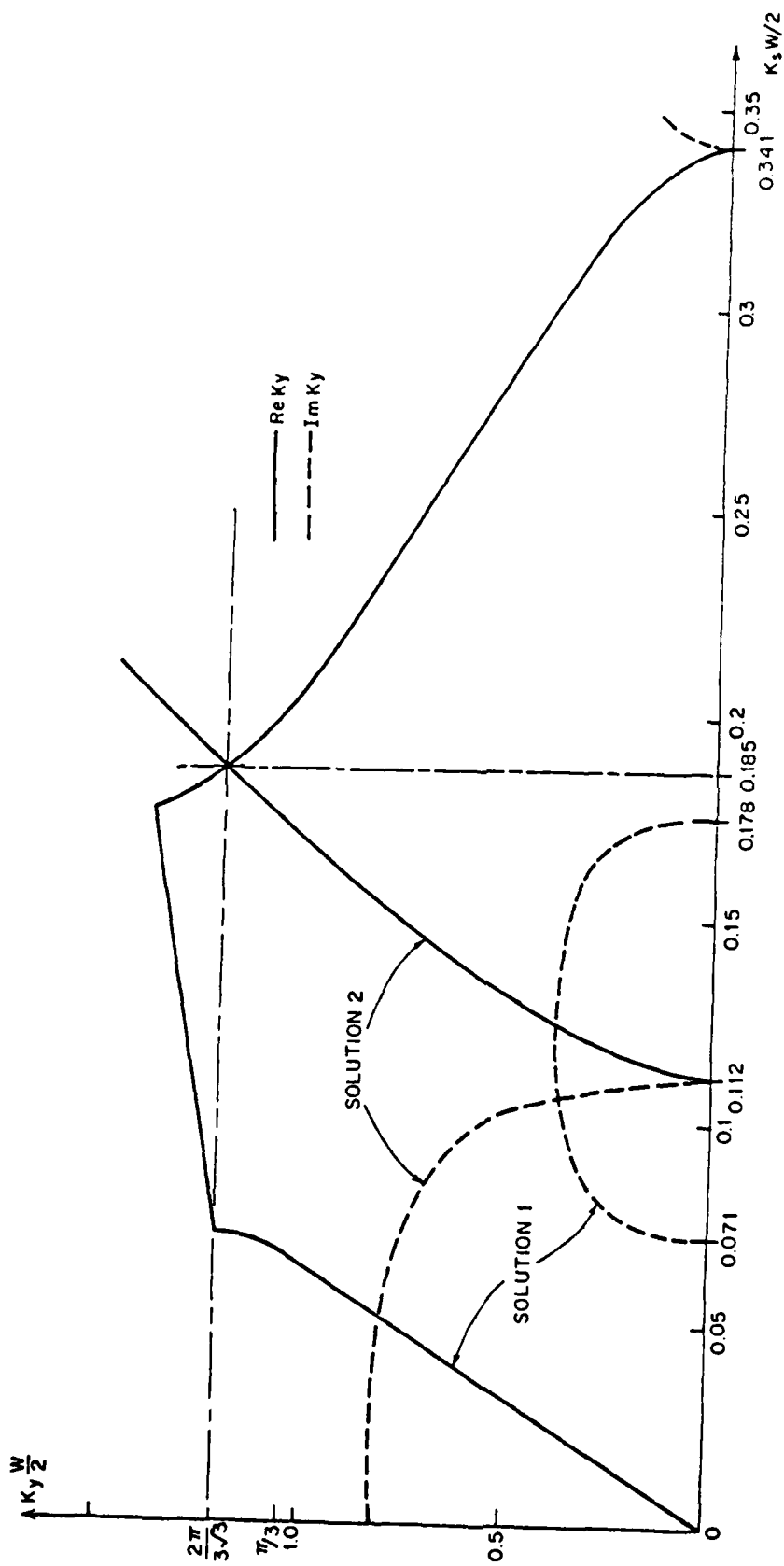


Figure 21. Dispersion curve for propagation along  $y$  of the slow Bloch wave ( $w/t = 20$ ,  $v = 0.32$ ).

frequency  $f_1$  to have a shape similar to that of the Q-SV Bloch wave at frequency greater than  $20 f_1$ . However, the frequency ratio is somewhat less than 20 due to the presence of the L and F(1) modes.

As the frequency increases from zero to the first stop band for propagation along x, the shape of the slowness curves of Figure 19 changes from circular about the origin to a figure that is elongated along  $k_x$ , and six-fold related axes. At the normalized frequency  $k_s w/2 = 0.0316$ , the slowness curve touches the boundary of the Brillouin zone. In the range  $0.0316 < k_s w/2 < 0.0671$ , the slowness curve breaks into a series of closed curves about the apexes of the first Brillouin zone. These curves shrink to a point at  $k_s w/2 = 0.0671$ . For frequencies in the range  $0.0671 < k_s w/2 < 0.112$ , the Bloch wave is evanescent for all directions of propagation in the x-y plane.

The particle motion associated with the slow Bloch wave in the first pass-band is depicted in Figures 22 and 23 for propagation along x and y respectively at normalized frequency  $k_s w/2 = 0.03$ . In these figures we have plotted, at an exaggerated scale, the actual displacement of the centers of plates comprising a unit cell at a particular instant in time. From Figure 22, it is seen for propagation along x the motion is almost transverse to the direction of propagation. From Figure 23 it is seen that the motion for propagation along y is anti-symmetric about a plane through the center of the cell and parallel to y, and has a strong shear component. On the basis of cell motion, we can identify the slow Bloch wave at low frequency as a shear wave in an elastic continuum, and will refer to it as the Q-SH (quasi-shear horizontal) wave.

For frequencies above the first pass-band, the dispersion curves of Figures 20 and 21 exhibit a complex series of stop bands and pass-bands, which are not periodic in frequency. For the case of propagation along x, a single

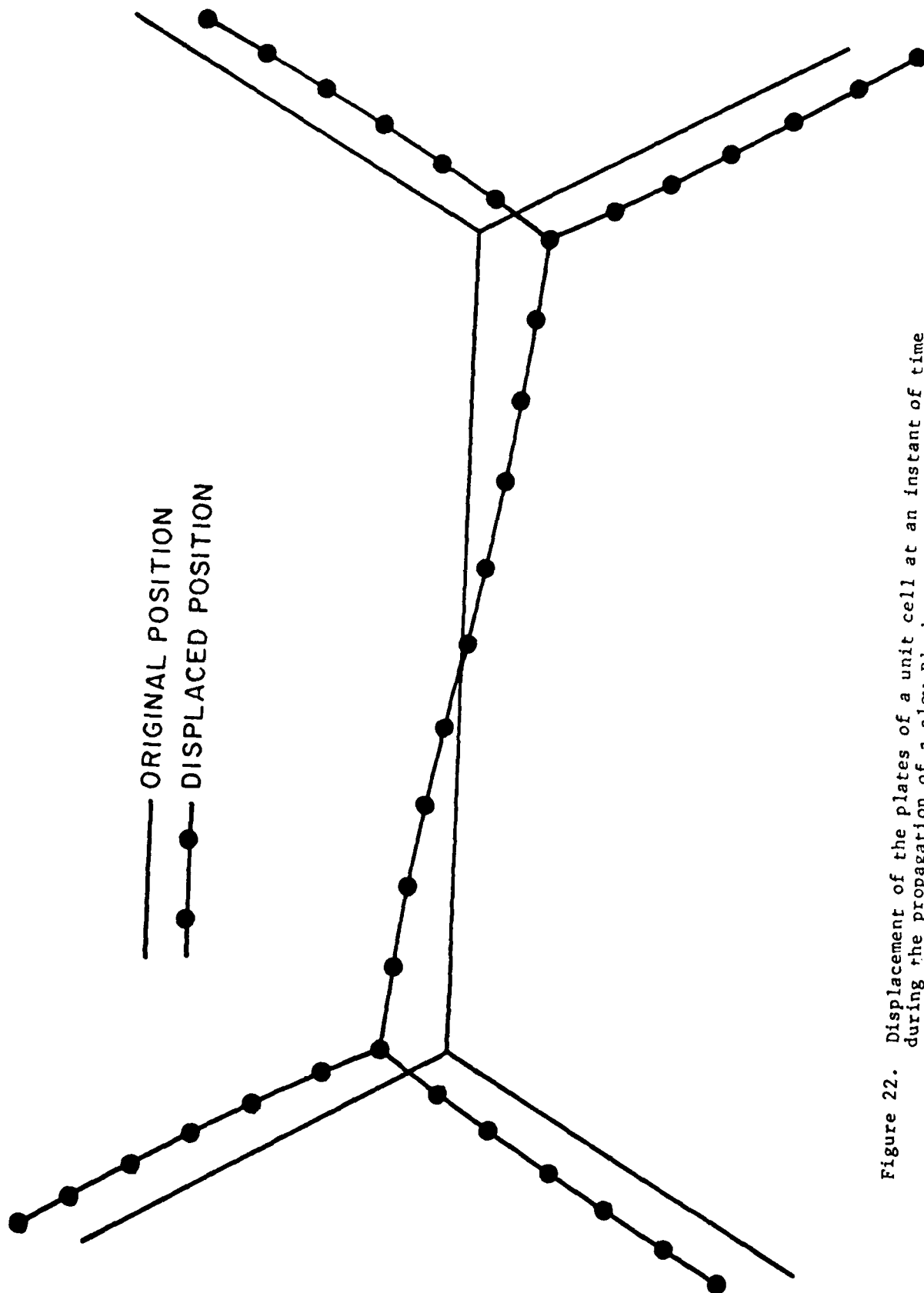


Figure 22. Displacement of the plates of a unit cell at an instant of time during the propagation of a slow Bloch wave in the  $x$  direction ( $w/t = 20$ ,  $v = 0.32$ ).

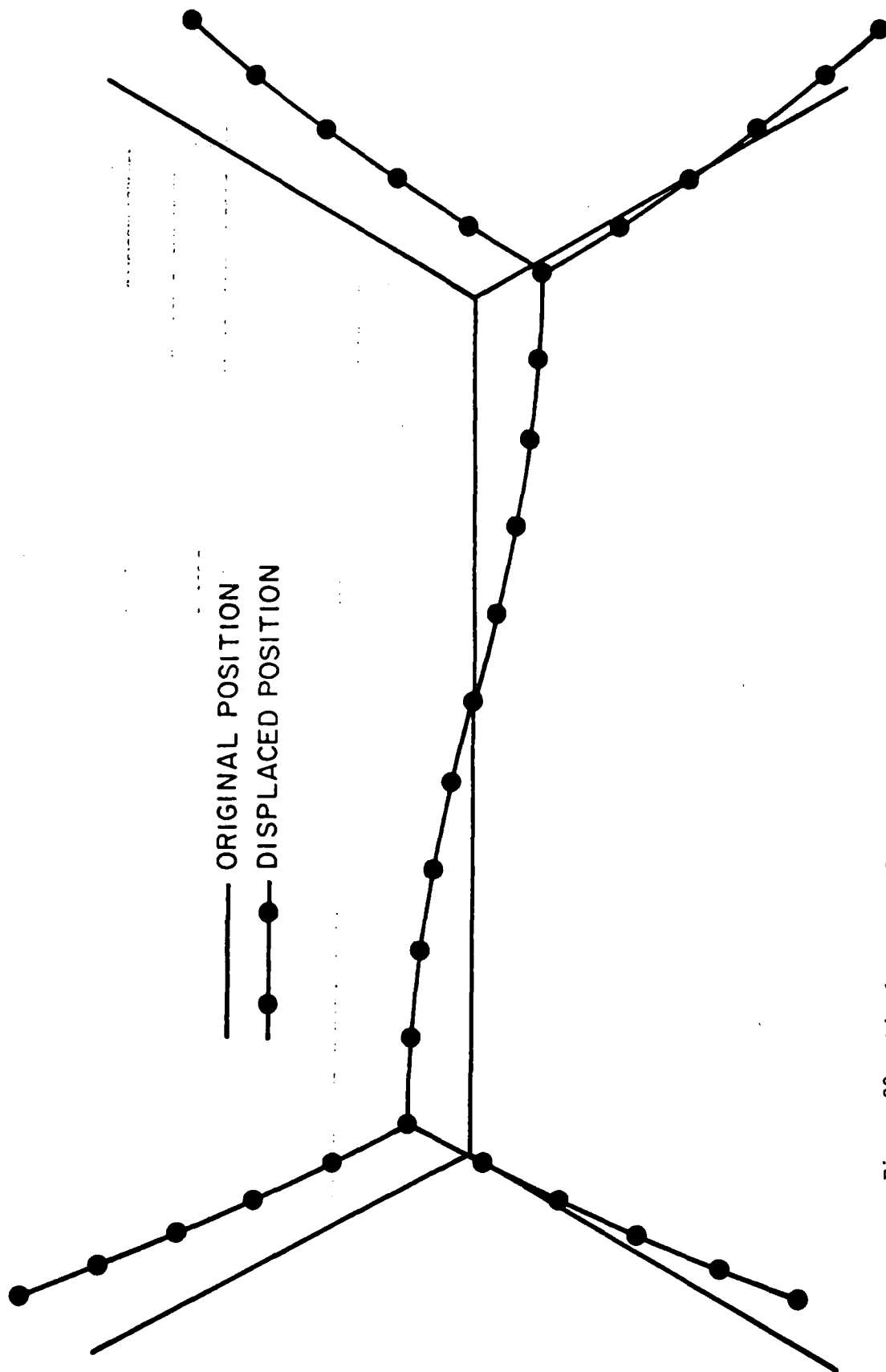


Figure 23. Displacement of the plates of a unit cell at an instant of time during the propagation of a slow Bloch wave in the  $y$  direction ( $w/t = 20$ ,  $v = 0.32$ ).

solution to the dispersion equation, which can be traced continuously as a function of frequency, gives the wavenumber  $k_x$  of propagating waves. However, for propagation along  $y$  it is necessary to trace two solutions to the dispersion relation. The first solution gives the propagating wavenumber  $k_y$  in the first pass-band  $0 < k_s w/2 < 0.0671$ , while the second solution is cutoff there. At  $k_s w/2 = 0.112$ , the second solution switches from cutoff to propagating, i.e.  $k_y$  becomes real, and remains so until  $k_s w/2 = 0.185$ . However, at  $k_s w/2 = 0.178$ , the first solution again becomes real, but corresponds to a solution in a Brillouin zone above the first zone in the  $k_x$ - $k_y$  plane. At  $k_s w/2 = 0.185$ , the two solutions are real and equal. For  $k_s w/2$  above 0.185, the two solutions diverge, one corresponding to the higher Brillouin zone and the other to the first Brillouin zone.

The foregoing dispersion characteristics can best be understood by examining the slowness curves as drawn for a progression of frequencies about  $k_s w/2 = 0.185$ . As  $k_s w/2$  increases from  $k_s w/2 = 0.112$ , the slowness curve starts as a circle, as shown in Figure 24, whose radius increases with frequency. The shape of the circle distorts with increasing frequency until the slowness curve touches the boundary of the first Brillouin zone at  $k_s w/2 = 0.178$ , as shown in Figure 24. Because the slowness curve touches the boundary at intermediate angles, rather than along the  $k_x$  and related six-fold axes, for frequencies above 0.178 it takes the form of closed curves about the vertices of the Brillouin zone and about the points  $k_x = \pi/3$ ,  $k_y = 0$  and six-fold related points. In the range  $0.178 < k_s w/2 < 0.185$ , the closed curves about the vertices shrink to a point, and then expand above 0.185. The closed curves about  $k_x = \pi/3$ ,  $k_y = 0$ , and related points, decrease in size in the

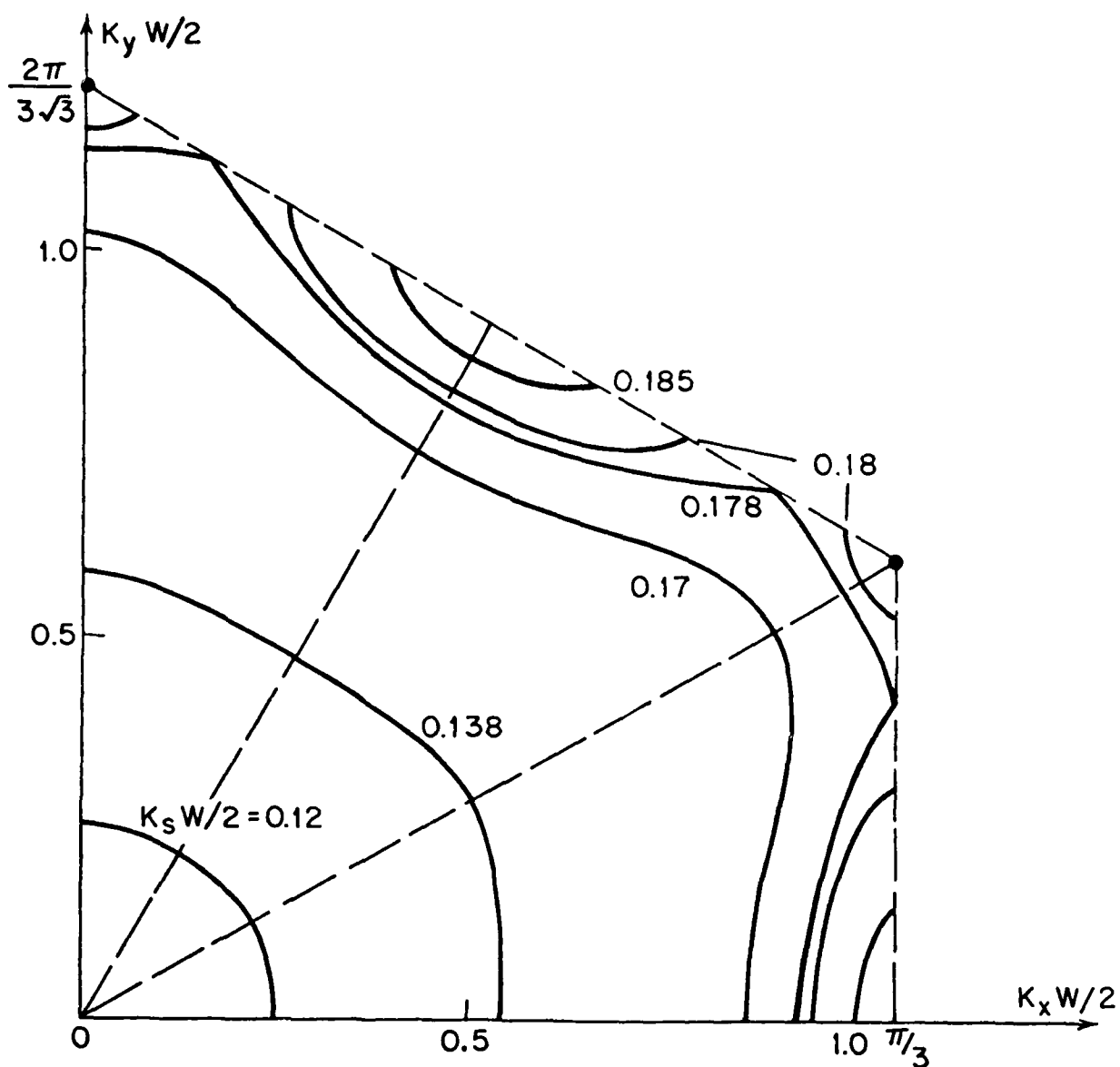


Figure 24. Slowness curves in the first quadrant of the first Brillouin zone for the slow Bloch wave for normalized frequencies in the range  $0.112 < k_s w/2 < 0.185$  ( $w/t = 20$ ,  $v = 0.32$ ).

range  $0.178 < k_s w/2 < 0.188$ . For  $k_s w/2$  between 0.188 and 0.207 no real solution for  $k_x$  exist, as is seen from Figure 20.

The closed curves about the vertices of the Brillouin zone expand in size for  $k_s w/2 > 0.185$ , as seen in Figure 25, until they touch the  $k_x$  and related axes at  $k_s w/2 = 0.207$ . Above 0.207, the slowness curve is again a closed curve about the origin, whose radius decreases with frequency to zero at  $k_s w/2 = 0.0342$ . The foregoing discussion illustrates the complex dependence of the Bloch wave properties on frequency in the higher pass-bands.



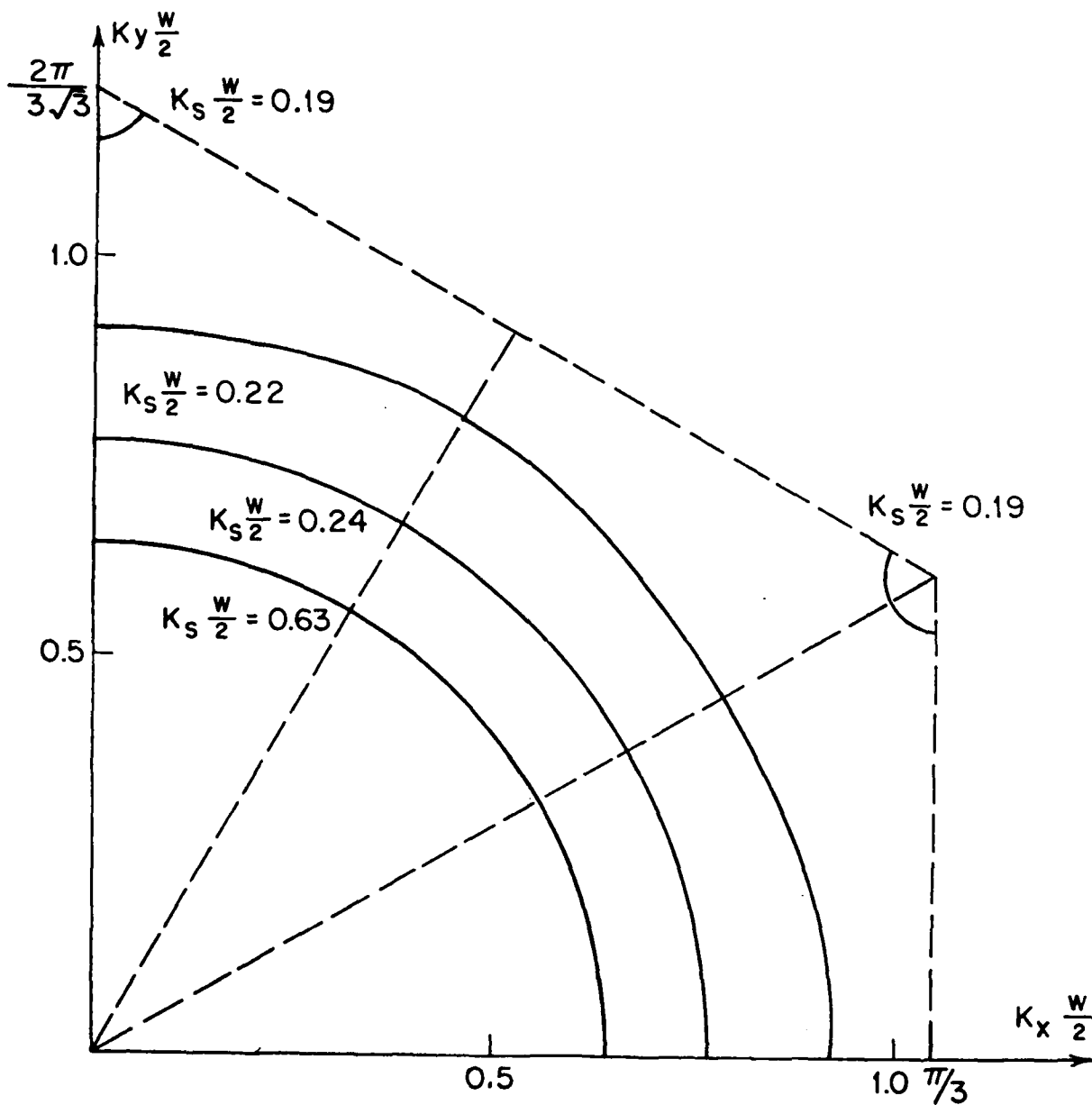


Figure 25. Slowness curves in the first quadrant of the first Brillouin zone for the slow Bloch wave for normalized frequencies in the range  $0.185 < k_s w/2 < 0.341$  ( $w/t = 20$ ,  $\nu = 0.32$ ).

## V. BLOCH WAVE PROPAGATION OBLIQUE TO THE CELL AXES

For propagation oblique to the cell axes, the scattering matrix for the Y joint is  $12 \times 12$  and the matrices  $\underline{a}_i$  and  $\underline{b}_i$  are  $1 \times 4$ , as defined in (38). With this recognition, the matrix algebra needed to find the propagation characteristics of the Bloch wave is the same as that developed in Section IV, provided the matrices defined there are appropriately generalized. Thus, the matrices  $\underline{S}_i$  in (58) that are used to partition  $\underline{S}$  are  $4 \times 4$ , as are the matrices  $\underline{S}_i'$  in (61). The  $\underline{g}$  matrix defined in (60) must be generalized as

$$\underline{g} = \begin{bmatrix} e^{-j\kappa_S w/2} & 0 & 0 & 0 \\ 0 & e^{-j\kappa_L w/2} & 0 & 0 \\ 0 & 0 & e^{-j\kappa_0 w/2} & 0 \\ 0 & 0 & 0 & e^{-j\kappa_1 w/2} \end{bmatrix} \quad (87)$$

where  $\kappa_S$ ,  $\kappa_L$ ,  $\kappa_0$  and  $\kappa_1$  are the modal wave numbers along  $x$ , as defined in (7), (9), (11) and (15).

Because the SH mode is symmetric, it has the same junction property (66) as the L mode so that the  $\underline{T}$  matrix defined in (72) becomes

$$\underline{T} = \begin{bmatrix} 1 & 0 & 0 & 0 \\ 0 & 1 & 0 & 0 \\ 0 & 0 & -1 & 0 \\ 0 & 0 & 0 & -1 \end{bmatrix} \quad (88)$$

Finally, in the  $\underline{\psi}$  matrix of (85) one must use the 4x4 unit matrix for  $\underline{1}$  and recognize that

$$\psi_{1,2} = \exp \left[ -j(\underline{x}_0 k_x + \underline{y}_0 k_y) \cdot \underline{d}_{1,2} \right]. \quad (89)$$

The wave number  $k_z$  is contained in the scattering matrix  $\underline{S}$  and hence in  $\underline{u}'$ , so that the dispersion equation (86) is of the form  $f(\omega, k_x, k_y, k_z) = 0$ . In the rest of this section we report on numerical solutions of the dispersion relation for  $k_x$  vs.  $k_z$  with  $k_y = 0$  and fixed values of  $\omega$ , and for  $k_y$  vs.  $k_z$  with  $k_x = 0$  and fixed values for  $\omega$ . These results, together with those of the previous section, indicate the shape of the slowness surface by means of cuts in the  $(k_x, k_y)$  plane, in the  $(k_x, k_z)$  plane and six-fold related planes, and in the  $(k_y, k_z)$  and six-fold related planes. Calculations were carried out for a honeycomb material having Poisson's ratio  $\nu = 0.32$  and for cell-wall aspect ratio  $w/t = 20$ .

#### A. Low Frequency Propagation: Continuum Model

For normalized frequencies below about  $k_s w/2 = 0.01$ , all of the Bloch waves propagating in the  $(k_x, k_y)$  plane show linear variation of  $k_x$  and  $k_y$  with  $\omega$ , and hence are non-dispersive. We have therefore computed the slowness curves for  $k_s w/2 = 0.01$ , and plotted  $k_z/k_s$  versus  $k_x/k_s$  or  $k_y/k_s$ . The resulting curves are independent of frequency for  $k_s w/2 \leq 0.01$ .

In Figure 26 we have plotted the slowness curves for the two fastest Bloch waves. The same numerical values were obtained for propagation in the  $(x, z)$  plane as for propagation in the  $(y, z)$  plane. The inner curve is a quasi-longitudinal wave (Q-P), as noted from

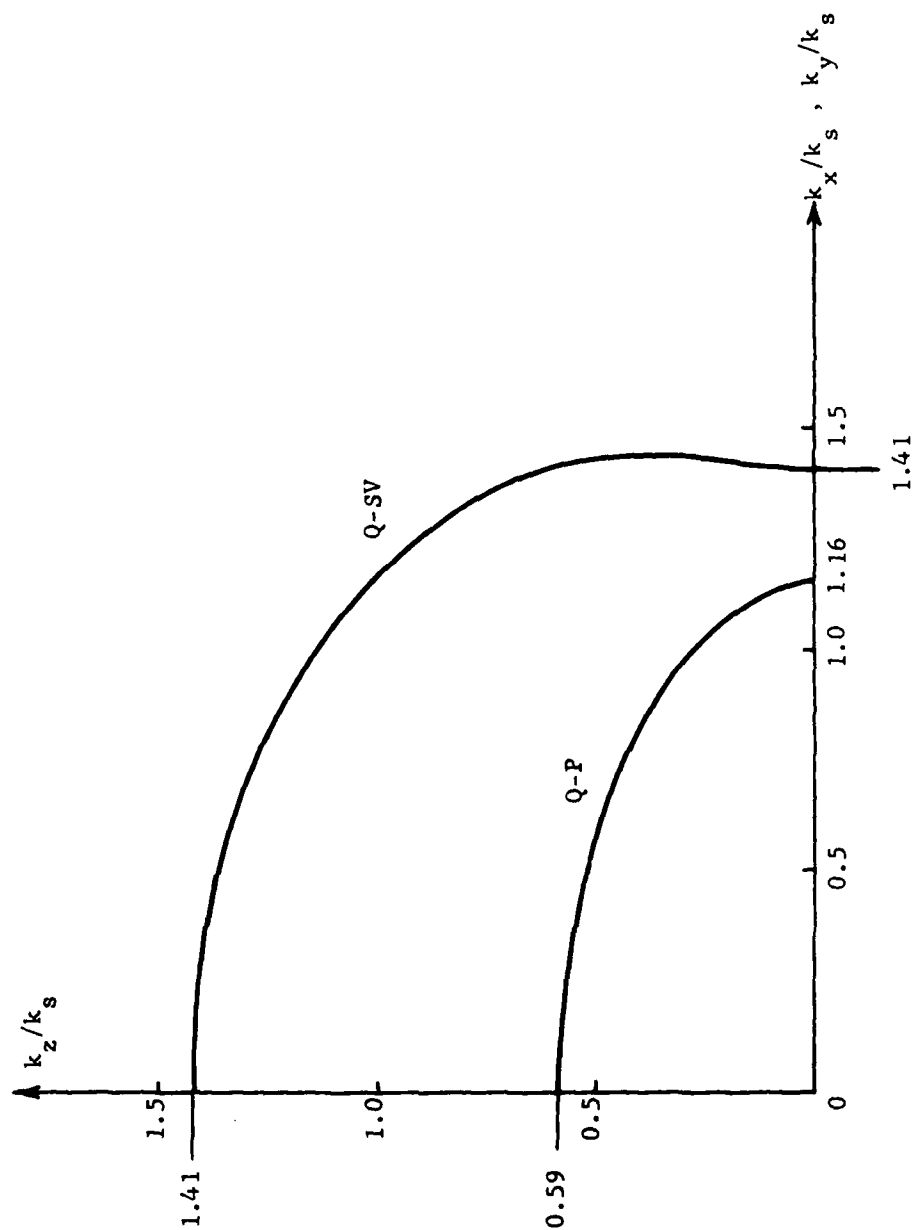


Figure 26. Slowness curves in the  $(k_x, k_z)$  and  $(k_y, k_z)$  planes for the Q-P and Q-SV Bloch waves at low frequency ( $k_s w/2 = 0.01$ ) for a honeycomb with  $w/t = 20$ ,  $\nu = 0.32$ .

the particle displacement for propagation along  $x$  and  $y$ . Also, for propagation along  $z$ , the value  $k_z/k_s = 0.59$  is the same as for the wavenumber  $k_L$  of the symmetric Lamb mode in the cell walls, which is essentially an extensional or longitudinal wave at low frequencies. Based on the polarization properties for propagation in the  $(x, y)$  plane, the outer curve in Figure 26 represents a vertically polarized shear wave (Q-SV). The fact that the intersection of the curve with the  $k_x/k_s$  or  $k_y/k_s$  axis and with the  $k_z/k_s$  axis have the same values (41) indicates that the honeycomb acts as an elastic continuum<sup>(11)</sup>.

Because the slow Bloch wave travels at one tenth the velocity of the fast Bloch waves in the  $(x, y)$  plane, its slowness curve cannot be drawn with equal scales for  $k_x$  and  $k_z$ , as in Figure 26. For this reason we have drawn the dispersion curves with different scales in Figure 27. The slow Bloch wave is labeled Q-SH because its particle motion is similar to horizontally polarized shear wave for propagation along  $x$  or  $y$ . The discrepancy between the slowness curves for propagation in the  $(x, z)$  planes and  $(y, z)$  plane amounts to 2.5% and is thought to result from the approximations used to compute the curves. It is seen that both shear waves cross the  $k_z$  axis at the same point, in accordance with the properties of a hexagonal contin-

to examine further the correspondence between the slow-  
 Figures 26 and 27 and an elastic continuum of hexa-  
 we have used the propagation characteristics along  
 to define the stiffness constants of the continuum.  
 the slowness curves for continuum were com-

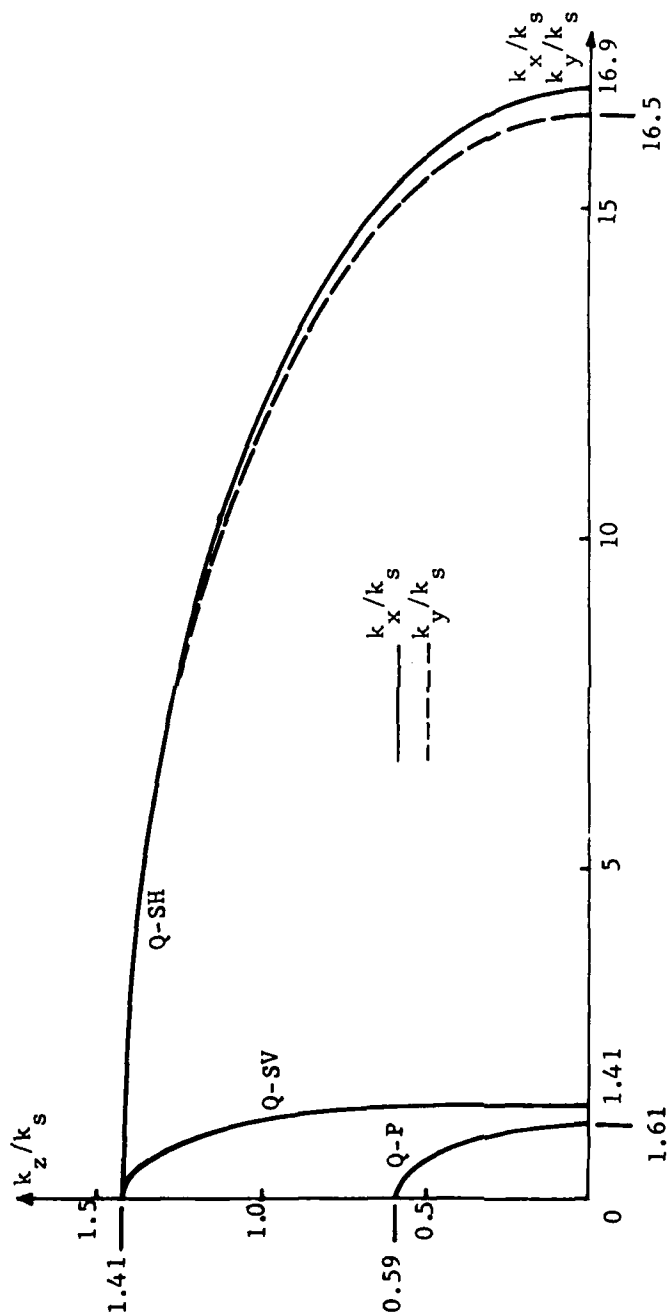


Figure 27. Slowness curves in the  $(k_x, k_z)$  and  $(k_y, k_z)$  planes for all three Bloch waves at low frequency ( $k_g w / \lambda = 0.01$ ) for a honeycomb with  $w/t = 20$ ,  $\nu = 0.32$ . Note the difference in vertical and horizontal scales need to accommodate the Q-SH Bloch wave.

puted and compared with those of Figures 26 and 27.

Static measurements of the mass density  $\rho_H$  and stiffness constant  $C_{33}$  for a WRII kraftboard honeycomb<sup>(12)</sup>, as listed in Table III, were used in conjunction with the properties listed in Reference (11) to find the remaining stiffness constants, which are listed in Table III. The mass density  $\rho$  of the kraftboard listed in Table III was obtained by dividing  $\rho_H$  by the fraction of honeycomb's volume occupied by the phenolic material. Assuming the kraftboard act as an isotropic medium with  $\nu = 0.32$ , and recognizing that  $k_z$  for the Q-P wave propagating along  $z$  is equal to  $k_L$ ,  $\mu$  can be found from the relation

$$\omega \sqrt{\frac{\rho_H}{C_{33}}} = k_L = \omega \sqrt{\frac{\rho}{\mu}} \sqrt{\frac{1-\nu}{2}}.$$

Knowing  $\mu$  and  $\nu$ , one can find  $\lambda$  from the expression

$$\nu = \frac{\lambda}{2(\lambda + \mu)}$$

for Poisson's ratio. These values are also listed in Table III.

The average of the values of  $k_x/k_s$  was used in obtaining  $C_{66}$  in Table III. With the values listed in Table III, we have computed the slowness curves for a hexagonal continuum and compared them with Figures 26 and 27. The Q-P and Q-SV curves were indistinguishable, while the Q-SH curve fell between the  $k_z$  vs.  $k_x$  and  $k_z$  vs.  $k_y$  curves of Figure 27. We therefore conclude that the continuum model is an accurate representation for the honeycomb at low frequencies. It should be noted that for a WRII kraftboard honeycomb, the normalized frequency  $k_g w/2 = 0.01$  corresponds to an actual frequency

TABLE III  
MATERIAL CONSTANTS FOR A WRH KRAFTBOARD HONEYCOMB

<u>Kraftboard</u>	<u>Honeycomb</u>
$\rho = 0.899 \text{ gm/cm}^3$	$\rho_H = 0.061 \text{ gm/cm}^3$
$\nu = 0.32$	$C_{33} = 3.79 \times 10^9 \text{ dynes/cm}^2$
$\mu = 3.38 \times 10^{10} \text{ dyne/cm}^2$	$C_{11} = 9.75 \times 10^8$
$\lambda = 1.9 \times 10^{10}$	$C_{12} = 9.66 \times 10^8$
	$C_{13} = 5.94 \times 10^8$
	$C_{44} = 6.60 \times 10^8$
	$C_{66} = 4.60 \times 10^6$



$f = 30$  Hz. For higher frequencies, the Q-SH wave becomes dispersive, while the Q-P and Q-SV waves do not exhibit dispersive effects until a frequency of nearly 10 KHz.

#### B. Dispersive Effects for the Slow Bloch Wave

To illustrate the dispersive effects on the slow Bloch wave we have computed slowness curves for  $k_s w/2 = 0.03, 0.06, 0.13$  and  $0.26$ . The results for  $k_s w/2 = 0.03$  are plotted in Figure 28. The extent of the curves along  $k_x$  and  $k_y$  is markedly different. In the insert of Figure 28 we have sketched a perspective view of the slowness surface in the first Brillouin zone. The surface is seen to have the shape of a six-pointed star. Slowness surfaces in the neighboring Brillouin zones have the same shape, and oriented such that the points of the stars face those of the star in the first zone.

As the frequency increases from 0.03, the tips of the stars in neighboring Brillouin zones grow towards each other until they touch at 0.316 and form tunnels for frequencies above 0.316. The tunnel shape is indicated in Figure 29, which is drawn for  $k_s w/2 = 0.06$ . As the frequency increases further, the tunnels increase in width until they merge at 0.071 when the wave becomes cut-off along  $y$ , as indicated in Figure 21. For frequencies between 0.071 and 0.112, where the second pass band starts, the slowness surface in  $(k_x, k_y, k_z)$  space undulates but does not touch down to the  $(k_x, k_y)$  plane.

The slowness surfaces of the slow Bloch wave in the second pass band consist of two surfaces. The outer surface does not touch the  $(k_x, k_y)$ , while the inner surface in the first Brillouin zone is closed about the origin. Identical closed surfaces exist in each of the

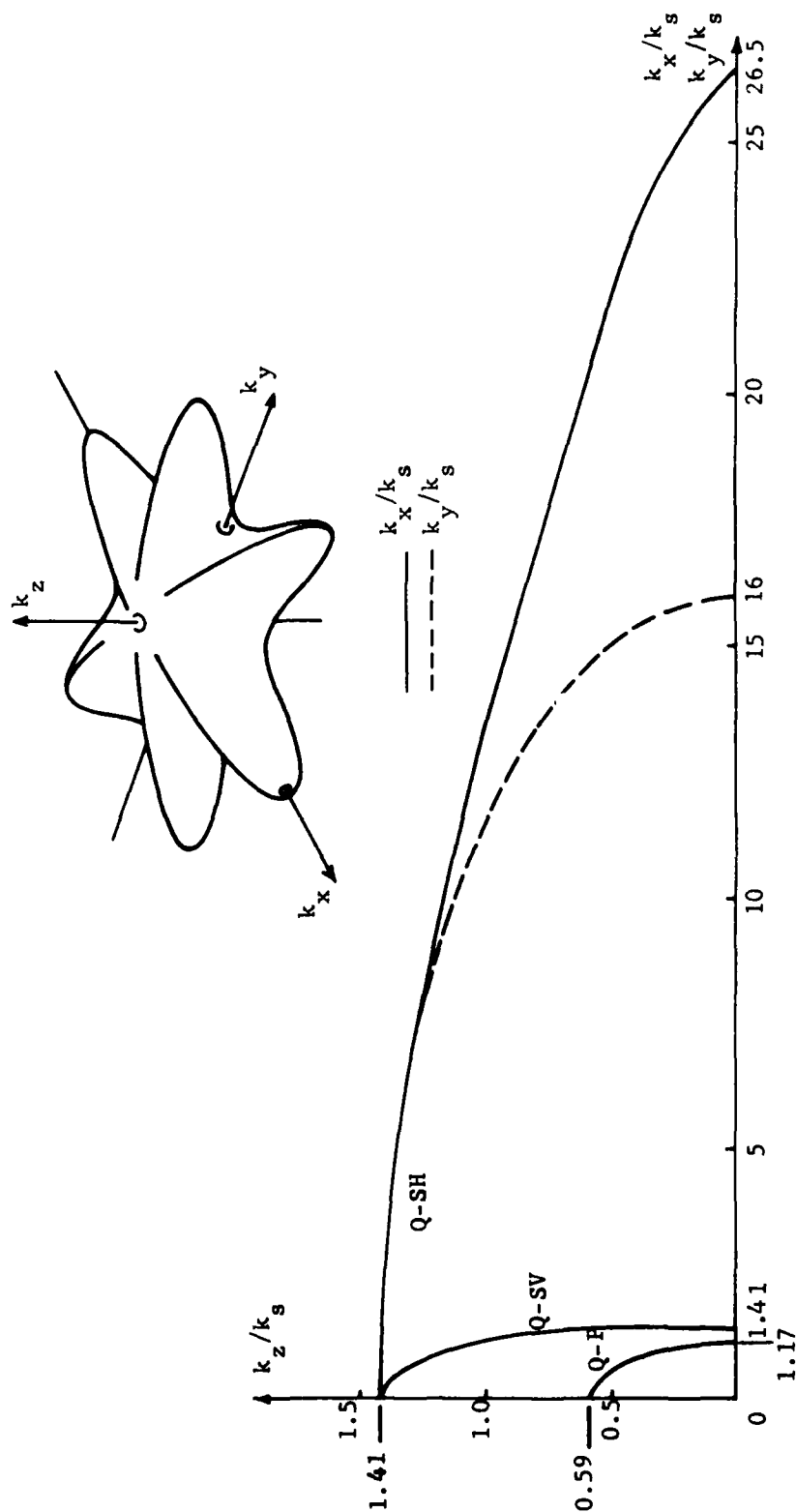


Figure 28. Slowness curves in the  $(k_x, k_z)$  and  $(k_y, k_z)$  planes for frequency  $k_g w/2 = 0.03$  approaching the first stop-band for propagation along  $x$  of the Q-SH Bloch wave ( $w/t = 20$ ,  $\nu = 0.032$ ).

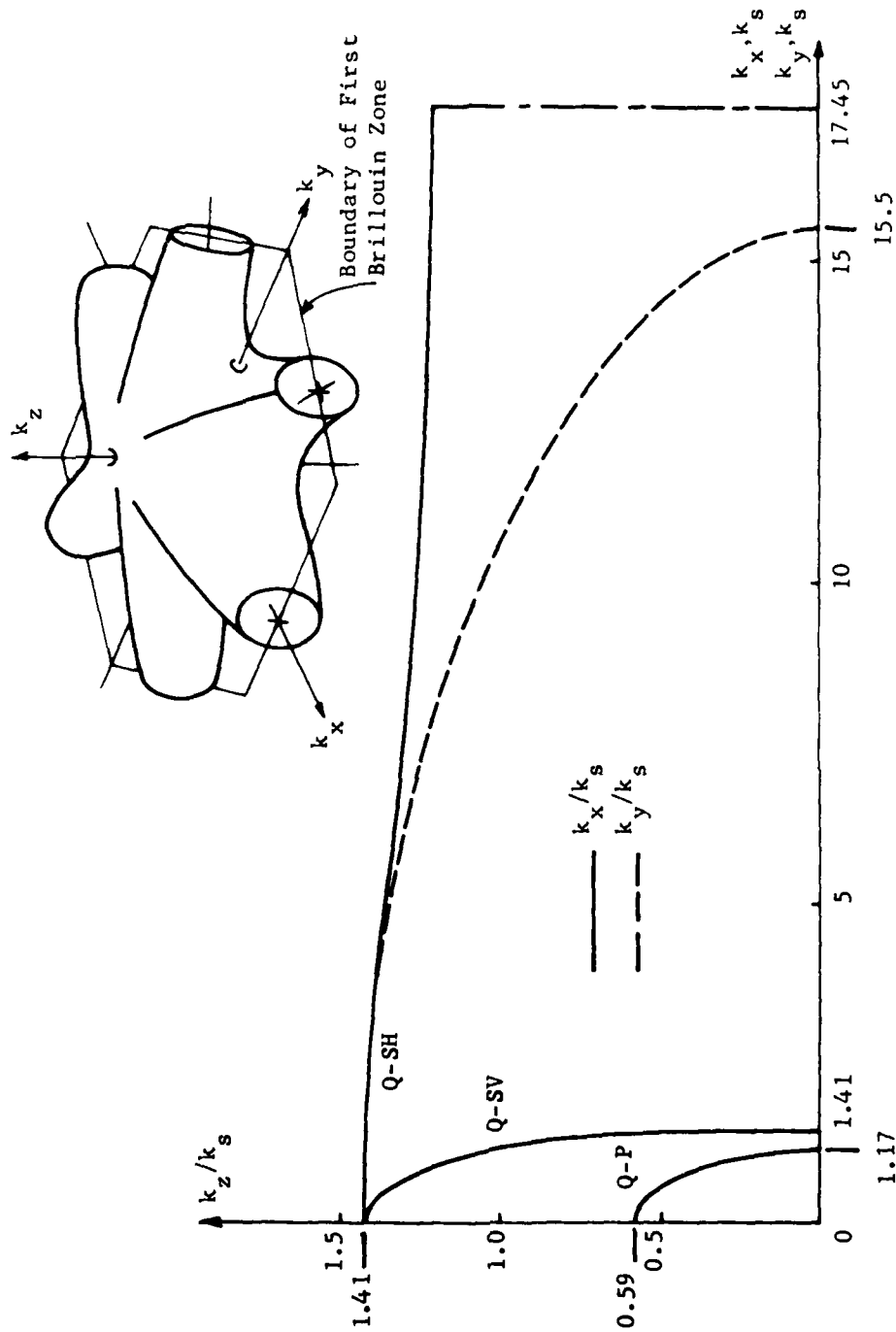


Figure 29. Slowness curves in the  $(k_x, k_z)$  and  $(k_y, k_z)$  planes for frequency  $k_g w/2 = 0.06$  located in the first stop-band for propagation along  $x$  of the Q-SH Bloch wave ( $w/t = 20$ ,  $\nu = 0.32$ ).

Brillouin zones. The intersections of these surfaces with the  $(k_x, k_z)$  and  $(k_y, k_z)$  planes are shown in Figures 30 and 31 for  $k_g w/2 = 0.13$ . The outer and inner surfaces touch in the  $(k_y, k_z)$  plane and six-fold related planes. The touching points are like the points of conical refraction in the optical slowness surfaces of a biaxial crystal. The surfaces for  $k_z > 0$  may be thought of as a head (inner surface) with a hat (outer surface) that rests on the head at six points.

As an example of the slowness curves in the third pass band of the SH-Bloch wave, we have drawn Figures 32 and 33 for  $k_g w/2 = 0.26$ . Slowness curves for propagation in the  $(x, z)$  and six-fold related planes are indicated in Figure 32, while Figure 33 has been drawn for propagation in the  $(y, z)$  and six-fold related planes. The Q-SH slowness surface is seen to consist of two parts. The upper part represents an undulating surface that does not touch the  $(k_x, k_y)$  plane. The lower Q-SH slowness surface resembles a tube enclosing the boundary of the Brillouin zone. The character of the slowness curves for the fast Bloch waves is discussed in the next section.

### C. Dispersive Effects for the Fast Bloch Wave

As seen from Figures 9 and 10, the Q-SV Bloch wave propagating in the  $(x, y)$  plane does not have significant dispersion for  $k_g w/2 < 0.4$ . The Q-P Bloch wave propagating in the  $(x, y)$  plane however shows significant dispersion even at  $k_g w/2 = 0.2$ . For oblique propagation the dispersive effects should be evident in both waves, even at frequencies as low as  $k_g w/2 = 0.2$ , since both waves are composed of the same plate modes in the honeycomb walls.

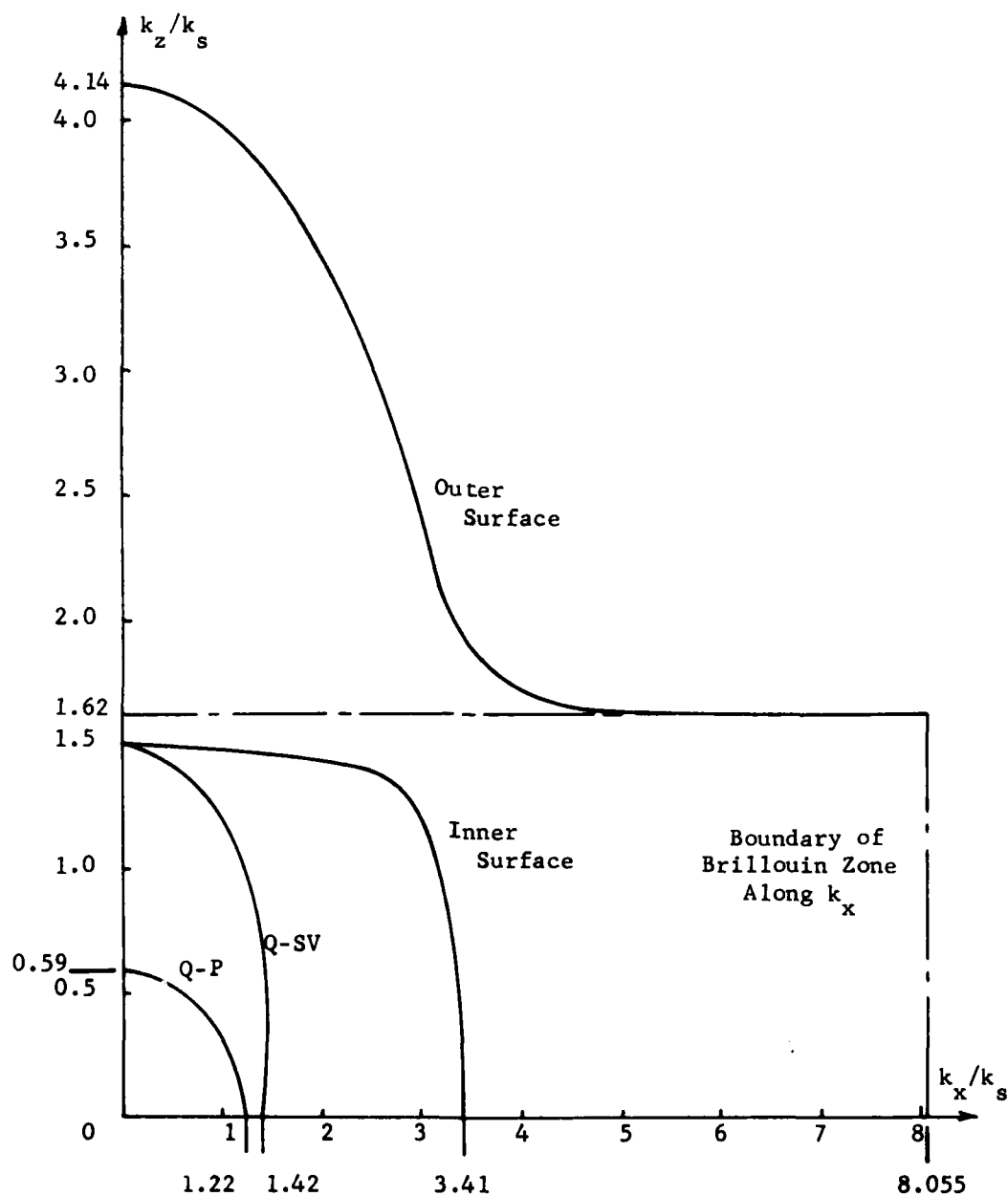


Figure 30. Slowness curves in the  $(k_x, k_z)$  plane for frequency  $k_s w/2 = 0.13$  in the second pass-band of the Q-SH Bloch wave showing the presence of a fourth surface ( $w/t = 20$ ,  $\nu = 0.32$ ).

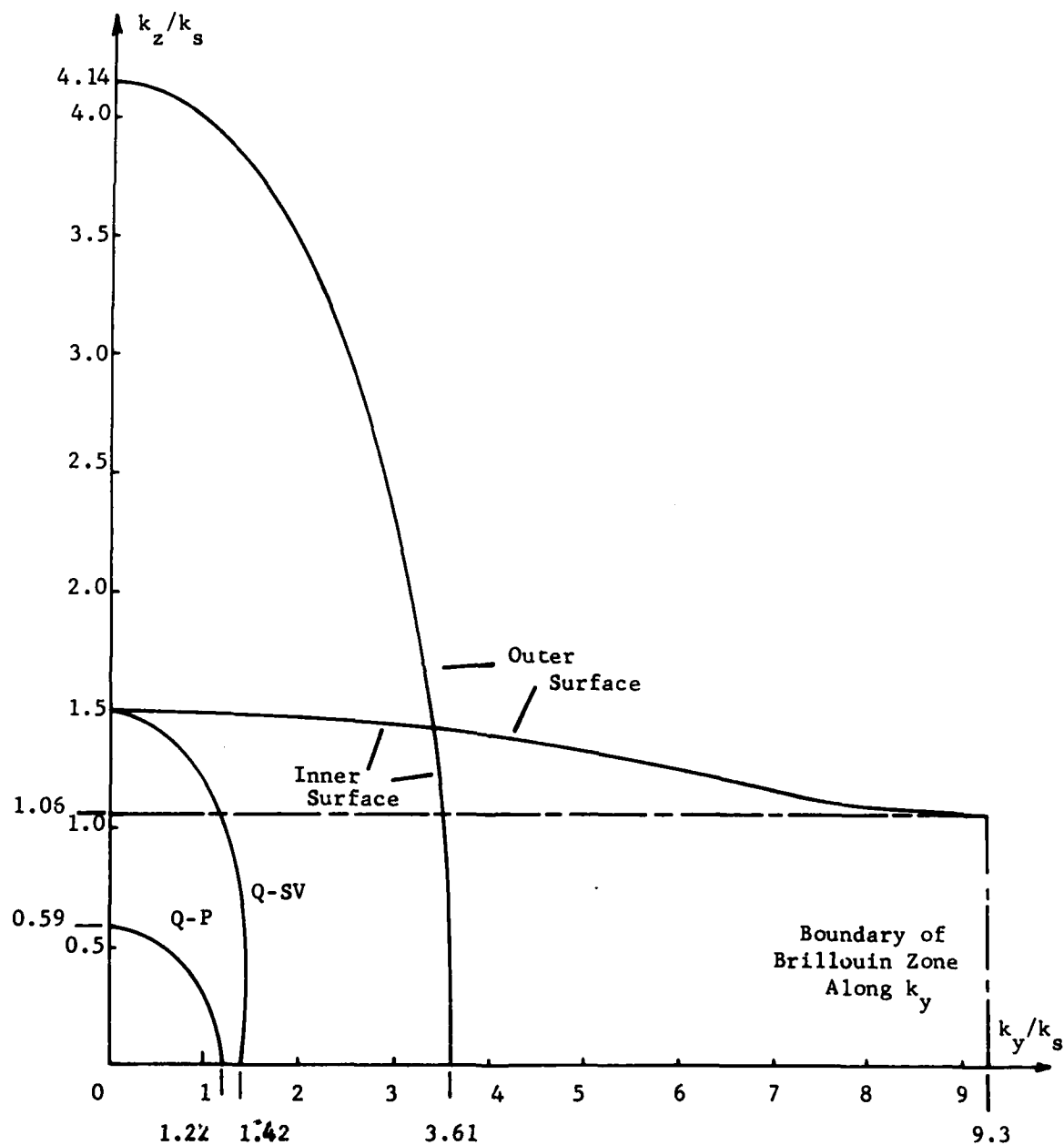


Figure 31. Slowness curves in the  $(k_y, k_z)$  plane for frequency  $k_s w/2 = 0.13$  in the second pass-band of the Q-SH Bloch wave showing the presence of a fourth surface ( $w/t = 20$ ,  $\nu = 0.32$ ). This figure is for the same frequency as Figure 30.

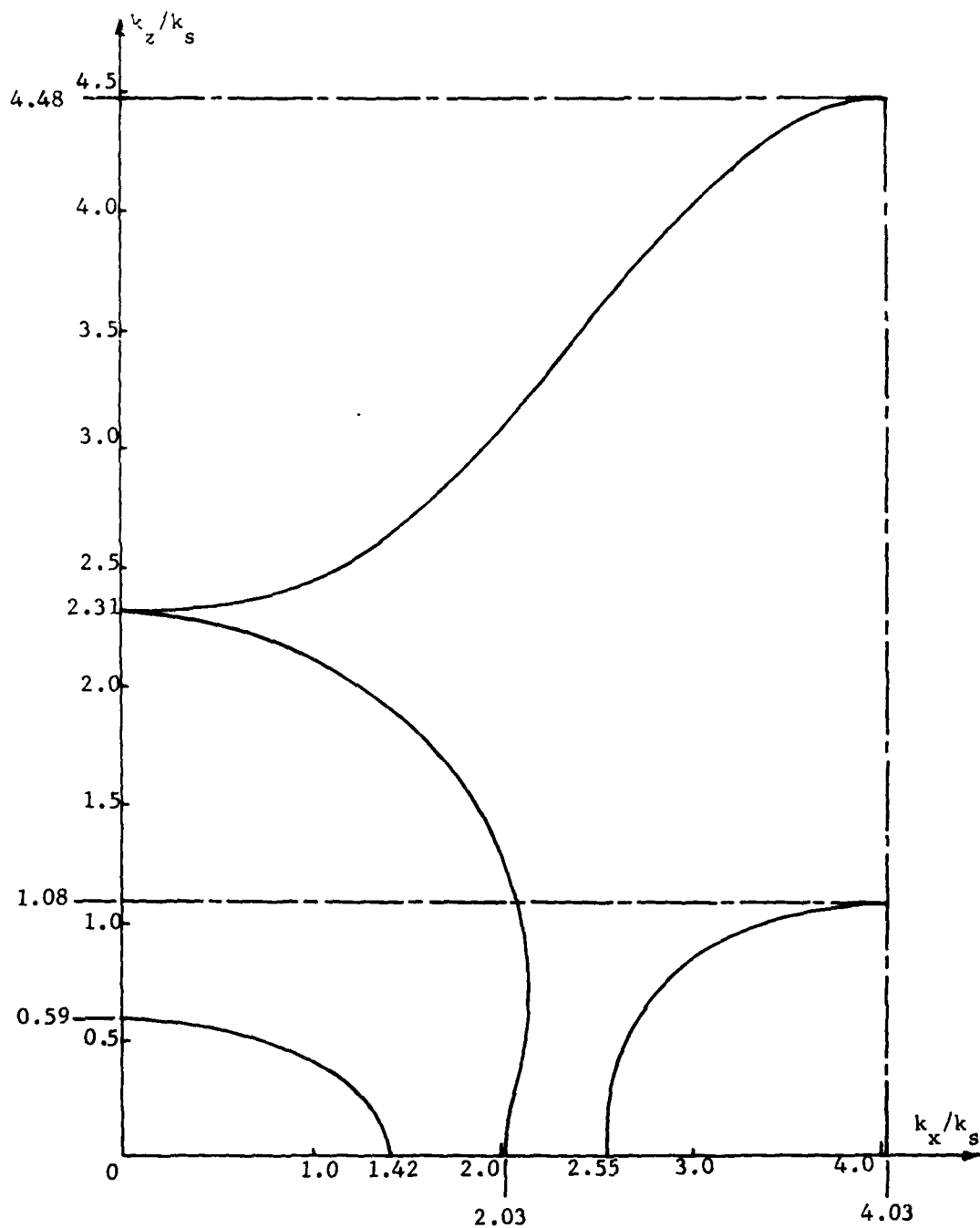


Figure 32. Slowness curves in the  $(k_x, k_z)$  plane for frequency  $k_s w/2 = 0.26$  in the third pass-band of the Q-SH Bloch wave ( $w/t = 20$ ,  $\nu = 0.32$ ).

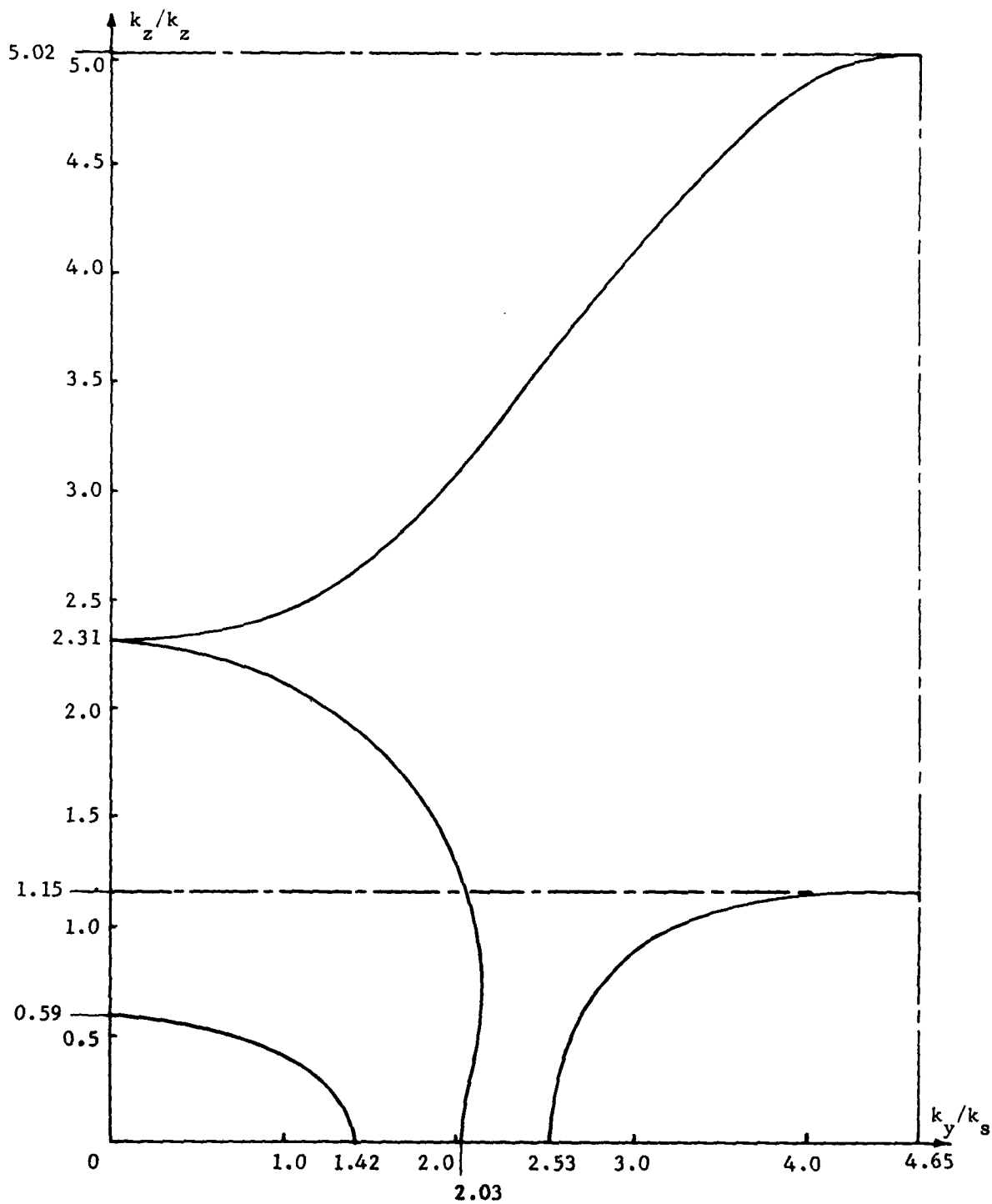


Figure 33. Slowness curves in the  $(k_y, k_z)$  plane for frequency  $k_s w/2 = 0.26$  in the third pass-band of the Q-SH Bloch wave ( $w/t = 20$ ,  $\nu = 0.32$ ). This figure is for the same frequency as Figure 32.



The nature of the dispersive effect can be understood by examining propagation for frequencies in the vicinity of  $k_s w/2 = 0.216$ , where the wavenumbers of the Q-P and Q-SV Bloch waves propagating in the (x, y) plane are equal. The slowness curves of the Q-P and Q-SV Bloch waves are drawn in Figure 34 for  $k_s w/2 = 0.21$ . Because anisotropy effects are not significant at this frequency, the same curve holds for propagation in the (x, z) plane and for propagation in the (y, z) planes. Comparing Figure 34 with Figure 26, which is drawn for  $k_s w/2 = 0.01$ , it is seen that the Q-P wave shows dispersive effects for propagation in the (x, y) plane. However, for propagation along z, the Q-P wave shows no dispersion since its wavenumber is that of the symmetric Lamb wave in the cell wall. For this direction of propagation it is the Q-SV wave that exhibits dispersive effects.

At the frequency  $k_s w/2 = 0.23$ , the slowness curves shown in Figure 35 reflect the fact the wavenumber of the Q-P wave propagating in the (x, y) plane is greater than that of the Q-SV wave. However, for propagation along z, the relative size of the wavenumbers is reversed. Thus, along the inner branch of the slowness curve in Figure 35 the Bloch wave polarization switches from that of a shear wave propagating in the (x, y) plane with particle motion along z to that of a longitudinal wave propagating along z. Alternatively, the outer branch has the polarization of a longitudinal wave for propagation in the (x, y) plane, since then the SH plate modes are not part of the Bloch wave. However, for propagation along z, the outer branch has shear polarization.

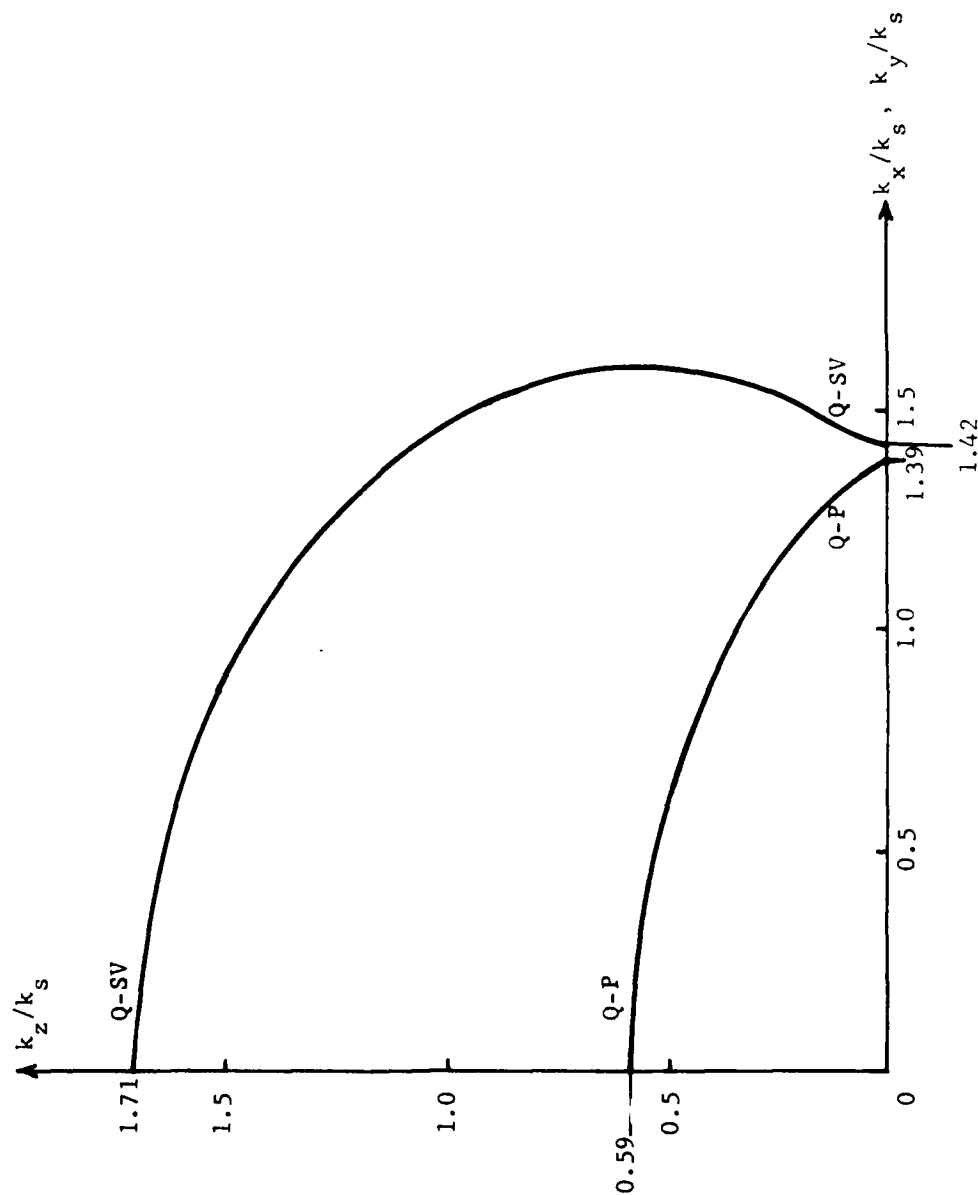


Figure 34. Slowness curves in the  $(k_x, k_z)$  and  $(k_y, k_z)$  plane of the Q-P and Q-SV Bloch waves for frequency  $k_s w/2 = 0.21$  just below the point where the two waves have the same phase velocity in the  $(x, y)$  plane.

AD-A086 667

POLYTECHNIC INST OF NEW YORK BROOKLYN

F/8 13/13

WAVE PROPAGATION IN HONEYCOMB AND FOAM-CORE PANELS FOR APPLICAT--ETC(III)

APR 80 H L BERTONI, S K PARK

F1962A-77-C-0130

UNCLASSIFIED

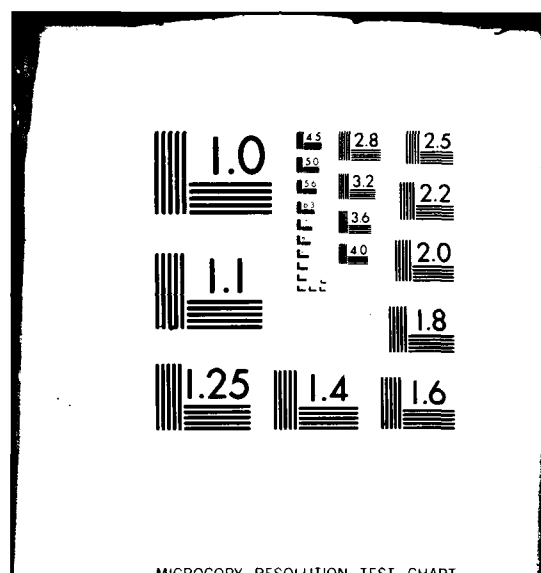
RADC-TR-80-112

ML

2 of 2

AD-A086 667

END  
DATE  
FILMED  
8-80  
DTIC



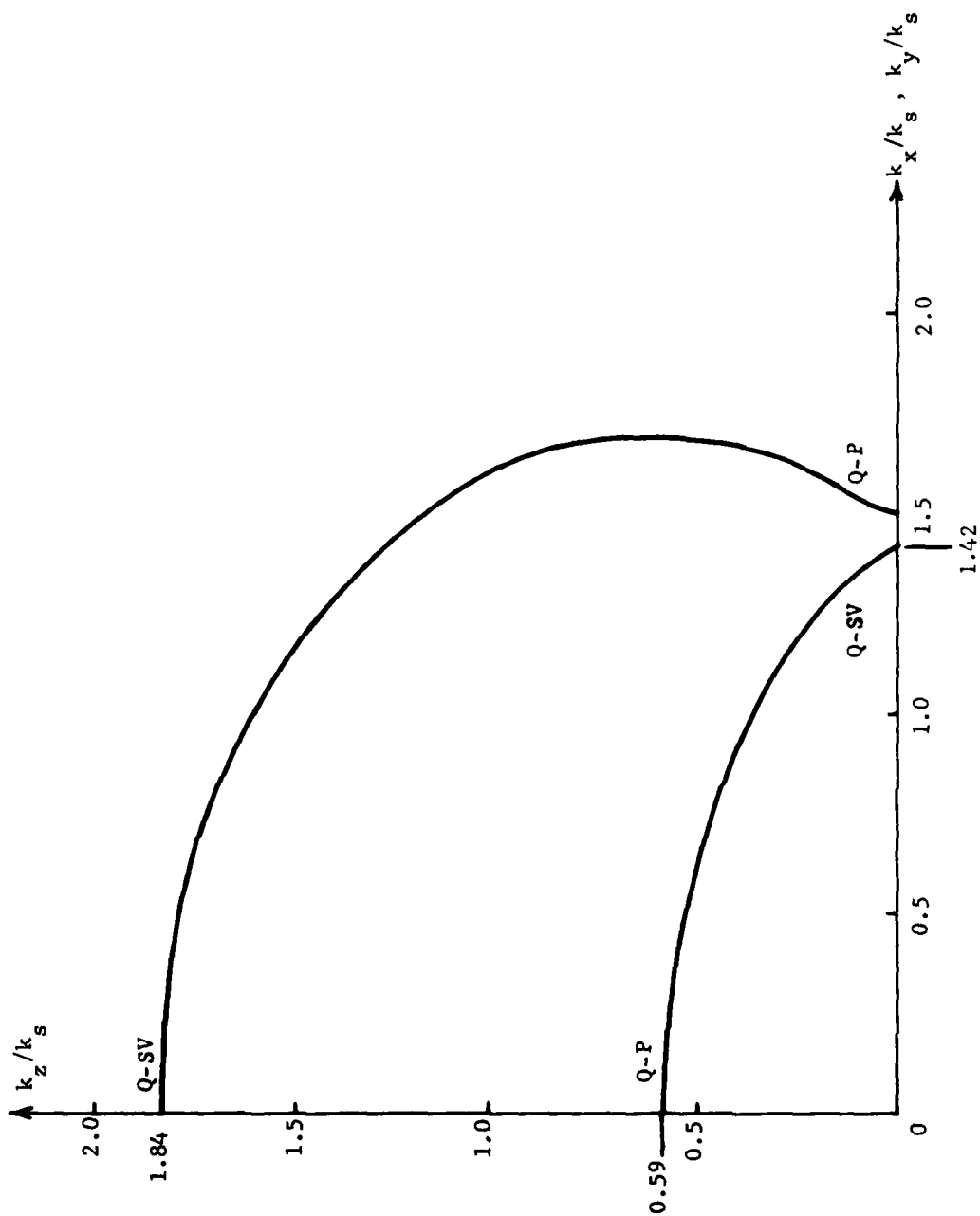


Figure 35. Slowness curves in the  $(k_x, k_y)$  and  $(k_x, k_z)$  plane of the Q-P and Q-SV Bloch waves for frequency  $k_y^2/k_s^2 = 0.23$  just above the point where the two waves have the same phase velocity in the  $(x, y)$  plane. Note the change in polarization indicated as the direction of propagation changes from being along  $z$  to being perpendicular to  $z$ .

Thus, in the first pass band of the fast Bloch waves, a significant aspect of the dispersion is to cause the polarization type of the wave to change with direction of propagation. As a result, the Bloch waves cannot be labeled as a quasi-shear or quasi-longitudinal for frequencies above  $k_s w/2 = 0.216$ . This conclusion is further supported by the slowness curves for the fast Bloch waves at the frequency  $k_s w/2 = 0.26$ , which are shown in Figures 32 and 33. From Figures 30 and 31 it is seen that the dispersion of the fast Bloch waves first becomes significant at  $k_s w/2 = 0.13$  for shear wave propagation along  $z$ .

Because the fast Bloch waves do not show significant dispersion for normalized frequencies below  $k_s w/2 = 0.13$ , their propagation can be modeled by that of Q-P and Q-SV plane waves in a hexagonal continuum for  $k_s w/2 < 0.13$ . However, the continuum model can be used for Q-SH wave propagation only in the range  $k_s w/2 < 0.013$ . Thus, in dealing with bounded honeycombs, the continuum model can be used for  $k_s w/2 < 0.013$  unless Q-SH waves are not excited, in which case the continuum model can be used up to  $k_s w/2 = 0.13$ . This distinction is used in the next section.

## VI. WAVES GUIDED BY A FACE PLATE BONDED TO A HONEYCOMB

A complete treatment of wave propagation in honeycomb panels requires taking into account both of the face plates and the finite honeycomb thickness. The properties of these waves result from a combination of effects due to coupling between the face plates and the honeycomb, and to the thickness of the honeycomb. However, for the NDE task of finding areas of debonding, one is only interested in coupling between the face plate and honeycomb. This coupling can be studied in isolation by examining the loading that a semi-infinite honeycomb places on the modes of the face plate.

In this section we consider the properties of the lowest modes guided by an aluminum face plate that is bonded to a semi-infinite honeycomb, as shown in Figure 36. The honeycomb is assumed to act as a hexagonal continuum having the parameters listed in Table III for a Shelter Core honeycomb. The face plate is assumed to have thickness  $h = 1/16$  in. and to be bonded to the honeycomb by means of an adhesive layer of vanishing thickness. However, in practical cases the adhesive layer can have major influence on the guided wave, as is shown in the next section for foam-core panels.

The SH mode in the aluminum plate couples to the slow Q-SH Bloch wave in the honeycomb. However, both the symmetric Lamb mode and the flexural mode in the aluminum plate couple to the fast Bloch waves. Thus we may treat the SH modes separately from the Lamb and flexural modes.

The Q-SH Bloch wave is non-dispersive for  $k_g w/2$  less than about 0.013, using the dimensions assumed for the Shelter Core honeycomb

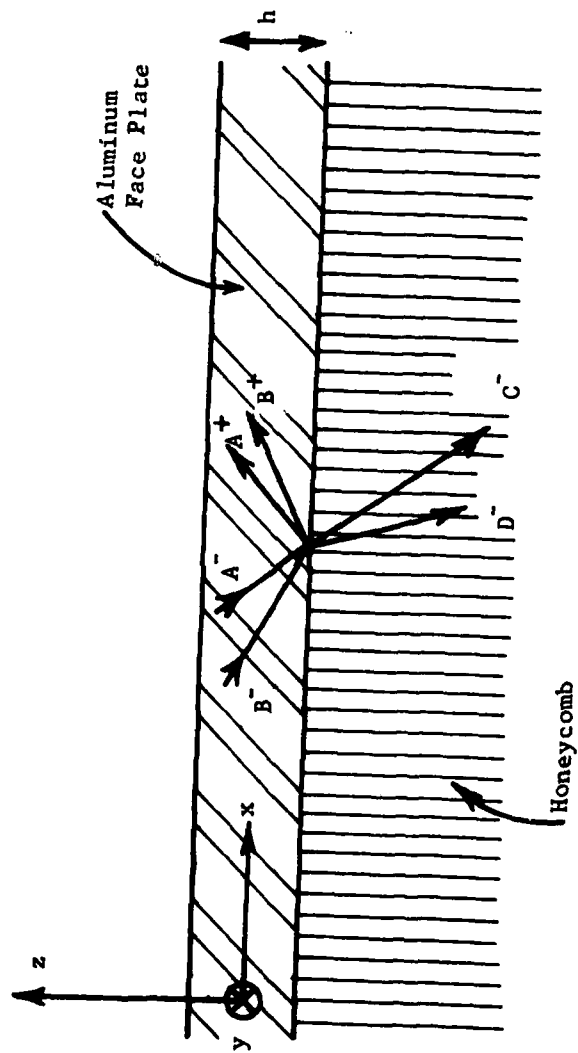


Figure 36. Coordinate system used in computing the characteristics of waves guided by an aluminum face plate bonded to a semi-infinite honeycomb.



gives an upper frequency limit of about 1,000 Hz. Thus our study for guided SH waves in the aluminum plate is limited to frequencies less than 1,000 Hz. On the other hand, the fast Bloch waves are non-dispersive for  $k_s w/2 < 0.13$  or  $f < 10$  kHz, so that the continuum model for the fast Bloch waves may be used up to this frequency. Hence, our study of the symmetric Lamb and flexural modes of the aluminum plate apply up to 10 kHz.

#### A. SH Mode of the Aluminum Plate

The fields associated with the SH mode in the aluminum plate can be represented as a combination of the SH plane waves in aluminum propagating with wave vectors  $(k_x \pm k'_{zs})$  where

$$k'_{zs} = \sqrt{(k_s^1)^2 - k_x^2} \quad (90)$$

and  $k_s^1$  is the shear wavenumber of aluminum. The wavenumber  $k_x$  along  $x$  must be the same for both plane waves, and for the Q-SH Bloch wave in the honeycomb in order to satisfy the boundary conditions at the free surface and at the plate-honeycomb boundary. The field quantities entering into the boundary conditions at  $z = \pm h/2$  are  $v_z$  and  $T_{yz}$ . If  $A^+$  and  $A^-$  are the amplitudes of these two waves, then the field quantities in the plate are given by (3)

$$v_y(x, z) = (A^+ e^{-jk'_{zs} z} + A^- e^{jk'_{zs} z}) e^{-jk_x x} \quad (91)$$

and

$$T_{yz}(x, z) = \frac{\mu^1 k_s^1}{\omega} (-A^+ e^{-jk'_{zs} z} + A^- e^{jk'_{zs} z}) e^{-jk_x x} \quad (92)$$

where  $\mu^1$  is the shear modulus of aluminum.

If  $D^-$  represents the amplitude of the Q-SH wave in the honeycomb, then the field quantities for  $z < -h/2$  are <sup>(13)</sup>

$$v_y(x, z) = D^- e^{jk_z z} e^{-jk_x x} \quad (93)$$

and

$$T_{yz}(x, z) = \frac{C_{44} k_z}{\omega} D^- e^{jk_z z} e^{-jk_x x} \quad (94)$$

Here  $C_{44}$  is the stiffness constant listed in Table III and  $k_z$  is the wavenumber along  $z$  of the Q-SH wave. Using the continuum model for the honeycomb,  $k_z$  can be found from the dispersion equation

$$C_{66} k_x^2 + C_{44} k_z^2 - \rho_H \omega^2 = 0 \quad (95)$$

where  $\rho_H$  and  $C_{66}$  are taken from Table III.

The boundary condition at the free surface  $z = h/2$  is  $T_{yz}(x, h/2) = 0$ , while at the interface  $z = -h/2$  we have that  $v_y(x, z)$  and  $T_{yz}(x, z)$  are continuous. After some manipulation, these conditions can be written in the form

$$\begin{bmatrix} -e^{-jk_z^i h} & 1 & 0 \\ e^{jk_z^i h} & 1 & -e^{-jk_z h/2} e^{jk_z^i h/2} \\ -e^{-jk_z^i h} & 1 & -\frac{C_{66} k_z}{\mu k_{zs}^i} e^{-jk_z h/2} e^{jk_z^i h/2} \end{bmatrix} \begin{bmatrix} A^+ \\ A^- \\ D \end{bmatrix} = 0 \quad (96)$$

The dispersion equation for the wave is obtained by setting the determinant of the  $3 \times 3$  matrix equal to zero. Recognizing that  $k_z$  and  $k_{zs}^i$  are functions of  $k_x$ , the dispersion equation takes the form  $f(k_x, \omega) = 0$ .

Because the Q-SH Bloch wave is extremely slow, for  $k_x$  in the vicinity of  $k_g'$ , this Bloch wave will be propagating along  $z$ . As a result, the SH mode in the aluminum plate will be converted into a leaky surface wave that radiates its energy into the honeycomb. The continuous radiation of energy causes an exponential decrease in the amplitude of the surface wave with distance in the propagation direction. The exponential decrease exhibits itself as an imaginary part in the wavenumber  $k_x$  of the surface wave. Thus the root of the dispersion equation  $f(k_x, \omega) = 0$  is the complex number  $k_x = \beta - j\alpha$ , where  $\beta$  is the phase constant and  $\alpha$  the attenuation constant of the leaky surface wave.

Numerical solutions of the dispersion equation for  $\beta$  and  $\alpha$  are plotted in Figure 37. The leaky wave is somewhat slower than the SH wave in an isolated aluminum plate. Because  $\alpha$  and  $\beta$  are on the same order, the wave is heavily attenuated even in propagating one wavelength. Thus, the coupling to the honeycomb strongly affects the wave in the aluminum plate. In principle, the significant perturbation resulting when the plate is bonded to the honeycomb makes possible detection of debonded regions. However, the wavelength at 1 KHz is 2.4 meters, which indicates that only large areas could be inspected. To achieve high resolution, it is necessary to use much higher frequency waves, for which the continuum model of the honeycomb is not valid.

#### B. Lamb Modes of the Aluminum Plate

When treating the symmetric and anti-symmetric (flexural) Lamb modes, it is necessary to include SV and P plane waves in the plate that have components of propagation in the  $+z$  direction as well as in

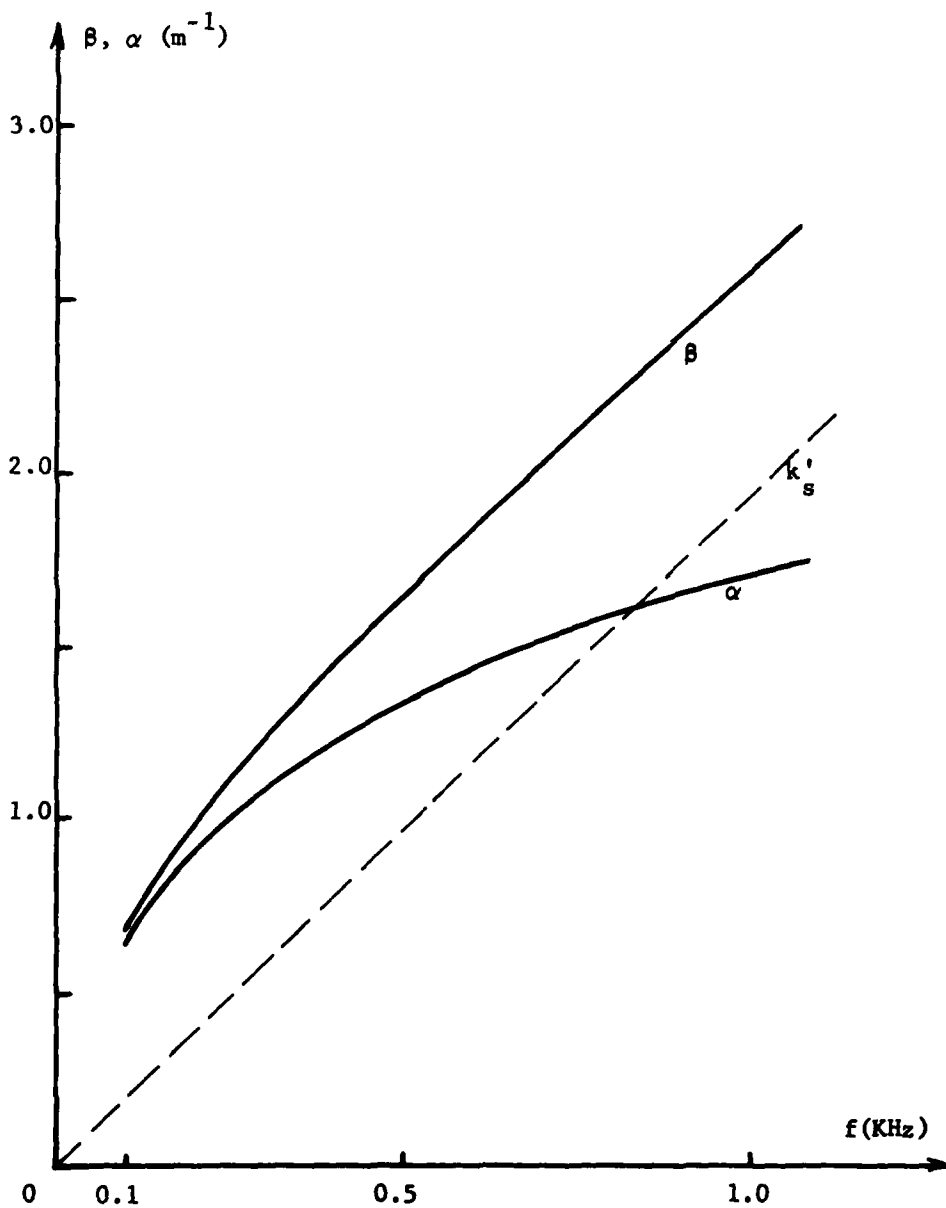


Figure 37. Attenuation constant  $\alpha$  and propagation constant  $\beta$  of the SH leaky wave guided by an aluminum face plate bonded to a semi-infinite honeycomb.

the  $-z$  direction. The fields in the honeycomb are composed of the Q-P and Q-SV Bloch waves propagating in the  $-z$  direction. The amplitude of these six waves are designated as  $A^+$ ,  $B^+$ ,  $C^+$  and  $D^+$  in Figure 36. The boundary conditions on  $v_x$ ,  $v_z$ ,  $T_{xz}$  and  $T_{zz}$  at  $z = \pm h/2$  requires that all of the plane waves have the same wave-number  $k_x$  along  $x$ . By requiring that the plane waves satisfy the boundary conditions, one obtains the dispersion equation for the guided waves.

#### 1. Formal Solution for the Guided Waves

The fields in the plate are given by the sum of four plane wave constituents. The particle velocity is given by<sup>(3)</sup>

$$v_x(x, z) = \left\{ \left[ A^+ e^{-jk'_{zs}z} + A^- e^{jk'_{zs}z} \right] + \frac{k_x}{k_p} \left[ B^+ e^{-jk'_{zp}z} + B^- e^{jk'_{zp}z} \right] \right\} e^{-jk_x x} \quad (97)$$

and

$$v_z(x, z) = \left\{ -\frac{k_x}{k_{zs}} \left[ A^+ e^{-jk'_{zs}z} - A^- e^{jk'_{zs}z} \right] + \frac{k_{zp}}{k_p} \left[ B^+ e^{-jk'_{zp}z} - B^- e^{jk'_{zp}z} \right] \right\} e^{-jk_x x} \quad (98)$$

Here

$$k'_{zs} = \sqrt{(k_s')^2 - k_x^2}; \quad k'_{zp} = \sqrt{(k_p')^2 - k_x^2} \quad (99)$$

where  $k'_s$  and  $k'_p$  are the wavenumbers of the shear and longitudinal waves in the aluminum. The components of stress entering into the boundary conditions are

$$T_{xz}(x, z) = \left\{ -\frac{\mu'}{\omega k'_{zs}} \left[ (k'_{zs})^2 - k_x^2 \right] \left[ A^+ e^{-jk'_{zs}z} - A^- e^{jk'_{zs}z} \right] - 2\mu' \frac{k'_{zp} k_x}{(k'_p)^2} \left[ B^+ e^{-jk'_{zp}z} - B^- e^{jk'_{zp}z} \right] \right\} e^{-jk_x x} \quad (100)$$

and

$$T_{zz}(x, z) = \left\{ \frac{2\mu' k_x}{\omega} \left[ A^+ e^{-jk'_{zs}z} + A^- e^{jk'_{zs}z} \right] - \frac{k'_p}{\omega} \left[ \lambda' + 2\mu' \left( \frac{k'_{zp}}{k'_p} \right)^2 \right] \left[ B^+ e^{-jk'_{zp}z} + B^- e^{jk'_{zp}z} \right] \right\} e^{-jk_x x} \quad (101)$$

where  $\lambda'$  is the Lamé coefficient of the aluminum.

To obtain the fields in the honeycomb, we make use of the properties of a hexagonal continuum<sup>(13)</sup>. Thus, the wavenumbers  $k_{zs}$  and  $k_{zp}$  of the Q-S and Q-P waves can be found from the dispersion equation

$$(C_{11} k_x^2 + C_{44} k_z^2 - \rho_H \omega^2)(C_{44} k_x^2 + C_{33} k_z^2 - \rho_H \omega^2) - (C_{13} + C_{44})^2 k_x^2 k_z^2 = 0. \quad (102)$$

The components of particle velocity are

$$v_x(x, z) = \left[ C^- e^{jk_{zp}z} + D^- e^{jk_{zs}z} \right] e^{-jk_x x} \quad (103)$$

and

$$v_z(x, z) = \left[ C^- \delta e^{jk_{zp}z} + D^- \gamma e^{jk_{zs}z} \right] e^{-jk_x x} \quad (104)$$

where

$$\gamma = \frac{C_{11}k_x^2 + C_{44}k_{zs}^2 - \rho_H \omega^2}{(C_{13} + C_{44})k_x k_{zs}} \quad (105)$$

and

$$\delta = \frac{(C_{13} + C_{44})k_x k_{zp}}{C_{44}k_x^2 + C_{33}k_{zp}^2 - \rho_H \omega^2} \quad (106)$$

Finally, the components of stress entering the boundary conditions can be found from

$$T_{xz}(x, z) = \frac{C_{44}}{\omega} \left[ C^- (-k_x \delta + k_{zp}) e^{jk_{zp}z} + D^- (-k_x \gamma + k_{zs}) e^{jk_{zs}z} \right] e^{-jk_x x} \quad (107)$$

and

$$T_{zz}(x, z) = \frac{C_{33}}{\omega} \left[ C^- \left( -k_x \frac{C_{13}}{C_{33}} + k_{zp} \delta \right) e^{jk_{zp}z} + D^- \left( -k_x \frac{C_{13}}{C_{33}} + k_{zs} \gamma \right) e^{jk_{zs}z} \right] e^{-jk_x x} \quad (108)$$

The boundary conditions at  $z = h/2$  require that  $T_{xz}(x, h/2)$  and  $T_{zz}(x, h/2)$  vanish. At the interface  $z = -h/2$ , the velocity components  $v_x(x, -h/2)$  and  $v_z(x, -h/2)$  together with the stress components  $T_{xz}(x, -h/2)$  and  $T_{zz}(x, -h/2)$  must be continuous. These conditions take the form of six homogeneous equations in the six unknown

amplitude coefficients. These equations can be written in the form

$$[\underline{L}] \begin{bmatrix} A^+ e^{jk'_{zs} h/2} \\ A^- e^{-jk'_{zs} h/2} \\ B^+ e^{jk'_{zp} h/2} \\ B^- e^{-jk'_{zp} h/2} \\ C^- e^{-jk'_{zp} h/2} \\ D^- e^{-jk'_{zs} h/2} \end{bmatrix} = 0 \quad (109)$$

where the 6x6 matrix  $\underline{L}$  is given in Table IV. The elements in the matrix depend on  $\omega$  and  $k_x$ . Hence, setting the determinant of  $\underline{L}$  equal to zero in order for (109) to have non-trivial solutions, gives the dispersion equation for the guided waves in the form  $f(k_x, \omega) = 0$ .

## 2. Numerical Evaluation of the Dispersion Characteristics

Results obtained for the dispersion characteristics of the leaky Lamb mode are summarized in Figure 38, where we have plotted the phase constant  $\beta$  and attenuation constant  $\alpha$  as a function of frequency. For comparison we have also plotted the wavenumber  $k'_L$  of the symmetric Lamb mode of a free aluminum plate. It is seen that the honeycomb slows the wave so that  $\beta > k'_L$  and causes it to radiate or leak into the honeycomb. The attenuation becomes constant with frequency above 2KHz and corresponds to a  $1/e$  attenuation length of 0.8 m. At 10KHz, the wavelength  $2\pi/\beta = 0.56$  m, so that wave is strongly attenuated per wavelength.



TABLE IV  
ELEMENTS OF THE MATRIX  $\bar{L}$

$L_1 e^{-jk_{zs}h}$	$L_1 e^{jk_{zs}h}$	$L_2 e^{-jk_{zp}h}$	$L_2 e^{jk_{zp}h}$	0
$-L_3 e^{-jk_{zs}h}$	$L_3 e^{jk_{zs}h}$	$-L_1 \frac{k_{zp}}{k_p} e^{-jk_{zp}h}$	$L_1 \frac{k_{zp}}{k_p} e^{jk_{zp}h}$	0
1	1	$k_x/k_p$	$k_x/k_p$	-1
$-k_x/k_{zs}$	$k_x/k_{zs}$	$k_{zp}/k_p$	$k_{zp}/k_p$	$-\gamma$
$L_1$	$L_1$	$L_2$	$L_2$	$\frac{C_{33}}{\omega} (k_x \frac{C_{13}}{C_{33}} - k_{zp} \delta)$
$-L_3$	$L_3$	$-L_1 k_{zp}/k_p$	$L_1 k_{zp}/k_p$	$\frac{C_{44}}{\omega} (k_x \gamma - k_{zs})$

$$L_1 = \frac{2\mu k_x}{\omega}$$

$$L_2 = -\frac{k_p}{\omega} \left[ \lambda' + 2\mu \left( \frac{k_{zp}}{k_p} \right)^2 \right]$$

$$L_3 = \frac{\mu}{\omega k_{zs}} \left[ (k_{zs}')^2 - k_x^2 \right]$$

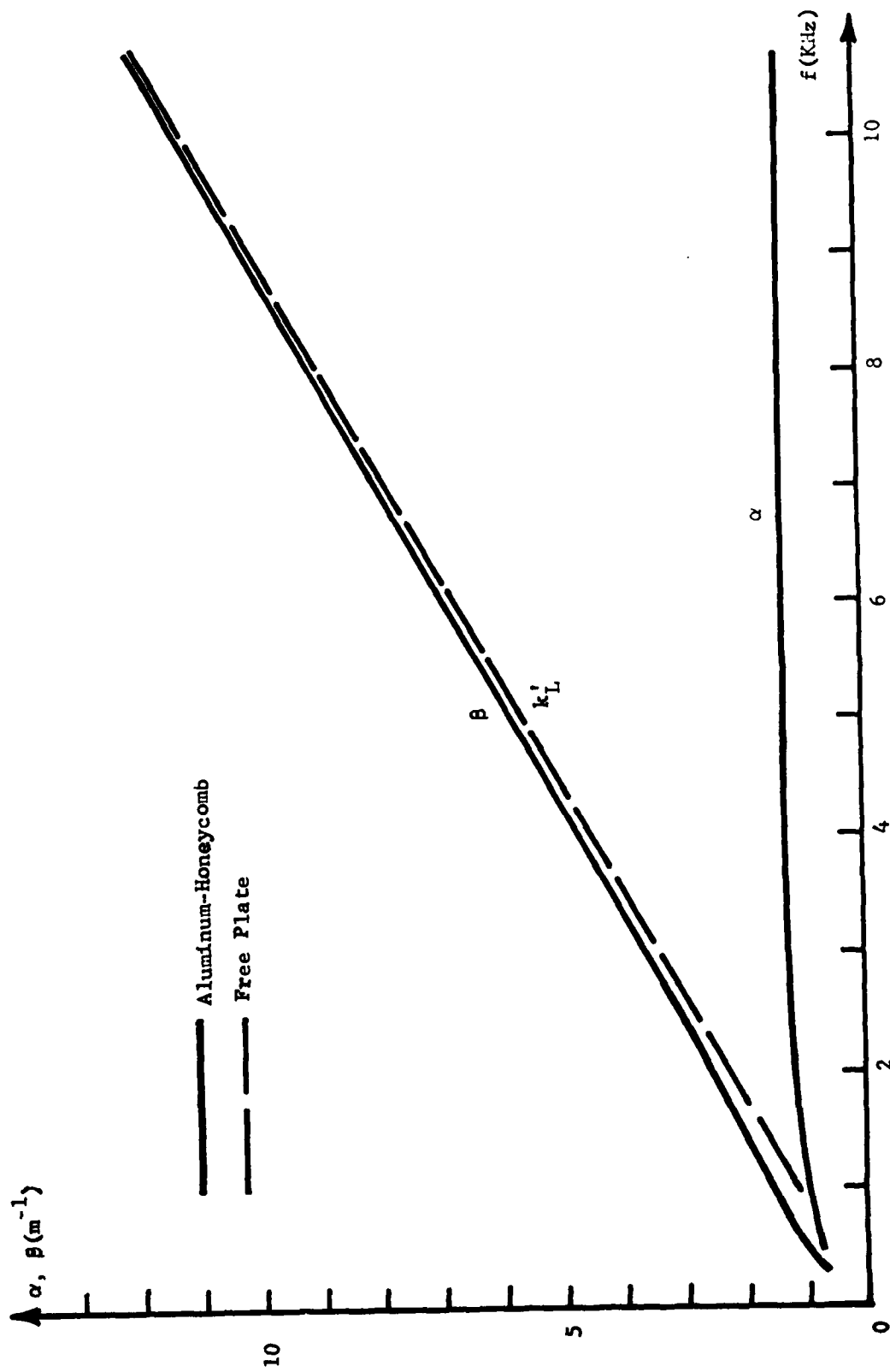


Figure 38. Attenuation constant  $\alpha$  and propagation constant  $\beta$  of the leaky Lamb wave guided by an aluminum face plate bonded to a semi-infinite honeycomb.

The flexural mode of the aluminum plate is slow compared to the Q-SH and Q-SV waves of the honeycomb for frequencies below 10 KHz. As a result, it is expected that this mode will not leak into the honeycomb, but remain a bound surface wave in the plate. This supposition is borne out by the values obtained for the root of the dispersion equation, from which it is found that the attenuation constant  $\alpha = 0$ . In Figure 39 we have plotted  $\beta$  obtained from the dispersion equation. For comparison we have plotted the wavenumber  $k_F'$  of the flexural wave in a free plate and the wavenumber  $k_R$  of the Rayleigh wave propagating on a z-cut hexagonal continuum having the elastic constants taken for the honeycomb at low frequencies. Below 3 KHz the surface wave is essentially a Rayleigh wave in the honeycomb. At higher frequencies the plate acts as a perturbation on the honeycomb and  $\beta$  deviates from  $k_R$ . The surface wave is slow compared to the leaky Lamb mode shown in Figure 38. At 10 KHz, the wavelength of the surface wave is 0.057 m or 5.7 cm, which is an order of magnitude smaller than that of the Lamb mode.

For application to NDE, it is necessary that the wavelength be on the order of the cell diameter, which is about 1 cm. Thus, the flexural mode would be useful at frequencies somewhat above 10 KHz. However, the Lamb and SH modes would require frequencies above 100 KHz to achieve such small wavelengths. Such high frequencies lie in higher pass or stop bands of the honeycomb, where the periodicity of the honeycomb is significant, and must be accounted for in computing the leaky wave characteristics. It therefore seems most convenient to use the flexural mode for NDE applications. This mode also offers the advantage of a large difference between  $k_F'$  and  $\beta$ , so that debonded regions of the honeycomb are easily distinguished from bonded regions.

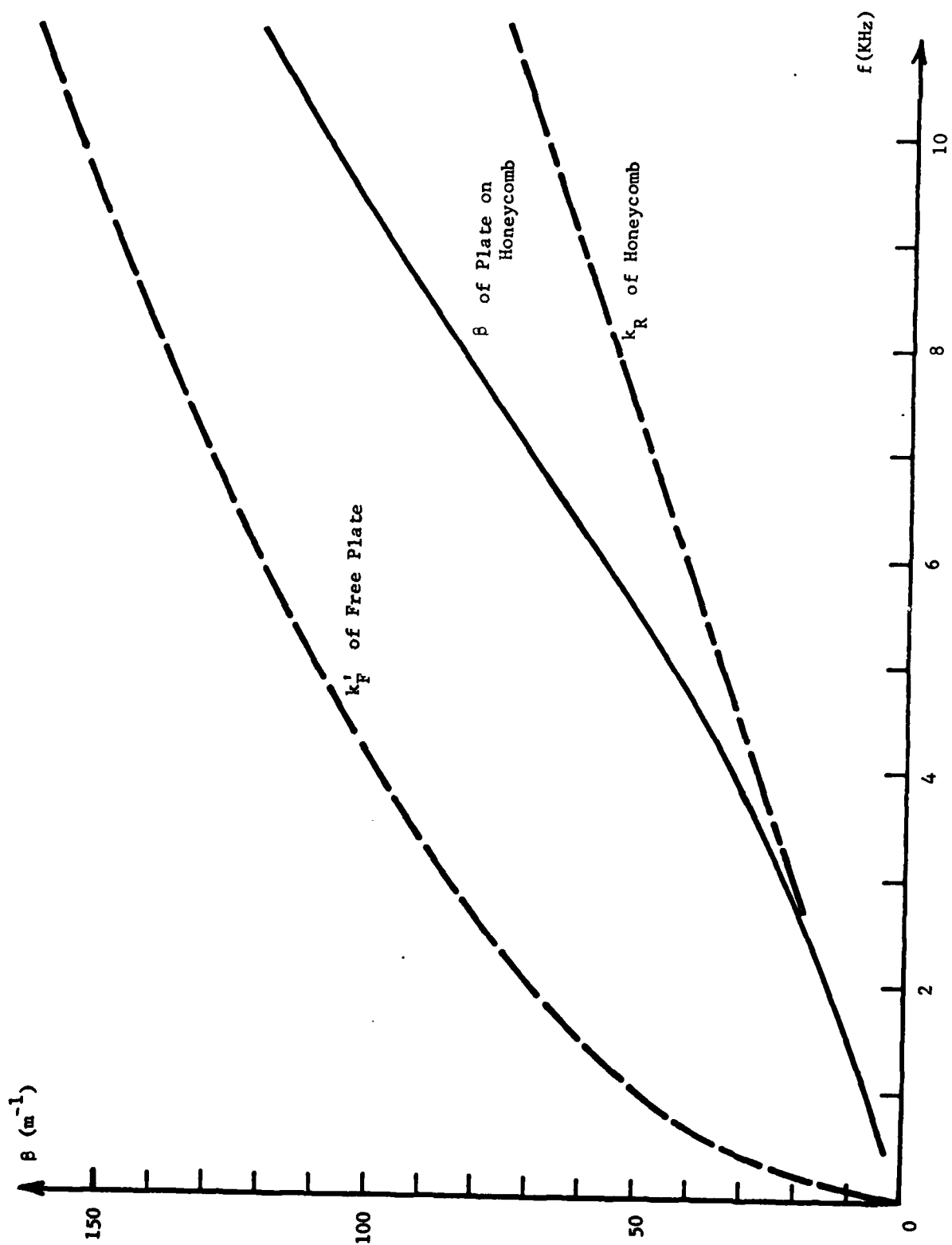


Figure 39. Propagation constant  $\beta$  of the flexural mode guided by an aluminum face plate bonded to a semi-infinite honeycomb. For this mode  $\alpha=0$ .

## VII. FOAM CORE PANELS

We consider here wave propagation in form core panels in the frequency rang  $100 \text{ KH}_z$  to  $1 \text{ MH}_z$  for application to NDE. In this frequency range, the acoustic attenuation in the foam is large. As a result, elastic waves excited in one face plate will be highly attenuated by the time they reach the opposite face plate. Because of this property, the wave propagation can accurately be determined by considering a single face plate bonded to a semi-infinite foam block, as was done for the honeycomb in the previous section. For this geometry we examine the perturbation due to the foam in the modes guided by the face plate.

Two methods exist for bonding the foam to the aluminum. For one method the chemical agents used to produce the foam are allowed to react directly on the aluminum. In the process of reacting, the foam becomes bonded to the aluminum. In the second method, preformed foam slabs are glued to the aluminum. This second method introduces an additional glue layer whose elastic properties greatly influence the characteristics of the guided wave<sup>(14)</sup>. In what follows, we consider separately the aluminum-foam case and the aluminum - glue - foam configuration.

It is assumed that the aluminum plate has thickness  $1/16$  in. and the elastic constants used for the foam are the nominal values listed for rigid polyurethan foams<sup>(15)</sup>. The glue was assumed to be a syntactic epoxy<sup>(15)</sup>. Elastic constants used for the various materials are listed in Table V. The method of analysis used to find the propagation constants of the guided waves is the same as that discussed in the previous section. For the aluminum - foam case, the expressions of

the previous section can be used directly by substituting the mass density of the foam for  $\rho_H$  and setting  $C_{11} = C_{33} = \lambda_f + 2\mu_f$ ,  $C_{12} = C_{13} = \lambda_f$  and  $C_{44} = \mu_f$ , where  $\lambda_f$  and  $\mu_f$  are the Lamé constants for the foam. For the aluminum - glue - foam configuration, a similar analysis is applied that accounts for the plane waves in the glue layer.

#### A. Aluminum - Foam Configuration

In Table V we have listed the shear and longitudinal wave velocities of the materials, as computed from the elastic constants that are listed there. It is seen that the wave velocities in foam are much smaller than those in aluminum, so that the SH and symmetric Lamb modes guided by the plate will radiate or leak energy into the foam. Over the frequency range considered here even the flexural mode of the plate is fast compared to the waves in the foam, so that this wave will also be of the leaky type.

The wavenumber  $k_x$  of the leaky waves takes the form  $k_x = \beta - j\alpha$ , where  $\beta$  is the phase constant and  $\alpha$  the attenuation constant that results from the radiation into the foam. Because of the low density of the foam, its presence does not significantly perturb the value of  $\beta$ . In Figure 40 we have plotted the phase constant  $\beta$  for the lowest flexural mode F(0) and lowest symmetric Lamb mode L(0) normalized to the shear wavenumber  $k'_s$  in the aluminum. This plot applies to both the free plate, and to the foam covered plate. Note that  $\beta$  for the lowest SH plate mode SH(0) is equal to  $k'_s$ .

The attenuation constant  $\alpha$ , normalized to  $k'_s$ , for the leaky waves is plotted in Figure 41. Because of the low values for  $\alpha$ , the waves can propagate over several hundred wavelengths before experiencing significant attenuation. For example, the SH(0) mode at 0.5 MHz propagates

TABLE V

Material Properties for Foam Core Panels

	Aluminum	Foam	Glue
$\rho' (k_g / m^3)$	$2.70 \times 10^3$	48	$5.8 \times 10^2$
$\lambda (N / m^2)$	$6.13 \times 10^{10}$	$3.17 \times 10^6$	$2.2 \times 10^9$
$\mu (N / m^2)$	$2.85 \times 10^{10}$	$1.45 \times 10^6$	$5.6 \times 10^8$
$C_s (m / s)$	$3.25 \times 10^3$	$1.74 \times 10^2$	$9.83 \times 10^2$
$C_p (m / s)$	$6.62 \times 10^3$	$3.56 \times 10^2$	$2.39 \times 10^3$

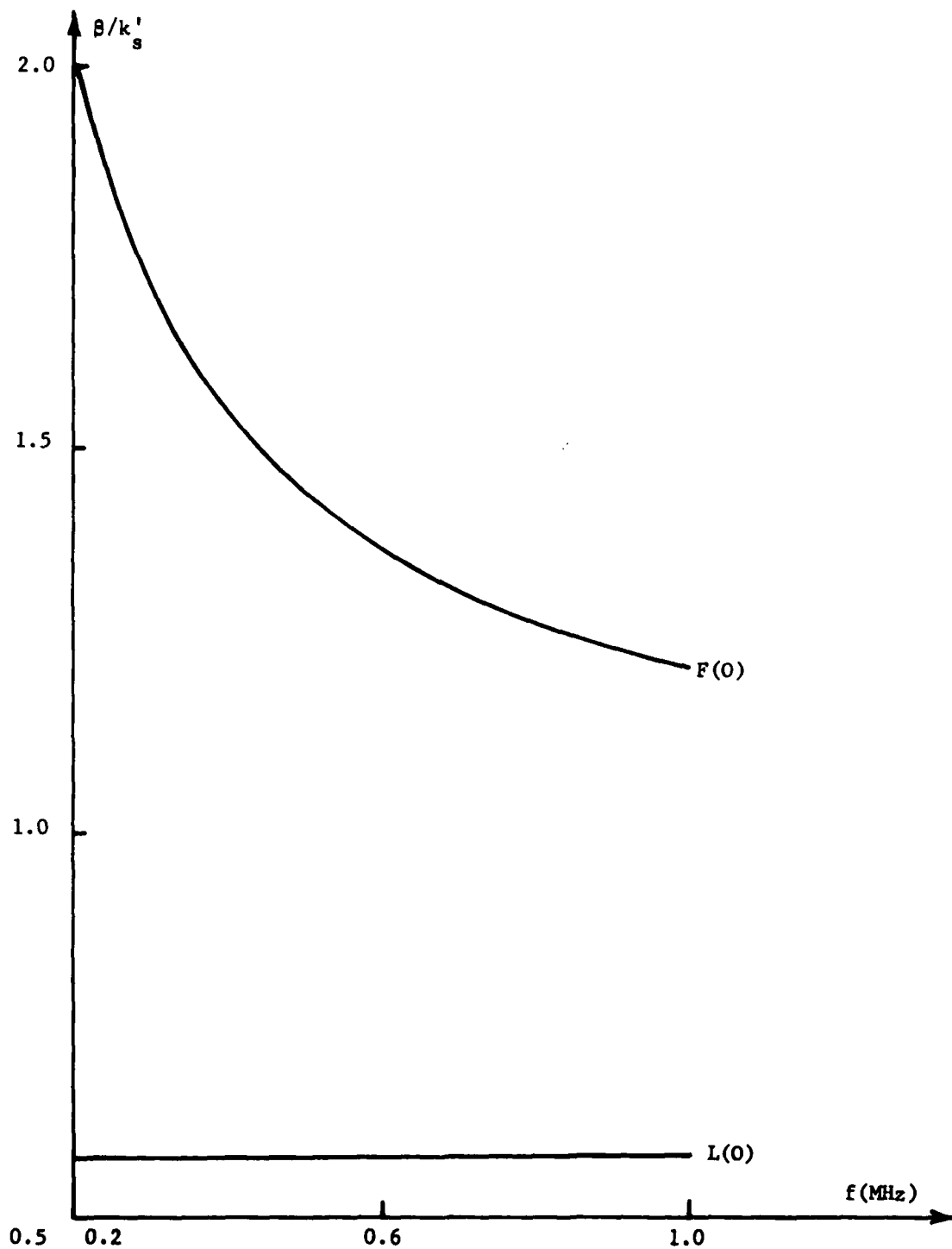


Figure 40. Propagation constants  $\beta$  of the  $L(0)$  and  $F(0)$  leaky wave modes of a 1/16 in. aluminum plate on which a polyurethane foam has been formed. These curves are numerically the same as those found for a free plate.



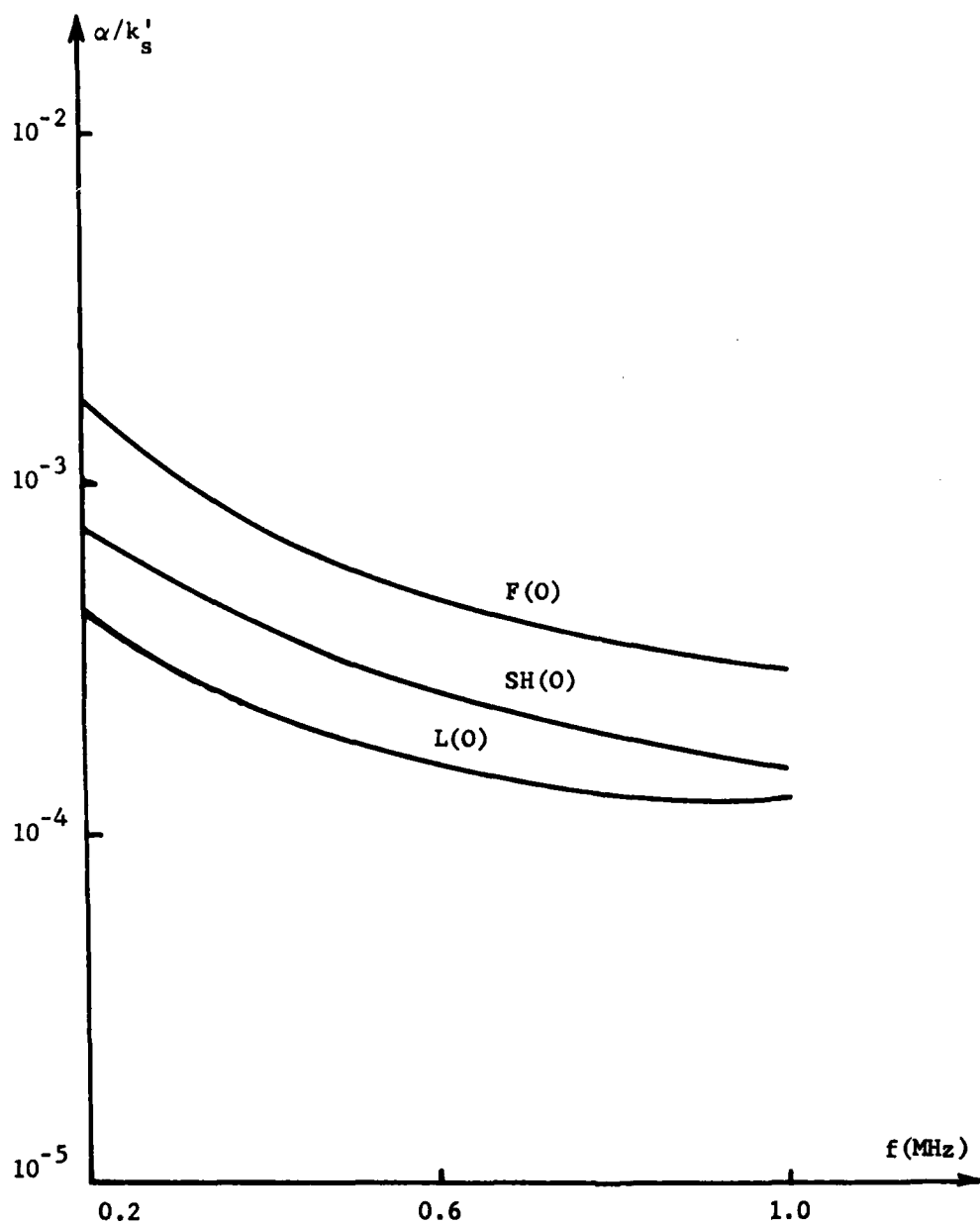


Figure 41. Attenuation constants  $\alpha$  of the L(0), SH(0) and F(0) leaky wave modes of a 1/16 in. aluminum plate on which a polyurethane foam has been formed.

500 wavelengths, or about 3.3 meters before attenuating by  $1/e$ .

Because the foam can have a high attenuation constant at those frequencies, we have investigated the effect of loss on the curves in Figures 40 and 41. No significant effect was found up to a loss tangent of unity. This observation indicates that the rate at which guided wave in the aluminum plate sheds energy into the foam is not strongly dependent on the loss tangent. However, the foam attenuation will prevent the radiated energy from reaching the second aluminum plate in a panel.

### B. Aluminum - Glue - Foam Configuration

The presence of the glue layer has two significant effects on the wave propagation. First, even without the foam it makes the effective plate thickness greater, so that higher plate modes can propagate. Second it acts as an impedance match between the aluminum and foam, so that the perturbation caused by the foam is much greater. We first consider these effects for the SH modes, and subsequently treat the Lamb modes.

#### 1. SH Modes

The propagation constant  $\beta$ , normalized to  $k'_g$  is indicated in Figure 42 for both the aluminum - glue and aluminum - glue - foam combinations. In computing the curves of Figure 42, the glue layer was assumed to be  $1/64$  in. thick, which is  $1/4$  of the thickness of the aluminum. At low frequencies where only the SH(0) mode propagates, in the aluminum - glue combination  $\beta$  is seen to be nearly equal to  $k'_g$ , indicating that the energy in the wave is carried primarily in the aluminum with only a small fraction in the glue. As the frequency increases above  $0.6 \text{ MHz}$ , the SH(0) mode shows dispersion and the SH(1) mode goes above cut off.

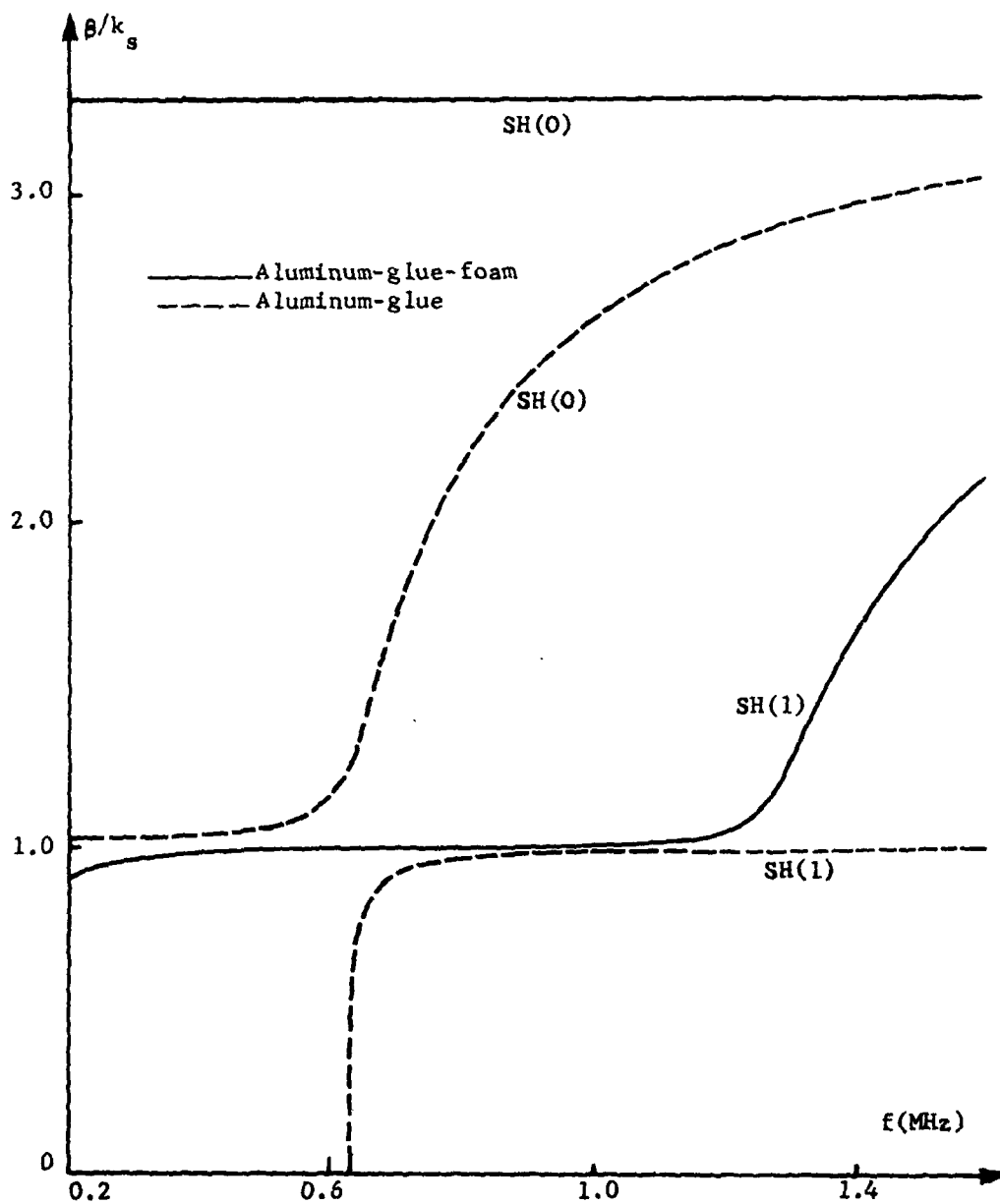


Figure 42. Propagation constants  $\beta$  of the SH(0) and SH(1) modes of a 1/16 in. aluminum plate covered with 1/64 in. of glue, with and without bonding to a semi-infinite polyurethane foam.

For the SH(0) mode,  $\beta/k'_g$  tends towards the value 3.3, which is the ratio of the shear wavenumber in the glue to that in the aluminum. This behavior of  $\beta$  indicates that the energy of the wave is concentrated in the glue. The energy of the SH(1) mode for frequencies somewhat above cut off is concentrated in the aluminum.

When the foam is taken into account the dispersion characteristics appears to shift to lower frequencies. Thus over the frequency range computed, the SH(0) mode has  $\beta \approx 3.3 k'_g$ , while the cut off of the SH(1) mode is below 0.2 MHz. For frequencies above cut off of the SH(1) mode,  $\beta$  is initially close to  $k'_g$  and then increases towards the shear wavenumber in the glue. As before, this behavior suggests that the energy of the wave is carried primarily in the aluminum at lower frequency, and then becomes concentrated in the glue at higher frequencies.

The attenuation constant  $\alpha$ , normalized to  $k'_g$ , is plotted in Figure 43 as a function of frequency. For the SH(0) mode,  $\alpha$  is larger than that in Figure 41 for the aluminum - foam combination by two orders of magnitude. Thus  $1/e$  attenuation length is on the order of five times the shear wavelength, or  $5 \times 3.3 \approx 17$  times the wavelength  $2\pi/\beta$  of the guided wave. The high attenuation constant is a result of the fact that the energy of the SH(0) mode at these frequencies is concentrated in the glue layer, whose elastic properties are much closer to the foam properties than are those of aluminum. This interpretation is supported by the SH(1) mode whose attenuation is lowest when the energy is concentrated in the aluminum layer, and highest when the energy is concentrated in the glue.

From the viewpoint of NDE, the distinct properties cited above for the aluminum, aluminum-glue, and aluminum-glue-foam combinations

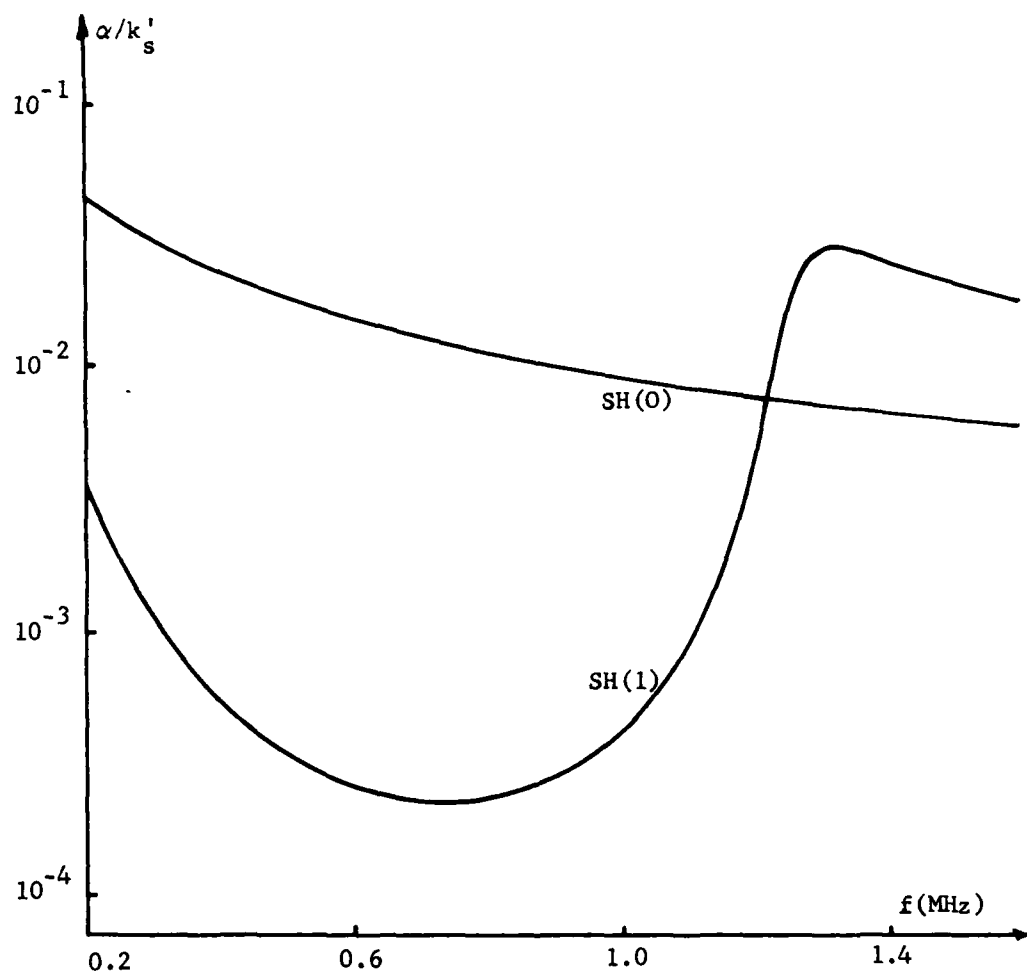


Figure 43. Attenuation constants  $\alpha$  of the SH(0) and SH(1) leaky wave modes of a 1/16 in. aluminum plate covered with 1/64 in. of glue that bonds the plate to a semi-infinite polyurethane foam.

facilitate inspection of foam core panels for regions of de-bonding. Regions of the aluminum plate lacking in glue, or having glue but not bonded to the foam have very different values of  $\beta$  and  $\alpha$ , and hence can be distinguished by phase and attenuation measurements. For example, consider a pair of transducers designed to launch and receive SH waves with  $\beta = 3.3k'_s$  at 0.4 MHz. When placed over a portion of the plate glued to the foam, the output of the receiving transducer will have some finite value due to the radiation and detection of the surface wave. Over a portion of the plate not glued to the foam, the output will have a lower value since the surface wave has a different wavelength and will not be strongly excited or detected. Thus, unglued regions can be detected from changes in receiver output.

## 2. Lamb Modes

Because of coupling between P and SV plane wave constituents, the dispersion characteristics of the Lamb modes are more complex than for the SH modes. The propagation constant  $\beta$ , normalized to  $k'_s$  is plotted in Figure 44 for the lowest four Lamb modes. The labeling L(0), F(0), F(1) and L(1) is made in accordance with their low frequency behavior, since the modes cannot be uniquely separated on the basis of symmetry in the composite plate. Curves for the aluminum - glue combination are shown dashed, while those for aluminum - glue - foam are solid. The dispersion curve of the L(0) mode in the presence of foam could not be traced past 0.65 MHz because of convergence difficulties in the computer program. Comparing the curves of the L(0) and F(0) modes with those of an aluminum plate as shown in Figure 40, it is seen that the presence of the glue significantly influences the high frequency behavior of the modes.

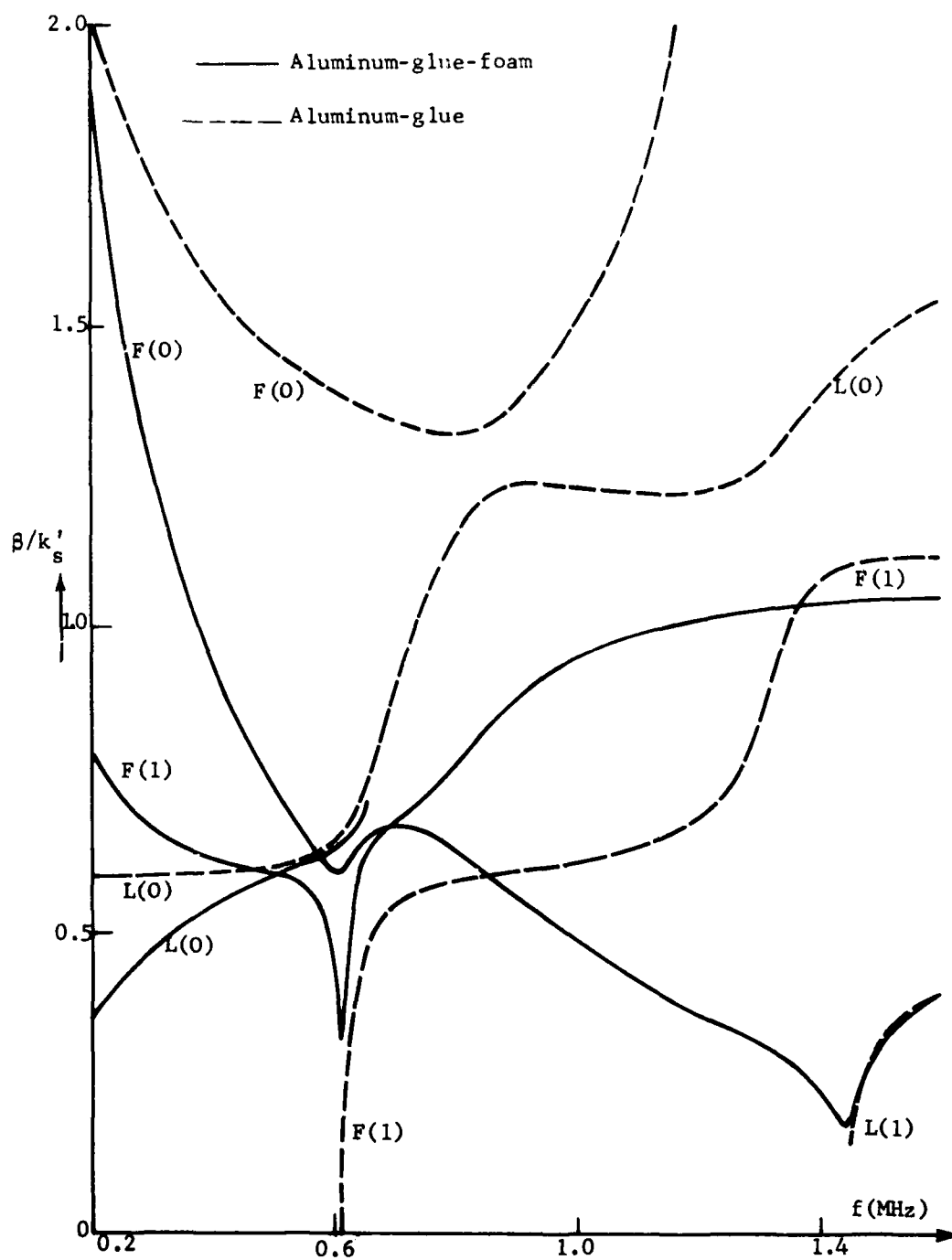


Figure 44. Propagation constants  $\beta$  of Lamb modes of a 1/16 in. aluminum plate covered with 1/64 in. of glue, with and without bonding to a semi-infinite polyurethane foam.

The presence of the foam is also seen to cause major changes in the propagation constant, as well as introduce attenuation. In Figure 45 we have plotted the attenuation constant  $\alpha$  normalized to  $k'_s$  for the curves labeled F(0) L(0) and F(1) in Figure 44. While the curves  $\beta(\omega)$  for the three modes intersect,  $\alpha$  for each mode is different at the intersection frequency, so that all three branches of the dispersion equation are distinct. The F(0) branch has high attenuation at low frequency, which decreases with frequency. Similarly, the attenuation of the F(1) branch decreases dramatically past the cut off frequency of the F(1) mode in the aluminum - glue combination. The low values of  $\alpha$  for the L(0) and F(1) modes away from 0.64 MHz are consistent with the values obtained in the aluminum - foam combination. The F(0) mode however shows much higher  $\alpha$ .

The curves of Figures 44 and 45 indicated that the presence of glue and adhesion to the foam can be determined from measurement of  $\alpha$  and  $\beta$  for the Lamb modes, as discussed in the previous section. However, a more complete analysis of the mode properties and their dependence on layer thickness is required to devise effective test procedures.



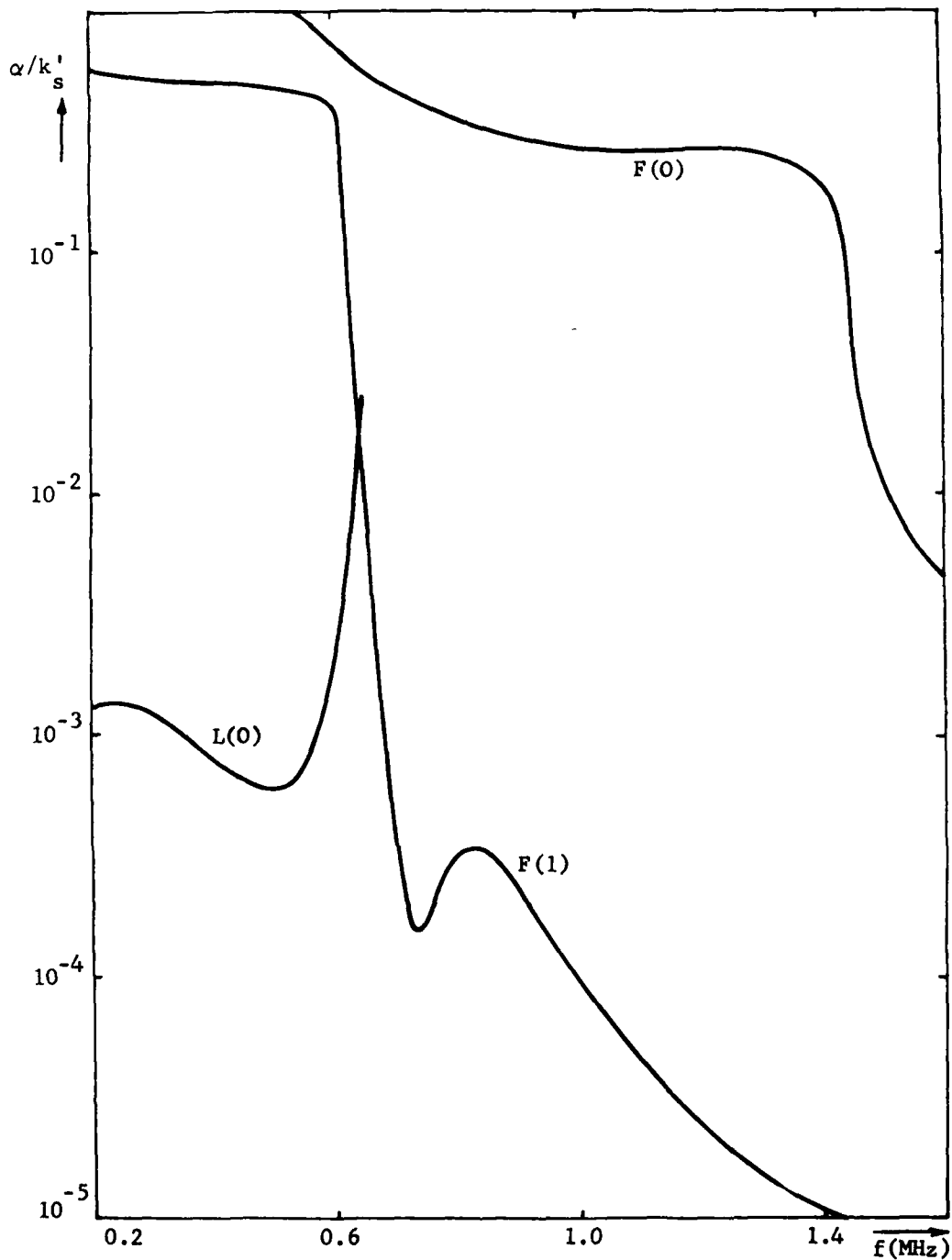


Figure 45. Attenuation constants  $\alpha$  of Lamb modes of a 1/16 in. aluminum plate covered with 1/64 in. of glue, with and without bonding to a semi-infinite polyurethane foam.

# Appendix: Thin Plate Approximation of the Plate Modes

The geometry of an infinite plate is illustrated in Figure A-1. The total fields in the plate can be expressed as a superposition of the modal fields of an infinite plate. In general, we are concerned with modes propagating obliquely with respect to the  $x$  axis. These modes will couple at junction planes perpendicular to  $x$ , at which we must satisfy boundary conditions involving the particle velocity  $\underline{v}$  and the surface traction  $\underline{x}_0 \cdot \underline{T}$ .

Obliquely traveling modes in an infinite plate have  $x$ - $z$  dependence of the form  $\exp[-j(\pm k_x x + k_z z)]$  where  $\sqrt{k_x^2 + k_z^2}$  is equal to the modal wavenumber. In order to satisfy boundary conditions at junction planes perpendicular to  $x$ , all modes must have the same transverse wavenumber  $k_z$ . Because of scattering at the junction, plate modes having both  $\pm x$  components of propagation must be accounted for, as indicated in the spatial dependence cited above. In addition, the fields of the plate modes have a variation with  $y$ , i.e., in the direction through the plate.

In the microwave network representation of guided acoustic waves, the six quantities  $\underline{v}$  and  $\underline{x}_0 \cdot \underline{T}$  entering the boundary conditions are organized into  $1 \times 3$  matrices  $\underline{G}$  and  $\underline{Q}$ , which are

$$\left. \begin{aligned} \underline{G} &= \begin{bmatrix} v_y \\ v_z \\ T_{xx} \end{bmatrix} = \underline{g}(y, z) \underline{V}(x) \\ \underline{Q} &= \begin{bmatrix} T_{xy} \\ T_{xz} \\ v_x \end{bmatrix} = \underline{q}(y, z) \underline{I}(x) \end{aligned} \right\} \quad (A-1)$$

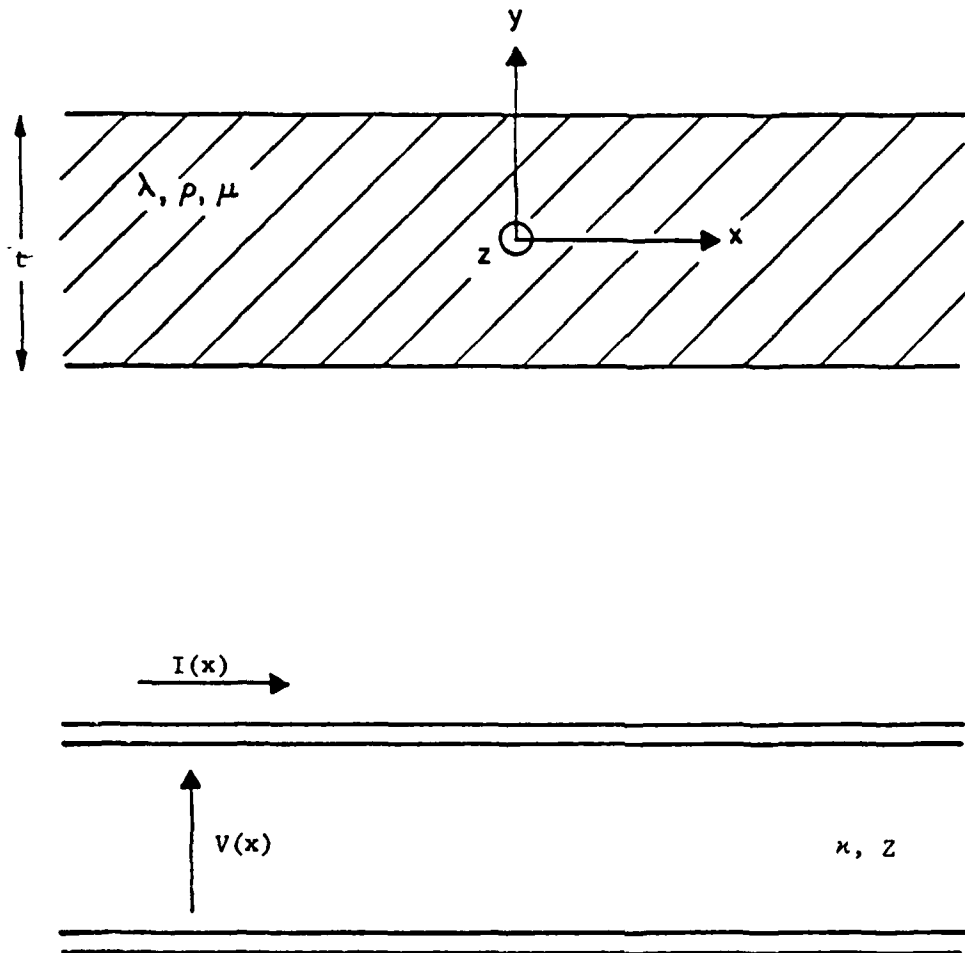


Figure A-1 Geometry of an infinite plate and the transmission line representation for a given plate mode, taking the transmission direction to be along  $x$ .

Here  $\underline{g}(y,z)$  and  $\underline{q}(y,z)$  are the "mode vectors" describing the variation of the fields transverse to  $x$ , and the relative amplitude of the various field quantities. As discussed above, the  $z$  variation of  $\underline{g}(y,z)$  and  $\underline{q}(y,z)$  is contained in the factor  $\exp(-jk_z z)$ . The modal voltage  $V(x)$  and current  $I(x)$  satisfy standard "electrical" transmission line equations involving the wavenumber  $\kappa$  and modal impedance  $Z$ , as indicated in Figure A-1. The voltage and current are composed of traveling wave solutions having  $x$  dependence  $\exp(\pm j\kappa x)$ .

The dispersion relation giving the wavenumber  $\sqrt{\kappa^2 + k_z^2}$  of each mode, and the transmission line representation of the plate modes have been derived by Markman, et al<sup>(5, 6)</sup>. In this Appendix, we approximate their results for  $\kappa$ ,  $Z$  and the mode vectors for the case of a thin plate, whose thickness is small compared to the acoustic wavelength.

#### A. Lamb Modes of an Infinite Plate

Lamb waves in the plate are characterized by having components of particle displacement perpendicular to the faces of the plates and components parallel to the direction of propagation.

##### 1. Lowest Symmetric Mode: $L(0)$

The symmetric Lamb modes are those for which the particle velocity in the direction of propagation is an even function of  $y$ , whereas the transverse particle velocity  $v_y$  is an odd function of  $y$ .

The dispersion relation of the symmetric modes of the plate, which gives the Lamb wavenumber  $k_L = \sqrt{\kappa^2 + k_z^2}$  as a function of frequency may be written as

$$\left( \frac{\kappa_s^2 - k_L^2}{k_s^2} \right)^2 \frac{k_s}{\kappa_p} \cot \kappa_p \frac{t}{2} + \frac{4k_L^2 \kappa_s}{k_s^3} \cot \kappa_s \frac{t}{2} = 0. \quad (A-2)$$

Here the wavenumbers along y,  $\kappa_p$  and  $\kappa_s$ , are functions of  $k_L$  and  $\omega$  defined by the relationships

$$\left. \begin{aligned} k_L^2 + \kappa_p^2 &= k_p^2 \equiv \omega^2 \frac{\rho}{\lambda + 2\mu} \\ k_L^2 + \kappa_s^2 &= k_s^2 \equiv \omega^2 \frac{\rho}{\mu} \end{aligned} \right\}, \quad (A-3)$$

where  $\lambda$  and  $\mu$  are the Lamé constants,  $\rho$  is the mass density and  $\omega$  is the radian frequency.

The modal fields obtained by summing the contributions from the P and SV plane waves, which are reflected back and forth between the faces of the plate, are

$$\underline{g}(y, z) = \frac{1}{N_L} \left\{ \begin{aligned} & -j \frac{1}{\sqrt{\mu\rho}} \frac{\kappa_p}{k_s} \sin \kappa_p y \\ & \frac{1}{\sqrt{\mu\rho}} \frac{k_z}{k_s} \cos \kappa_p y \\ & - \frac{1}{k_s^2} (k_s^2 - 2\kappa_p^2 - 2k_z^2) \cos \kappa_p y \end{aligned} \right\} \quad (A-4)$$

$$+ \frac{\kappa_p \cos \kappa_p \frac{t}{2}}{\kappa_s \cos \kappa_s \frac{t}{2}} \left\{ \begin{aligned} & j \frac{1}{\sqrt{\mu\rho}} \frac{k_L}{\kappa_s} \sin \kappa_s y \\ & \frac{1}{\sqrt{\mu\rho}} \frac{k_z}{k_L} \cos \kappa_s y \\ & - 2 \frac{\kappa^2}{k_s k_L} \cos \kappa_s y \end{aligned} \right\} e^{-j k_z z}$$

$$q(y,z) = \frac{\pm 1}{N_L} \left\{ \begin{array}{l} j 2 \sqrt{\mu\rho} \frac{\kappa_p}{k_s} \sin \kappa_p y \\ - 2 \sqrt{\mu\rho} \frac{k_z}{k_s} \cos \kappa_p y \\ \cos \kappa_p y \end{array} \right\} \quad (A-5)$$

$$+ \frac{n_p \cos \kappa_p \frac{t}{2}}{n_s \cos \kappa_s \frac{t}{2}} \left\{ \begin{array}{l} j \sqrt{\mu\rho} \frac{k_s^2}{\kappa_s k_L} \left( 1 - 2 \frac{k_L^2}{k_s^2} \right) \sin \kappa_s y \\ - 2 \sqrt{\mu\rho} \frac{k_z}{k_L} \cos \kappa_s y \\ \frac{k_s}{k_L} \cos \kappa_s y \end{array} \right\} e^{-jk_z z}$$

where

$$\left. \begin{array}{l} n_p = \frac{\kappa_s^2 - k_L^2}{k_s^2} \\ n_s = 2 \frac{k_L}{k_s} \end{array} \right\} \quad (A-6)$$

The characteristic impedance  $Z$  of the modal transmission line is chosen to be

$$Z_L = \pm \omega\rho/\kappa \quad (A-7)$$

where  $\kappa = \sqrt{k_L^2 - k_z^2}$  is the wavenumber in  $x$  direction.

The choice of sign before  $q$  in (A-5) and  $Z_L$  in (A-7) is made such that the normalizing conditions

$$\int_{t/2}^{t/2} \underline{g} \cdot \underline{q}^* dy = -1 \quad (\text{A-8})$$

can be satisfied. With this normalizing condition, the power carried along  $x$  per unit length along  $z$ , is equal to the power  $\frac{1}{2} \text{Re } VI^*$  on the modal transmission line for modes with real or imaginary  $\kappa$ . We impose this condition to facilitate conservation of power test of our results for mode coupling.

Approximate solution to the dispersion equation (A-2) can be obtained for the case of a thin plate at low frequencies ( $\kappa_s t \ll 1$  and  $\kappa_p t \ll 1$ ) by approximating  $\cot \kappa_p \frac{t}{2}$  and  $\cot \kappa_s \frac{t}{2}$  as  $\frac{2}{\kappa_p t}$  and  $\frac{2}{\kappa_s t}$ . This approximation leads to a solution for the wavenumber  $k_L$  of  $L(0)$  mode, which is the lowest symmetric Lamb mode, and the only symmetric Lamb mode that propagates down to zero frequency. It is found that

$$k_L = \sqrt{\frac{1-\nu}{2}} k_s \quad (\text{A-9})$$

where  $\nu$  is Poisson's ratio.

With (A-9) and the approximations  $\cos \theta \approx 1$  and  $\sin \theta \approx \theta$  for  $\theta \ll 1$ , the mode functions in (A-4) and (A-5) can be approximated by

$$\underline{g}(y,z) = \frac{1}{N_L} \begin{bmatrix} 0 \\ \frac{1}{\sqrt{\mu\rho}} \frac{k_z k_s}{2k_L^2} \\ -\frac{1}{1-\nu} + \frac{k_z^2}{k_L^2} \end{bmatrix} e^{-jk_z z} \quad (\text{A-10})$$

$$\underline{q}(y,z) = \frac{1}{N_L} \begin{bmatrix} 0 \\ -\sqrt{\mu\rho} \frac{k_z}{k_s} \frac{2}{1-\nu} \\ \frac{1}{1-\nu} \end{bmatrix} e^{-jk_z z} \quad (\text{A-11})$$

with the characteristic impedance chosen as

$$Z_L = \frac{\omega \rho}{\kappa} \quad (\text{A-12})$$

The normalization constant  $N_L$  obtained via (A-8) is given by

$$N_L = \frac{\sqrt{t}}{1-\nu} \quad (\text{A-13})$$

## 2. Antisymmetric Modes: $F(0)$ and $F(1)$

In the antisymmetric modes  $v_x$  is an odd function of  $y$  whereas  $v_y$  is an even function, with the result that the plate bends or flexes during its motion. These modes are therefore referred to as flexural modes. The dispersion relation giving the wavenumber  $k_F = \sqrt{\kappa^2 + k_z^2}$  of flexural modes as a function of frequency is

$$\left( \frac{\kappa_s^2 - k_F^2}{k_s^2} \right)^2 \frac{k_s}{\kappa_p} \tan \kappa_p \frac{t}{2} + \frac{4k_F^2 \kappa_s}{k_s^2} \tan \kappa_s \frac{t}{2} = 0 \quad (\text{A-14})$$

where the wavenumbers  $\kappa_s$  and  $\kappa_p$  are defined by the relationships

$$k_F^2 + \kappa_p^2 = k_p^2 = \omega^2 \frac{\rho}{\lambda + 2\mu} \quad (\text{A-15})$$

$$k_F^2 + \kappa_s^2 = k_s^2 = \omega^2 \frac{\rho}{\mu}$$

The modal fields are obtained again by summing the fields contributed from P and SV plane waves that are multiply reflected between faces of the plate. The mode vectors are given by



$$g(y, z) = \frac{1}{N} \left\{ \begin{aligned} & \left[ \begin{aligned} & \frac{1}{\sqrt{\mu\rho}} \cos \kappa_p y \\ & - j \frac{1}{\sqrt{\mu\rho}} \frac{k_z}{\kappa_p} \sin \kappa_p y \\ & \frac{j}{k_s \kappa_p} (\kappa_s^2 - 2\kappa_p^2 - 2k_z^2) \sin \kappa_p y \end{aligned} \right] \\ & + \frac{n_s \cos \kappa_p \frac{t}{2}}{n_p \cos \kappa_s \frac{t}{2}} \left[ \begin{aligned} & \frac{1}{\sqrt{\mu\rho}} \frac{k_F}{k_s} \cos \kappa_s y \\ & \frac{j}{\sqrt{\mu\rho}} \frac{\kappa_s}{k_s} \frac{k_z}{k_F} \sin \kappa_s y \\ & - j \frac{2\kappa_s}{k_s} \frac{\kappa_s^2}{k_F^2} \sin \kappa_s y \end{aligned} \right] \end{aligned} \right\} e^{-jk_z z} \quad (A-16)$$

and

$$q(y, z) = \frac{+1}{N} \left\{ \begin{aligned} & \left[ \begin{aligned} & - 2 \sqrt{\mu\rho} \cos \kappa_p y \\ & j 2 \sqrt{\mu\rho} \frac{k_z}{\kappa_p} \sin \kappa_p y \\ & - j \frac{k_s}{\kappa_p} \sin \kappa_p y \end{aligned} \right] + \frac{n_s \cos \kappa_p \frac{t}{2}}{n_p \cos \kappa_s \frac{t}{2}} \left[ \begin{aligned} & \sqrt{\mu\rho} \frac{k_s}{k_F} \left( 1 - 2 \frac{k_F^2}{k_s^2} \right) \cos \kappa_s y \\ & - j 2 \sqrt{\mu\rho} \frac{\kappa_s}{k_s} \frac{k_z}{k_F} \sin \kappa_s y \\ & j \frac{\kappa_s}{k_F} \sin \kappa_s y \end{aligned} \right] \end{aligned} \right\} e^{-jk_z z} \quad (A-17)$$

where  $n_s$  and  $n_p$  are given in (A-6) with  $k_L$  replaced by  $k_F$ .

The characteristic impedance of the modal transmission line is chosen as

$$Z_F = \pm \frac{\omega\rho}{\kappa} \quad (A-18)$$

where  $\kappa = \sqrt{k_F^2 - k_z^2}$  is the wavenumber along x. The signs of q and  $z_F$  are chosen such that (A-8) is satisfied.

There are two significant flexural modes that should be taken for the wave propagation in the thin plate at low frequencies. One of these, the lowest flexural mode,  $F(0)$ , has a real wavenumber even for frequency approaching zero, while the other, the first higher flexural mode,  $F(1)$ , has an imaginary wavenumber. The  $F(1)$  mode cannot be neglected even though it has an imaginary wavenumber since the imaginary wavenumber vanishes as the frequency goes to zero, and since its transverse dependence is similar to that of the  $F(0)$  mode. As a result, the presence of  $F(1)$  strongly influences the amplitude of the  $F(0)$  mode, and other modes, excited at a junction. In addition the  $F(1)$  couples neighboring junctions at low frequencies.

The wavenumbers of the lowest flexural mode,  $k_{F0}$ , and the first higher flexural mode,  $k_{F1}$ , can be obtained from the dispersion equation (A-14) by approximating  $\tan \kappa_p \frac{t}{2}$  and  $\tan \frac{\kappa_s t}{2}$  as  $\frac{\kappa_p t}{2}$  and  $\frac{\kappa_s t}{2}$  for the case of a thin plate at low frequencies. The modal wavenumbers are found to be

$$\begin{aligned} k_{F0} &= \sqrt{\frac{k_s}{t} \sqrt{6(1-\nu)}} \\ k_{F1} &= -j \sqrt{\frac{k_s}{t} \sqrt{6(1-\nu)}} \end{aligned} \tag{A-19}$$

The mode functions given in (A-16) and (A-17) may be approximated by substituting  $\sin \theta \approx \theta$  and  $\cos \theta \approx 1 - \frac{\theta^2}{2}$ , which is appropriate for the case of a thin plate. The thin plate approximations for the  $F(0)$  mode gives

$$\underline{g}(y,z) = \frac{1}{N_0} \begin{bmatrix} \frac{1}{\sqrt{\mu\rho}} \frac{1}{1-2r} \\ \frac{jk_z y}{\sqrt{\mu\rho}} \frac{1}{1-2r} \\ jk_s y \left\{ \frac{1}{1-\nu} + \frac{1}{1-2r} \left( \frac{2k_z^2}{k_s^2} - 1 \right) \right\} \end{bmatrix} e^{-jk_z z} \quad (A-20)$$

$$\underline{q}(y,z) = \frac{1}{N_0} \begin{bmatrix} \frac{k_s^2 ((t/2)^2 - y^2)}{\sqrt{\mu\rho} 2(1-\nu)} \\ -j2\sqrt{\mu\rho} k_z y \frac{1}{1-2r} \\ \frac{jk_s y}{1-2r} \end{bmatrix} e^{-jk_z z} \quad (A-21)$$

Here

$$r = \sqrt{6(1-\nu)}/k_s t \quad (A-22)$$

and the characteristic impedance is given by

$$Z_0 = \frac{\omega\rho}{\kappa} \quad (A-23)$$

The normalization constant  $N_0$  can be obtained via (A-8) as

$$N_0 = \sqrt{\frac{k_s^2 t^3}{6(1-\nu)(2r-1)} \left[ 1 - \frac{1-\nu}{2(1-2r)} \right]} \quad (A-24)$$

The thin plate approximations for the F(1) mode gives

$$\underline{g}(y,z) = \frac{1}{N_1} \begin{bmatrix} \sqrt{\mu\rho} \frac{1}{1+2r} \\ \frac{jk_z y}{\sqrt{\mu\rho}} \frac{1}{1+2r} \\ jk_s y \left\{ \frac{1}{1-\nu} + \frac{1}{1+2r} \left( \frac{2k_z^2}{k_s^2} - 1 \right) \right\} \end{bmatrix} e^{-jk_z z} \quad (A-25)$$

$$\underline{q}(y,z) = -\frac{1}{N_1} \begin{bmatrix} \sqrt{\mu\rho} \frac{k_s^2 ((t/2)^2 - y^2)}{2(1-\nu)} \\ -j2\sqrt{\mu\rho} \frac{k_z y}{1+2r} \\ jk_s y \frac{1}{1+2r} \end{bmatrix} e^{-jk_z z} \quad (A-26)$$

where  $r$  is given in (A-22). For the F(1) mode

$$Z_1 = -\frac{\omega\rho}{\kappa} \quad (A-27)$$

and

$$N_1 = \sqrt{\frac{k_s^2 t^3}{6(1+2r)(1-\nu)} \left[ 1 - \frac{1-\nu}{2(1+2r)} \right]} \quad (A-28)$$

The - sign in the characteristic impedance  $Z_1$  and the mode functions  $\underline{q}$  has been chosen in order to satisfy normalizing condition (A-8).

#### B. SH Modes of an Infinite Plate

The SH modes are orthogonally polarized with respect to the Lamb modes in that the particle displacement of an SH mode is parallel to the plate faces but perpendicular to the propagation direction. The lowest mode, SH(0), is of even symmetry and the only SH mode that propagates down to zero frequency. The dispersion relation for symmetric SH modes, which yield SH wavenumbers,  $k_{SH} = \sqrt{\kappa^2 + k_z^2}$  as a function of frequency, is given by the simple expression

$$k_{SH} = \sqrt{k_s^2 - (2n\pi/t)^2} \quad n = 0, 1, 2, \dots \quad (A-29)$$

Here,  $k_s = \omega \sqrt{\frac{\rho}{\mu}}$  is the shear wavenumber.

The normalized mode functions of even symmetry are given by

$$g(y, z) = \frac{1}{N_e} \begin{bmatrix} 0 \\ \frac{1}{\sqrt{\mu\rho}} \\ 2 \frac{k_z}{k_s} \end{bmatrix} \cos \frac{2n\pi y}{t} e^{-jk_z z} \quad (A-30)$$

$$g(y, z) = \frac{1}{N_e} \begin{bmatrix} -j\sqrt{\mu\rho} \frac{2k_z}{k_s^2} \frac{n\pi}{t} \sin \frac{2n\pi y}{t} \\ \sqrt{\mu\rho} \frac{k_z^2 - k^2}{k_s^2} \cos \frac{2n\pi y}{t} \\ -\frac{k_z}{k_s} \cos \frac{2n\pi y}{t} \end{bmatrix} e^{-jk_z z} \quad (A-31)$$

where

$$N_e = \sqrt{\left[1 - \left(\frac{n\lambda_s}{t}\right)^2\right] \frac{t}{2} \epsilon_n} \quad (A-32)$$

with  $\lambda_s = 2\pi/k_s$  and

$$\epsilon_n = \begin{cases} 2 & n = 0 \\ 1 & n > 0 \end{cases} \quad (A-33)$$

The characteristic impedance is chosen to be

$$Z_s = \frac{\mu k}{\omega} \quad (A-34)$$

The dispersion relation and the mode functions for the lowest SH mode, SH(0), can be obtained by simply setting  $n = 0$  in (A-29) through (A-33).

One obtains

$$k_{SH} = k_s \quad (A-35)$$

$$g(y, z) = \frac{1}{\sqrt{t}} \begin{bmatrix} 0 \\ \frac{1}{\sqrt{\mu\rho}} \\ \frac{2k_z}{k_s} \end{bmatrix} e^{-jk_z z} \quad (A-36)$$

$$q(y, z) = \frac{1}{\sqrt{t}} \begin{bmatrix} 0 \\ \sqrt{\mu\rho} \frac{k_z^2 - k^2}{k_s^2} \\ -\frac{k_z}{k_s} \end{bmatrix} e^{-jk_z z} \quad (A-37)$$

The modal quantities used in the text, and listed in equations (7)-(17) are obtained by setting  $k_z = 0$  in corresponding expression listed in this Appendix.

### References

- 1a. R.B. Thompson, et al., "Dispersion of Flexural Elastic Waves in Honeycomb Sandwich Panels", JASA, Vol. 57, pp. 1119-1127 (1975).
- 1b. R.B. Thompson, et al., "Acoustic Delays of the Order of a Millisecond per Inch in Cellular Materials", IEEE Trans., Vol. SU-18, p. 184 (1971).
2. A.A. Oliner, H.L. Bertoni and R.C.M. Li, "A Microwave Network Formalism for Acoustic Waves in Isotropic Media", Proc. IEEE, Vol. 60, pp. 1503-1512 (1972).
3. A.A. Oliner, R.C.M. Li and H.L. Bertoni, "Catalog of Acoustic Equivalent Networks for Planar Interfaces", Proc. IEEE, Vol. 60, pp. 1513-1518 (1972).
4. R.C.M. Li, A.A. Oliner, H.L. Bertoni, "Microwave Network Analysis of Surface Acoustic Waveguides, I: Flat Overlay Guides", IEEE Trans. Sonics Ultrason., Vol. SU-24, No. 2, pp. 66-78 (March 1977).
5. S. Markman, R.C.M. Li, A.A. Oliner, H.L. Bertoni, "Microwave Network Analysis of Surface Acoustic Waveguides, II: Rectangular Ridge Guides", IEEE Trans. Sonics Ultrason., Vol. SU-24, No. 2, pp. 79-87 (March 1977).
6. S. Markman, "A Microwave Network Analysis of Rid Ridge-Type Surface Acoustic Waveguides", Ph.D. Dissertation, Polytechnic Inst. of New York (1973).
7. R.D. Mindlin, "Influence of Rotary Inertia and Shear on Flexural Motions of Isotropic Elastic Plates", J. Appl. Mech., pp. 31-38 (1951).
8. T.R. Kane and R.D. Mindlin, "High Frequency Extensional Vibrations of Plates", J. Appl. Mech., pp. 277-283 (1956).
9. R.C.M. Li and J. Meingailis, "The Influence of Stored Energy at Step Discontinuities on the Behavior of Surface-Wave Gratings", IEEE Trans., Vol. SU-22, pp. 189-198 (1975).
10. L. Cremer, M. Heckel and E.E. Ungar, Structure-Borne Sound, Springer-Verlag, New York, 1973, pp. 306-335.

11. B.A. Auld, Acoustic Fields and Waves in Solids: Vol. I, John Wiley and Sons, New York, 1973, pp. 388-391.
12. Mechanical Properties of Hexcel Honeycomb Materials, Hexcel, Dublin, California, 1976 , Report TSB 120.
13. B.A. Auld, op. cit., pp. 107-124.
14. L.J. Graham, "Frequency Response Characteristics of Acoustic Emission Systems Components", Science Center, Rockwell International, Report SCTR-73-6, 1973 .
15. C.T. Lynch, Handbook of Materials Science: Vol. III, CRC Press, Cleveland, Ohio, 1975, pp. 77-79.



## MISSION of Rome Air Development Center

RADC plans and executes research, development, test and selected acquisition programs in support of Command, Control Communications and Intelligence (C<sup>3</sup>I) activities. Technical and engineering support within areas of technical competence is provided to ESD Program Offices (POs) and other ESD elements. The principal technical mission areas are communications, electromagnetic guidance and control, surveillance of ground and airborne objects, intelligence data collection and handling, information system technology, ionospheric propagation, solid state sciences, microwave physics and electronics reliability, maintainability and compatibility.

DATE  
FILMED  
-8